Sun, H. *et al.* (2019). *Géotechnique* **69**, No. 8, 713–726 [https://doi.org/10.1680/jgeot.17.P.253]

Bentonite microstructure and saturation evolution in wetting–drying cycles evaluated using ESEM, MIP and WRC measurements

HAIQUAN SUN*, DAVID MAŠÍN†, JAN NAJSER‡, VILÉM NEDĚLA§ and EVA NAVRÁTILOVÁ§

In this paper, the microstructure of the Czech bentonite B75 was investigated by three methods: water retention curve (WRC) measurements, mercury intrusion porosimetry (MIP) measurements and environmental scanning electron microscopy (ESEM) investigation. The experiments were performed on samples at various compaction levels (between 1·27 and 1·90 g/cm^3) and at various suctions (between 3·3 and 290 MPa) along both drying and wetting hydraulic paths. In the ESEM observations, target relative humidities (and thus total suctions) were imposed directly in the ESEM chamber to observe the effect of the hydraulic path on the microstructure. Apart from the inter-lamellar pores, which are not accessible to the adopted experimental techniques, two pore families were identified: micropores and macropores. The transition pore size between the micropores and macropores was found to be suction dependent. The microporosity was practically insensitive to compaction and only the largest micropores were sensitive to suction. Smaller macropores were sensitive to compaction only, whereas larger macropores were sensitive to both compaction and suction. It was observed that, during wetting from the as-compacted state, the macropores remained completely dry up to very low values of suction, whereas the micropores were found to be unsaturated up to the suctions between 10 to 60 MPa. Both macropores and micropores contributed to sample volume changes during drying and wetting. Although the microstructural volume change appeared to be reversible, the macrostructure exhibited permanent deformation.

KEYWORDS: fabric/structure of soils; suction

INTRODUCTION

It is now well accepted that compacted bentonite has a structure with two distinct pore systems, denoted as a double structure (Gens & Alonso, 1992; Alonso *et al.*, 1999, 2010). This double structure is explicitly considered in many bentonite constitutive models, focusing on its mechanical behaviour (Alonso *et al.*, 1999; Lloret *et al.*, 2003), hydraulic behaviour (Romero *et al.*, 2011), coupled hydro-mechanical behaviour (Simms & Yanful, 2005; Della Vecchia *et al.*, 2013; Mašín, 2013; Sánchez *et al.*, 2016; Li *et al.*, 2017) or hydro-mechanical behaviour, considering the effect of temperature change (Mašín, 2017). In these models, inter-play between the mechanical, hydraulic and/or thermal response of micropores and macropores is considered and the global response results from the rearrangement of the macrostructural units and the physical–chemical–mechanical interaction of clay minerals and aggregates. In these models, aggregates are often considered as fully saturated and their mechanical response is assumed to be reversible.

In this paper, the authors focus on investigation of the effect of wetting and drying on the bentonite microstructure. The microstructure is investigated using mercury intrusion posorimetry (MIP) and an environmental scanning electron microscopy (ESEM) method, which are supplemented by water retention measurements. Bentonite microstructure has been studied by many authors in the past. Microstructure investigation using MIP has been presented, for example, by Monroy *et al.* (2010), Lloret & Villar (2007), Romero *et al.* (1999, 2011), Simms & Yanful (2001), Cuisinier & Laloui (2004), Cui (2017) and Romero & Simms (2008). Typically, the authors observe bi-modal pore structure consistent with a double structure modelling approach. However, in several recent studies, it has been suggested that the consideration of two pore families may be an oversimplification of the complex bentonite structure. For example, Wang *et al.* (2014) identified four major pore sizes, which include inaccessible pores (<6 nm), small pores (6–40 nm), medium pores (40 nm–2 μm) and large pores (>2 μm) for MX80 bentonite. Přikryl & Weishauptová (2010) investigated the hierarchical porosity of the Czech bentonite from Rokle deposit (similar to the one used in this study). Four pore size categories were identified by the authors by adsorption isotherms and MIP testing, namely inter-lamellar pores (average radius 0·65 nm), mesopores within individual aggregates (with two peaks corresponding to 2–2·5 nm and 5–10 nm), macropores (+ mesopores) between aggregates of clay minerals (2–63 μm) and coarse pores (>63 μm) between non-clayey particles of sand size. Monroy *et al.* (2010) considered three classes of pores, nanoporosity (which cannot be detected by MIP technique), microporosity and macroporosity for compacted London Clay, with delimiting pore size approximately 2 μm. Microporosity was found to depend substantially on suction. Villar *et al.* (2014) delimit macropores and mesopores by 5 μm for both MX80 and Febex bentonite; the non-intruded pores were named micropores. Manca *et al.* (2016) found 5 μm to be a delimitation of macro- and micropores, and the delimiting pore size was found to be independent of density. Hattab *et al.* (2013) studied the microstructure of natural and remoulded sensitive marine

Manuscript received 6 October 2017; revised manuscript accepted 23 August 2018. Published online ahead of print 26 September 2018. Discussion on this paper closes on 1 January 2020, for further details see p. ii.

* Faculty of Science, Charles University, Prague, Czech Republic.
† Faculty of Science, Charles University, Prague, Czech Republic (Orcid:0000-0002-5990-6021).
‡ Faculty of Science, Charles University, Prague, Czech Republic (Orcid:0000-0002-6702-3210).
§ Institute of Scientific Instruments, The Czech Academy of Sciences, Brno, Czech Republic.

sediment by MIP tests, showing that the compaction is predominantly influencing macropores. Seiphoori *et al.* (2014) investigated the microstructure of MX80 bentonite under wetting–drying cycles by MIP and SEM tests. A clear transition from a bimodal pore structure to a single pore structure was found upon full saturation, similarly to Monroy *et al.* (2010).

Scanning electron microscopy (SEM) has been widely used in clay science, and can provide information about the bentonite microstructure. The samples used for SEM observation must be completely dried and coated with gold. As the drying process affects the bentonite structure substantially, it is preferable to adopt more advanced ESEM, where vapour pressure (and thus total suction) can be controlled directly in the observation chamber. The ESEM technique was used by Watt *et al.* (2000), who showed that charge-contrast imaging can improve the resolution of an ESEM image. Komine & Ogata (1999) found that bentonite aggregates swell into macrovoids along wetting paths, the level of macrovoid occlusion being dependent on bentonite content in a sand–bentonite mixture. Romero (1999) observed highly compacted Boom Clay (2 g/cm^3) under relative humidities of 28, 53, 71 and 81% in an ESEM chamber. Results showed that irreversible aggregate volume change occurred. Montes-H *et al.* (2005) investigated MX80 bentonite at four different densities subjected to hydration/dehydration cycles under ESEM observation. Their results showed that the mechanical compaction influences the clay microstructure. Villar & Lloret (2001) observed the Febex bentonite aggregates by ESEM with a relative humidity between 50% and nearly 100% under constant volume. They showed that the macropore volume had been reduced due to the swelling of aggregates.

The water retention properties of compacted clay/bentonite have been related to its microstructure by various authors. Villar (2007) observed that the water retention curve (WRC) was not dependent on relative density for suctions higher than 10 MPa. Similar observations have been made by Romero & Vaunat (2000) and Romero *et al.* (2011), who adopted a double-structure framework to interpret water retention behaviour. A similar approach was chosen by Dieudonne *et al.* (2017), who considered adsorbed water in the micropores and capillary water in the macropores separately. Gatabin *et al.* (2016) attributed the difference in WRCs of bentonite measured under confined and unconfined conditions to its microstructure.

In the present paper, the authors focus on studying the Czech compacted Ca–Mg bentonite from Černý vrch deposit, known as B75. Unlike many previous studies, where MIP testing and ESEM imaging was adopted in a qualitative description of the bentonite microstructure, here the authors aim to study the results quantitatively. A combination of the methods allows unexpected conclusions to be drawn, which would have been difficult to obtain using individual methods, such as information about the state of saturation of the aggregates and macropores, the contribution of macroporosity and microporosity to sample deformation and distinction and the properties of the pore size classes.

MATERIAL

The Czech bentonite B75 extracted from the Cerny vrch deposit (north-western region of the Czech Republic) and commercially supplied in the form of powder, was used in this study. The montmorillonite content was around 60% and the water content of the bentonite powder was about 10%. Table 1 lists its physical parameters. The plastic limit, liquid limit and specific gravity of the solid are 65%, 229% and 2·87, respectively. The cation exchange capacity is shown in Table 2. The chemical composition of bentonite B75 is shown in Table 3.

Table 1. Montmorillonite content and physical properties of bentonite B75 (Stastka & Smutek, 2015)

Property	Description
Montmorillonite: %	60
Liquid limit: %	229
Plastic limit: %	65
Plasticity index, I_p	164
Particle density, ρ_s: g/cm^3	2·87

Table 2. Cation exchange capacity of bentonite B75 (Sun *et al.*, 2017)

Cation	meq/100 g
Ca^{2+}	36·92
Na^+	65·75
K^+	3·03
Mg^{2+}	26·84
H^+	<0·5

Table 3. Chemical composition of bentonite B75 (Hausmannova & Vasicek, 2014)

Component	Weight: %
Silicon dioxide (SiO_2)	51·91
Aluminium oxide (Al_2O_3)	15·52
Iron (III) oxide (Fe_2O_3)	8·89
Titanium dioxide (TiO_2)	2·28
Calcium oxide (CaO)	4·6
Magnesium oxide (MgO)	2·22
Sodium oxide (Na_2O)	1·21
Potassium oxide (K_2O)	1·27
Phosphorus pentoxide (P_2O_5)	0·4
Manganese oxide (MnO)	0·11
Iron (II) oxide (FeO)	2·95
Sulfur trioxide (SO_3)	0·09
Calcium carbonate ($CaCO_3$)	11·71
Carbon dioxide (CO_2)	5·15

METHODS

The samples used in the tests were prepared from the bentonite powder at its initial water content by uniaxial compaction in a laboratory mould to reach the desired initial dry density (1·27, 1·60 and 1·90 g/cm^3). The height of the sample was 10 mm and the diameter was 50 mm.

Table 4 shows test procedures and initial states of samples in the experiments. The compacted samples were split into two parts. One part was directly equilibrated in the desiccator under controlled suction from 3·29 MPa to 286·7 MPa. The other part was first oven dried, thus reaching an approximate suction of 1000 MPa (Nowamooz & Masrouri, 2010).

The samples were then either directly equilibrated in a desiccator at various suctions for the wetting path or equilibrated at a suction of 3·29 MPa and then moved to the higher suction desiccator for WRC measurements along drying paths. Both the sample types – namely, samples directly equilibrated at the suctions of 3·29, 38 and 286·7 MPa and samples initially oven dried and then equilibrated – were used for MIP tests. The samples initially oven dried and then equilibrated at 286·7 MPa were used in ESEM observations in a variable relative humidity chamber.

Table 4. Test programme

Initial ρ_d: g/cm^3	Initial w_c: %	Initial suction: MPa	Sample state	Suction paths: MPa
1·27	10	48·57	Oven dried	WRC: 286·7→3·29 ESEM: 290·75→3·85→290·75 MIP: 286·7, 38·00, 3·29
			Directly equilibrated	MIP: 286·7, 38·00, 3·29
			Equilibrated at suction of 3·29 MPa	WRC: 3·29→286·7
1·6	10	46·65	Oven dried	WRC: 286·7→3·29
			Equilibrated at suction of 3·29 MPa	WRC: 3·29→286·7
1·9	10	49·29	Oven dried	WRC: 286·7→3·29 ESEM: 290·75→3·85→290·75 MIP: 286·7, 38·00, 3·29
			Directly equilibrated	MIP: 286·7, 38·00, 3·29
			Equilibrated at suction of 3·29 MPa	WRC: 3·29→286·7

Table 5. Salt solutions used for vapour equilibrium method measurements (for temperature of 20°C) (OIML, 1996)

Salt solutions	Solubility: g/100 ml	Relative humidity: %	Suction: MPa
Lithium chloride monohydrate ($LiCl·H_2O$)	82·78	12·0	286·7
Potassium acetate (CH_3COOK)	268·6	23·1	198·14
Magnesium chloride hexahydrate ($MgCl_2·6H_2O$)	55·24	33·1	149·51
Potassium carbonate (K_2CO_3)	109·43	43·2	113·50
Sodium bromide (NaBr)	91·21	59·1	71·12
Sodium chloride (NaCl)	36	75·5	38·00
Potassium chloride (KCl)	34	85·1	21·82
Potassium sulfate (K_2SO_4)	11·05	97·6	3·29

The WRCs were measured at three different initial dry densities (1·27, 1·60and 1·90 g/cm^3), whereas the ESEM and MIP tests were performed at low (1·27 g/cm^3) and high (1·90 g/cm^3) compaction dry densities only.

Water retention curves

The vapour equilibrium method (Delage *et al*., 1998) was applied to suction control. Relative humidity in the closed desiccator was controlled by different saturated salt solutions (adopted from OIML (1996)). The total suction has a unique relationship with relative humidity described by Kelvin's equation.

$$S_t = \left(\frac{RT\rho_w}{\omega}\right) \ln(1/\mathrm{RH}) \quad (1)$$

where S_t is the total suction (kPa); R is the molar gas constant, which equals 8·314462 J/(mol K); T is the absolute temperature (K); ρ_w is the density of water (kg/m^3); ω is the molecular mass of water vapour, which equals 18·016 g/mol; RH denotes the relative humidity of the system, which is defined as the ratio of partial pressure of vapour over saturation vapour pressure.

The relative humidity, solubility and total suction of each saturated salt solution applied in this paper are listed in Table 5. The samples of different dry densities were dried in the oven at 105°C for over 24 h. Then, the samples were broken into small irregular pieces weighing between 0·8 and 1·5 g and put into the desiccator. All the desiccators were placed in an air-conditioned room at 20°C. The samples were not confined; they could thus freely expand during wetting. The weight of the bentonite was regularly measured until the sample mass stabilised. It usually took about 2 months to reach equilibrium, consistently with Tang & Cui (2005) (see example results in Fig. 1). Once the equilibrium was reached, one part of the samples was used for the equilibrium water content determination, another part was immediately weighted and then covered by wax. The volume was measured using the wax immersion method following the ASTM C914-95 (ASTM, 2004) procedure. The water content and void ratio of each of the samples were determined and the degree of saturation was calculated from the obtained values.

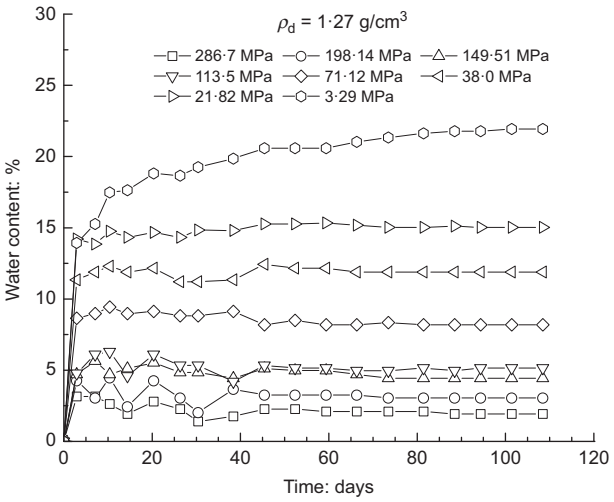

Fig. 1. Example of water content time evolution in WRC measurements by vapour equilibrium method for initial dry density of 1·27 g/cm^3

In order to evaluate the precision of volume measurements using the wax immersion method, three iron balls of different diameter with known volumes were used to calibrate the volume measurements. Fig. 2(a) shows the volume errors with respect to measurement number for three different iron ball volumes. Fig. 2(b) shows the relationship between the error and the iron ball volume. It can be seen that, as expected, the error increased with decreasing volume.

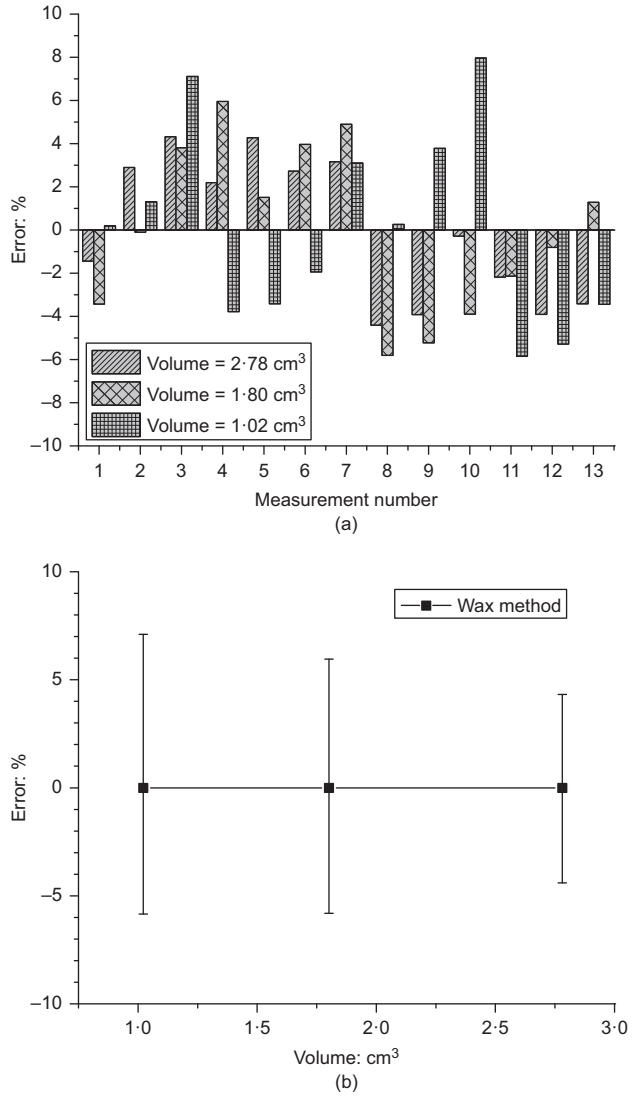

Fig. 2. Uncertainty of volume measurement by wax immersion method. (a) Volume measurement errors with respect to measurement number for balls of three different volumes; (b) volume measurements errors plotted against ball volumes

Considering the volume of bentonite used for evaluation of WRCs, the uncertainty of volume measurements of −5·8 to 7·1% was assumed for calculated void ratio and these values are included as error bars in the graphs presenting the measurement data.

Mercury intrusion porosimetry

Mercury intrusion porosimetry is based on the capillary law governing non-wetting liquid (with contact angle bigger than 90°) penetration into small pores. The pore entrance diameter (D) can be determined from the applied mercury pressure (P) by assuming that the cylindrical pores existed in soil according to the Washburn equation (Juang & Holtz, 1986)

$$D = -(4\sigma_{Hg}\cos\theta_{nw})/P \quad (2)$$

where D is the entrance pore diameter; σ_{Hg} is the surface tension of mercury; θ_{nw} is the contact angle between the mercury and the soil surface; and P is the intrusion pressure. In this study, the values $\theta_{nw} = 130°$ and $\sigma_{Hg} = 0{\cdot}484$ N/m at 25°C were considered in the pore diameter calculation.

The tests were performed at the Department of Inorganic Technology at the University of Chemistry and Technology Prague (Apparatus Autopore IV, Micromeritics). The measurement was done in two regimes, one was a low-pressure regime from 0·01 to 0·2 MPa (corresponding to the pore radius between 100 and 3 μm); the other one is the high-pressure regime from 0·2 to 400 MPa (corresponding to the pore radius between 3 μm and 1·5 nm). MIP tests were conducted on freeze-dried samples to retain the original microstructure. In freeze-drying methods, the samples were first immersed in liquid nitrogen and then the frozen samples were placed under a deep vacuum. Finally, the samples went through sublimation in the vacuumed chamber of a freeze dryer (Delage *et al.*, 1996).

In the tests, samples of two different initial dry densities of the as-compacted initial water content were oven dried and then equilibrated at suctions of 286·7, 38 and 3·29 MPa. Other experiments were performed on samples with as-compacted initial water content, again equilibrated at the three suction levels of 286·7, 38 and 3·29 MPa subsequently.

Environmental scanning electron microscopy

The ESEM tests were performed using a Quanta 650 FEG scanning electron microscope at the Institute of Scientific

Table 6. Water vapour pressure, relative humidity and total suction adopted in ESEM measurements

Temperature 5°C		
Relative humidity: %	Water vapour pressure: Pa	Total suction: MPa
10	93	290·75
30	266	152·03
50	439	87·52
60	519	64·50
74	649	38·02
80	692	28·18
90	785	13·30
97	850	3·85
90	785	13·30
80	692	28·18
74	649	38·02
60	519	64·50
50	439	87·52
30	266	152·03
10	93	290·75

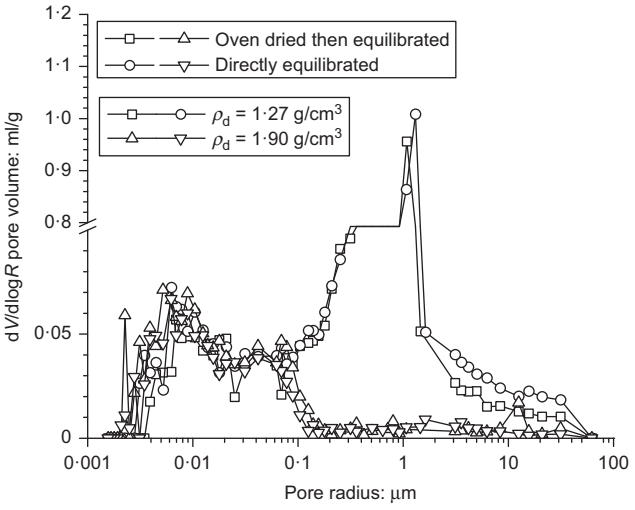

Fig. 3. The effect of oven drying on pore size distribution of 1·27 g/cm^3 and 1·90 g/cm^3 samples

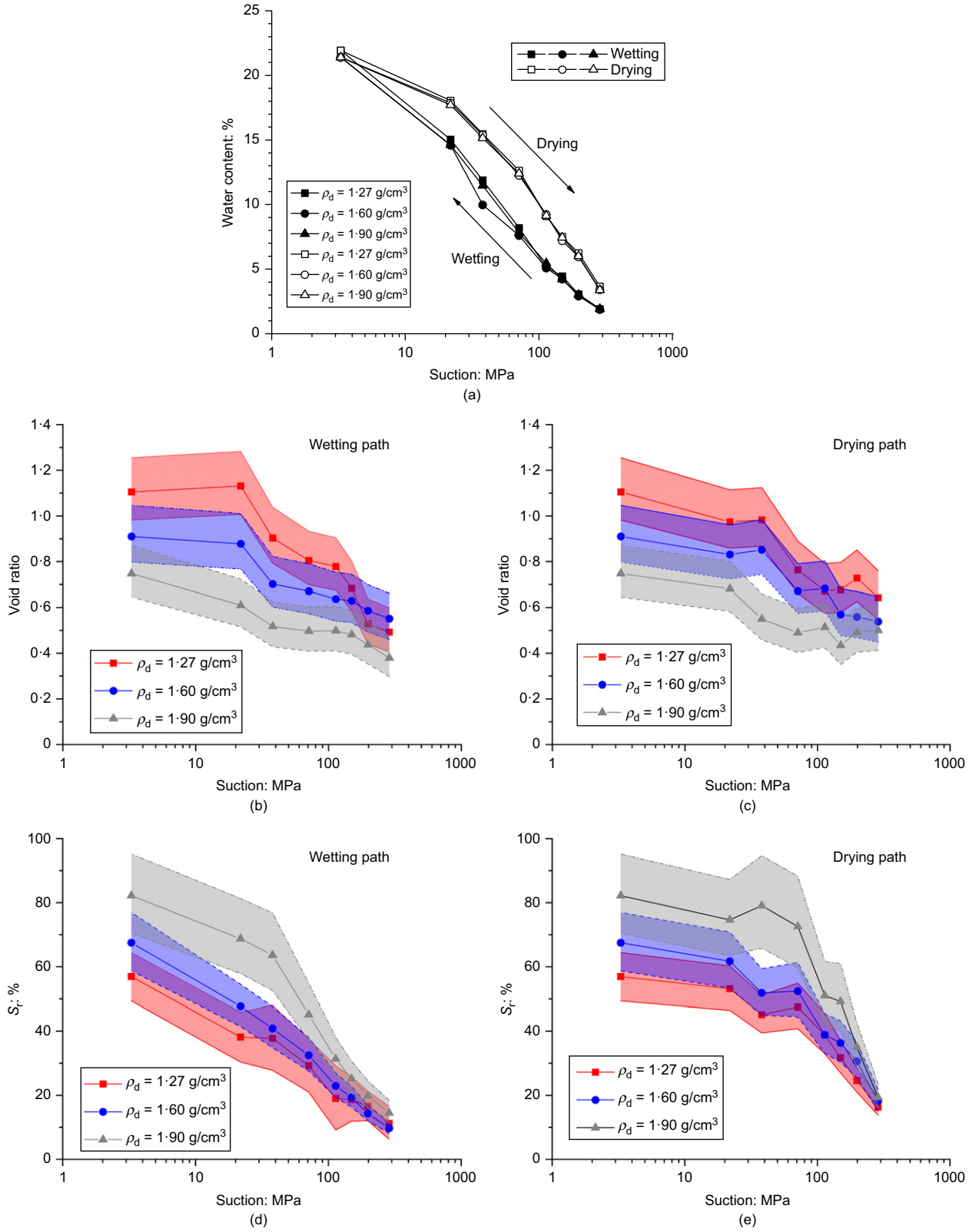

Fig. 4. Water content, void ratio and degree of saturation with respect to suction for WRC measurements along wetting and drying path at three different initial dry densities. (a) Water content against suction curves; (b, c) void ratio against suction curves for wetting and drying paths; (d, e) degree of saturation against suction curves for wetting and drying paths. Shaded areas indicate volume measurement errors based on ball volume measurements

Instruments of the Czech Academy of Sciences, Brno. Oven-dried samples equilibrated at the suction of 286·7 MPa were used for the ESEM observations. The samples taken from the desiccator were immediately prepared for the ESEM test. No cutting tool was used to prepare the sample surface; instead, following the procedures of Lin & Cerato (2014), the specimen was fractured in order to expose a fresh, undisturbed section of the sample. The tests were performed at constant temperature of 5°C; the water vapour pressure was imposed directly in the ESEM chamber, which made it possible to observe directly the microstructure response to suction changes. The water vapour pressure of 93 Pa (relative humidity of 10%, suction of 290·75 MPa) was determined as the optimal initial state for the experiment. Then the vapour

pressure was gradually increased up to 850 Pa (relative humidity 97%, suction of 3·85 MPa). After the relative humidity had reached its maximum value, it was gradually decreased back to 10%. The test conditions are summarised in Table 6. The interval between vapour pressure changes was 15 min. A similar interval was adopted by other researchers (Montes-H, 2005; Lin & Cerato, 2014).

RESULTS AND DISCUSSION

The effect of oven drying on microstructure

As some samples (see Table 4) used for WRC, ESEM and MIP measurements were first oven dried at 105°C before testing and the temperature could potentially affect their microstructure, this effect was evaluated first. Fig. 3 shows pore size density curves measured by MIP method for samples compacted to dry densities 1·27 g/cm^3 and 1·90 g/cm^3 directly equilibrated at the suction of 38 MPa compared with MIP results of the samples equilibrated at the same suction after oven drying. The effect of oven drying on MIP curves is insignificant, apart from its effect on the largest pores, where it can be attributed to mechanical hysteresis due to the drying–wetting cycle. The authors therefore consider the effect of oven drying does not affect the qualitative and quantitative evaluation of the presented data.

Water retention curves

Figure 4(a) shows the WRCs of samples at three initial dry densities (wetting and drying path). It is clear that the initial dry density had only little influence on water content. With the assumption that most water is concentrated in the micropores at high suctions, these results suggest that micropores are only little influenced by the compaction pressures, as if their volume was to be affected, their water retention capacity (which is known to be porosity dependent) would also change. Contrarily, quite a remarkable effect of the initial dry density was found on the degree of saturation (Figs 4(d) and 4(e)) through its effect on void ratio (Figs 4(b) and 4(c)). Although the void ratio measurements using the wax immersion method were subject to an error (indicated as shaded areas in Figs 4(b)–4(e)), the measurements consistently show an increase in the global degree of saturation with increasing dry density.

Mercury intrusion porosimetry measurements

Figure 5 shows the MIP results of low- (1·27 g/cm^3) and high- (1·90 g/cm^3) density samples at each suction level. Fig. 6 then shows the same results, replotted to identify the effect of suction on pore size density curves. The MIP data make it possible to identify the effects of suction and

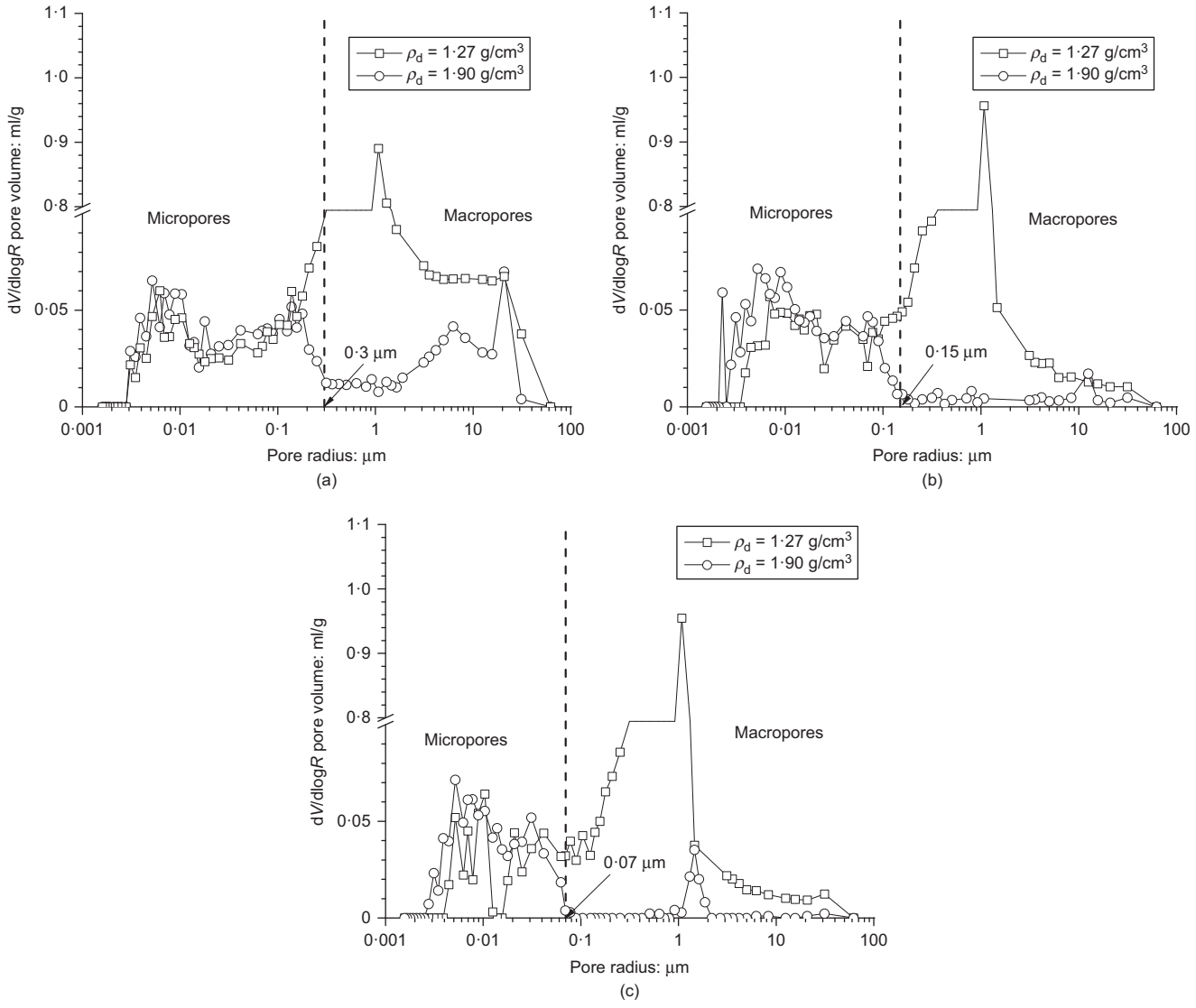

Fig. 5. Pore size distribution curves – the effect of dry density: (a) suction = 3·29 MPa; (b) suction = 38 MPa; (c) suction = 286·7 MPa

compaction level on the individual pore sizes. Apart of the inter-lamellar pores, which are not accessible to the adopted measurement techniques, two primary pore size domains can be distinguished, as described below.

(*a*) 'Micropores': these are between 3 nm and micro–macro transition pore radius. Micropores are defined with the aid of Figs 5 and 6 as smaller pores which are practically unaffected by compaction. The transition pore radii were identified on high-density samples as the maximum pore size which remained open after compaction (in low-density samples, the transition pore radius was not clear due to the dominant effect of macropores). The transition pore radii obtained were 0·07, 0·15 and 0·3 μm for suctions of 286·7, 38 and 3·29 MPa, respectively.
(*b*) 'Macropores': these are larger than the micro–macro transition pore radius. This is a family of larger pores, which are affected by compaction level.

More detailed study of Figs 5 and 6 reveals that, in both the two pore families, only the larger pores are affected by suction: above 0·025 μm for micropores and above 2·5 μm for macropores. It thus seems that, at each level of structure, larger pores are more deformable and are thus more responsive to a change in suction forces. In Fig. 7, void ratios corresponding to the individual pore sizes are quantified from the cumulative pore size distribution curves. It is clear that the compaction level

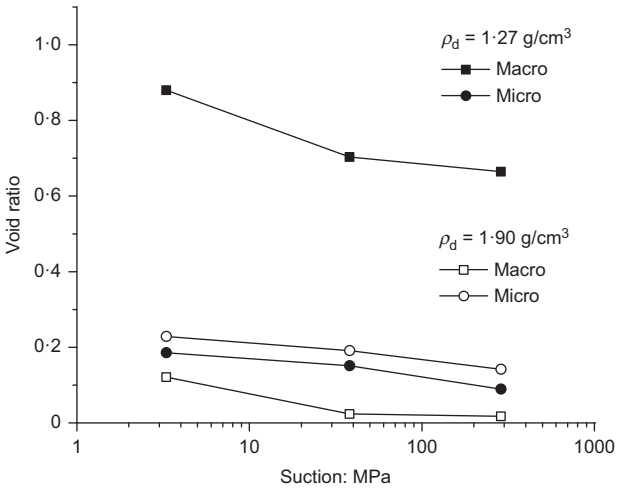

Fig. 7. Void ratios corresponding to the individual pore families calculated from MIP data

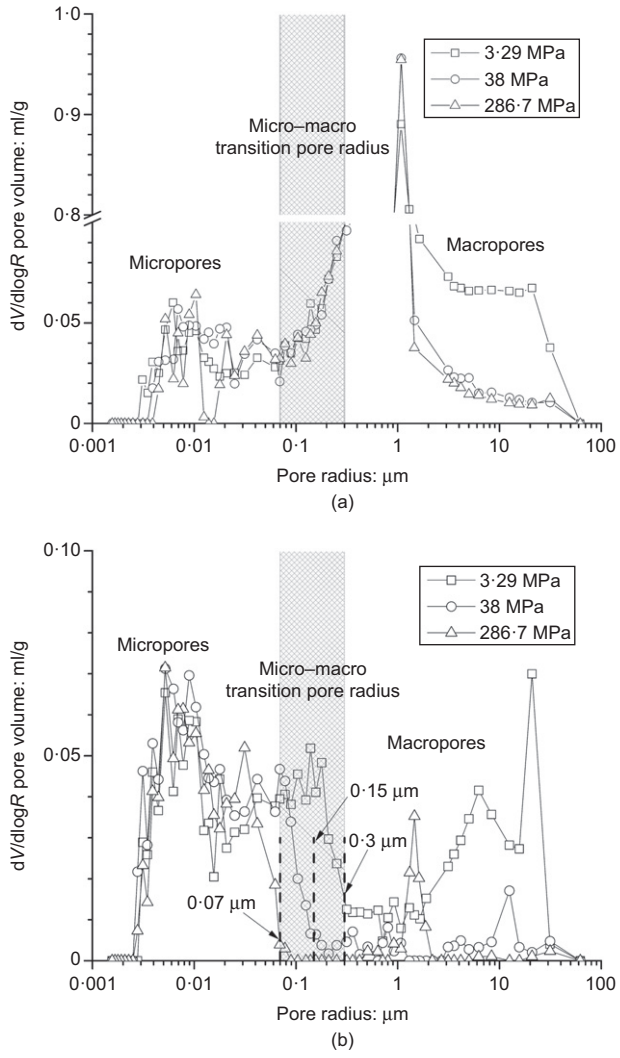

Fig. 6. Pore size distribution curves – the effect of suction and indication of micro–macro transition pore radius: (a) ρ_d = 1·27 g/cm^3; (b) ρ_d = 1·90 g/cm^3

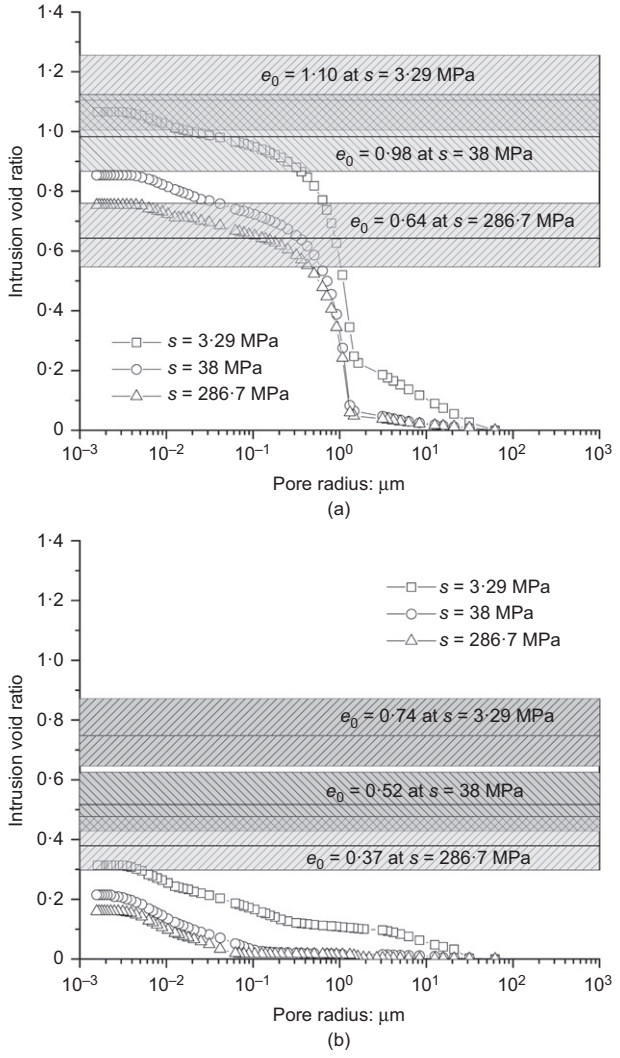

Fig. 8. Cumulative pore size distribution curves along with void ratios obtained during WRC measurements: (a) initial ρ_d = 1·27 g/cm^3; (b) initial ρ_d = 1·90 g/cm^3

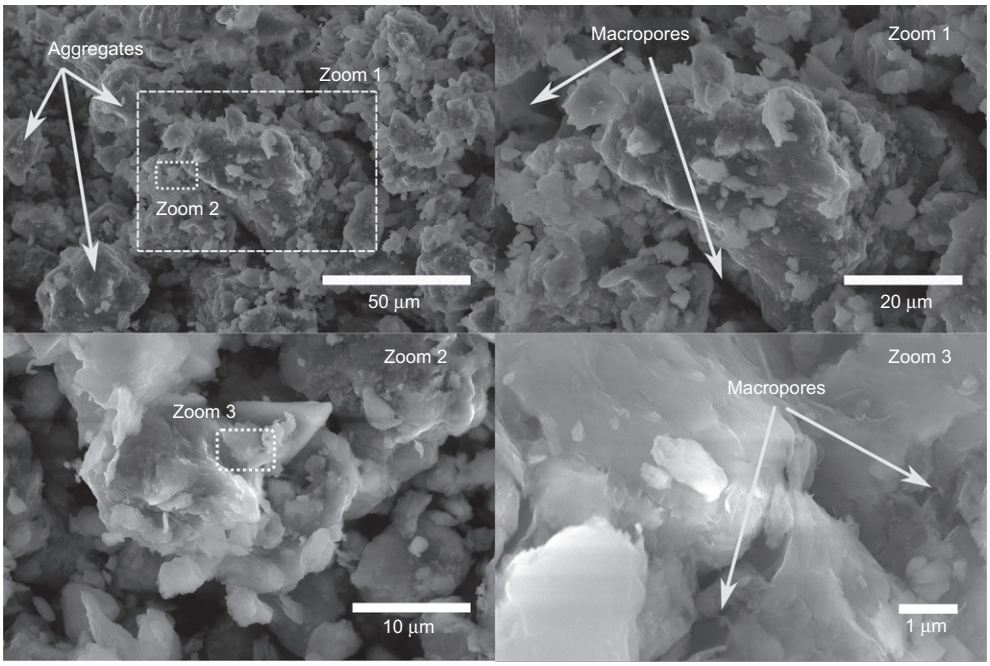

Fig. 9. ESEM micrographs of compacted bentonite with a dry density of 1·27 g/cm^3 at different magnifications (note that 'zoom 2' and 'zoom 3' images are from a different sample section than the main photograph and 'zoom 1' image)

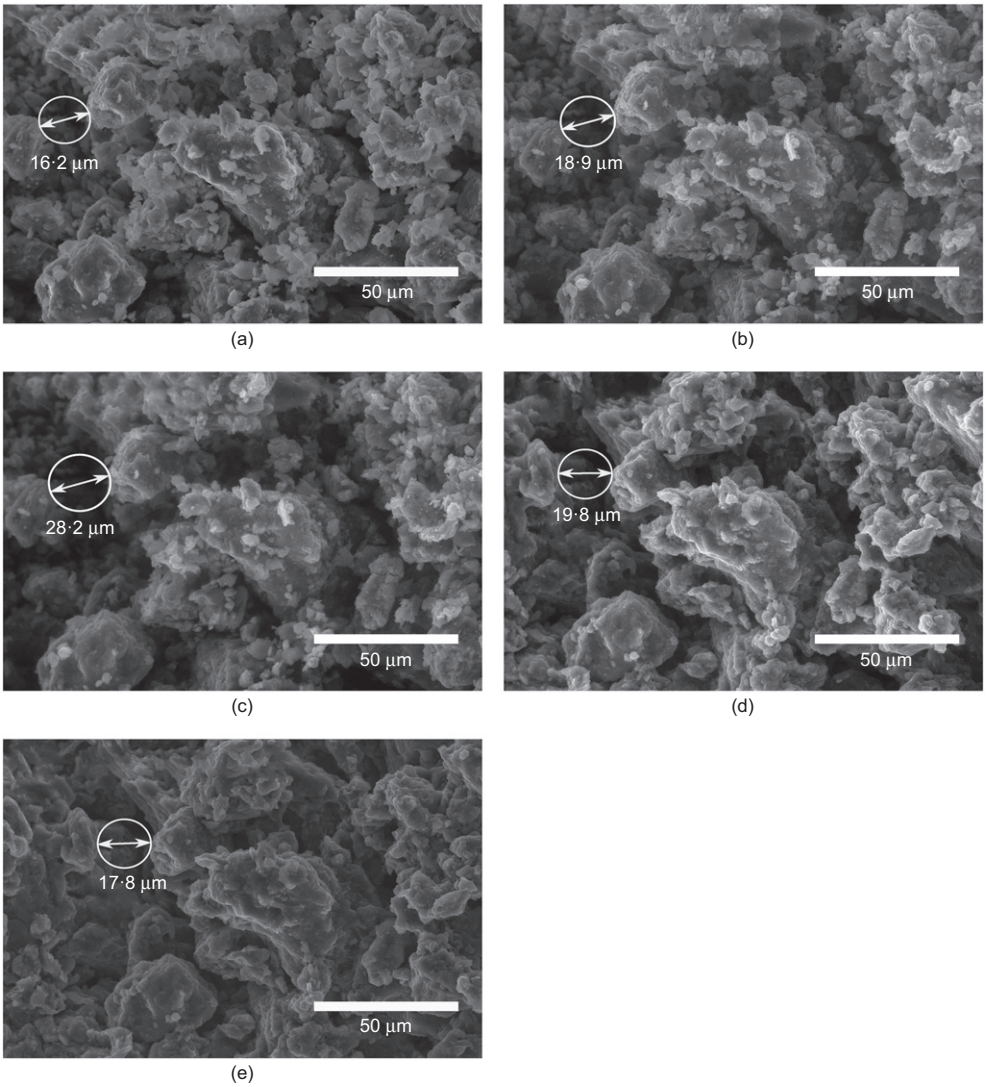

Fig. 10. Selected ESEM micrographs of compacted bentonite with a dry density of 1·27 g/cm^3 under the wetting–drying path: (a) 290·75 MPa; (b) 38·02 MPa; (c) 3·3 MPa; (d) 38·02 MPa; (e) 290·75 MPa

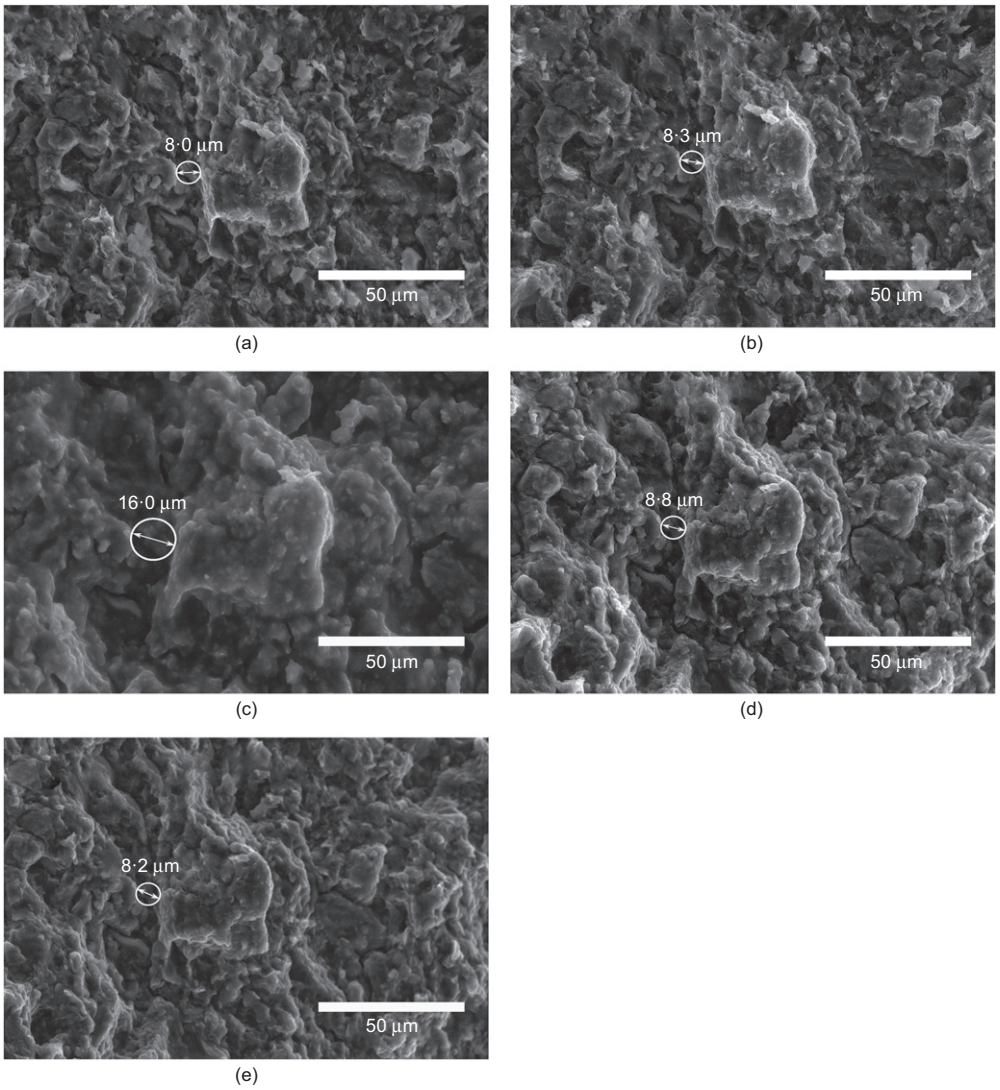

Fig. 11. Selected ESEM micrographs of compacted bentonite with a dry density of 1·9 g/cm^3 under the wetting–drying path: (a) 290·75 MPa; (b) 38·02 MPa; (c) 3·3 MPa; (d) 38·02 MPa; (e) 290·75 MPa

influences mainly the macropores, following the definition which the present authors adopted for distinction of transition pore radius. Micropores are relatively insensitive to compaction effort and they are moderately sensitive to suction, whereas only the largest micropores contribute to deformation due to suction change. Finally, in Fig. 8, cumulative pore size density functions obtained in MIP measurements are compared with void ratios obtained from the wax immersion measurement method (results of wax immersion measurements are plotted along with the error range). Both the measurement methods are subjected to inaccuracies; the errors in the wax immersion method of volume measurement have already been discussed. In addition, MIP evaluation is based on an assumption of cylindrical pore size. Irrespectively of these assumptions, however, it appears that both measurements are relatively consistent with each other in samples with low initial dry density. In samples with high initial dry density, void ratios extracted from MIP data are lower than the void ratios measured by wax immersion method, but relative positions of the curves for different suctions are consistent between the two methods.

Environmental scanning electron microscopy observations

Figure 9 shows example ESEM micrographs of the compacted bentonite with a dry density of 1·27 g/cm^3 which was equilibrated at the total suction of 286·7 MPa. The arrangement of aggregates may be clearly seen, along with different pore families. The aggregates are clearly visible at lower magnification (complete photograph and zoom 1), zoom 2 and zoom 3 then show details of the aggregate structure with microporosity. The micrographs of compacted bentonite subjected to wetting and drying in the ESEM chamber are presented in Fig. 10 for dry density of 1·27 g/cm^3 and in Fig. 11 for dry density of 1·90 g/cm^3. These photographs are qualitatively consistent with MIP observations: macropores and distinct aggregates are visible in the sample with low dry density, only aggregates with the fine bentonite matrix, without clear macroporosity, are visible in the samples with high dry density. It is also clear that the macropores remain dry at most suction levels, apart of lowest suction in the soil at high dry density (Fig. 11(c)), where water menisci in the macropores start to be identifiable in the photographs. Water retention measurements (in particular, the independence of water content from the compaction level, Fig. 4(a)) are consistent with these observations.

To quantitatively analyse the measured data, the authors evaluated the macroporosity evolution with suction and the aggregate size variation with suction. To identify the macroporosity evolution with suction, a double arrow has been included in Figs 10 and 11, which indicates the distance between the selected aggregates. The macropore size increases

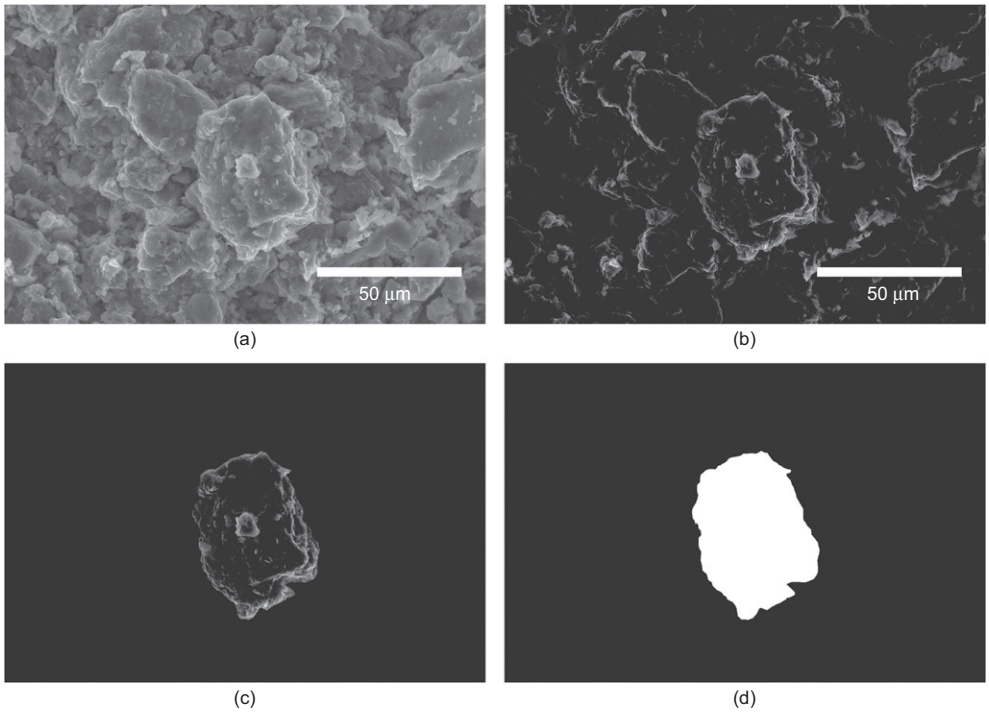

Fig. 12. Digital image analysis methodology for target aggregates: (a) original ESEM microphotographs; (b) image grey level adjustment; (c) target aggregates; (d) measurement of the surface area

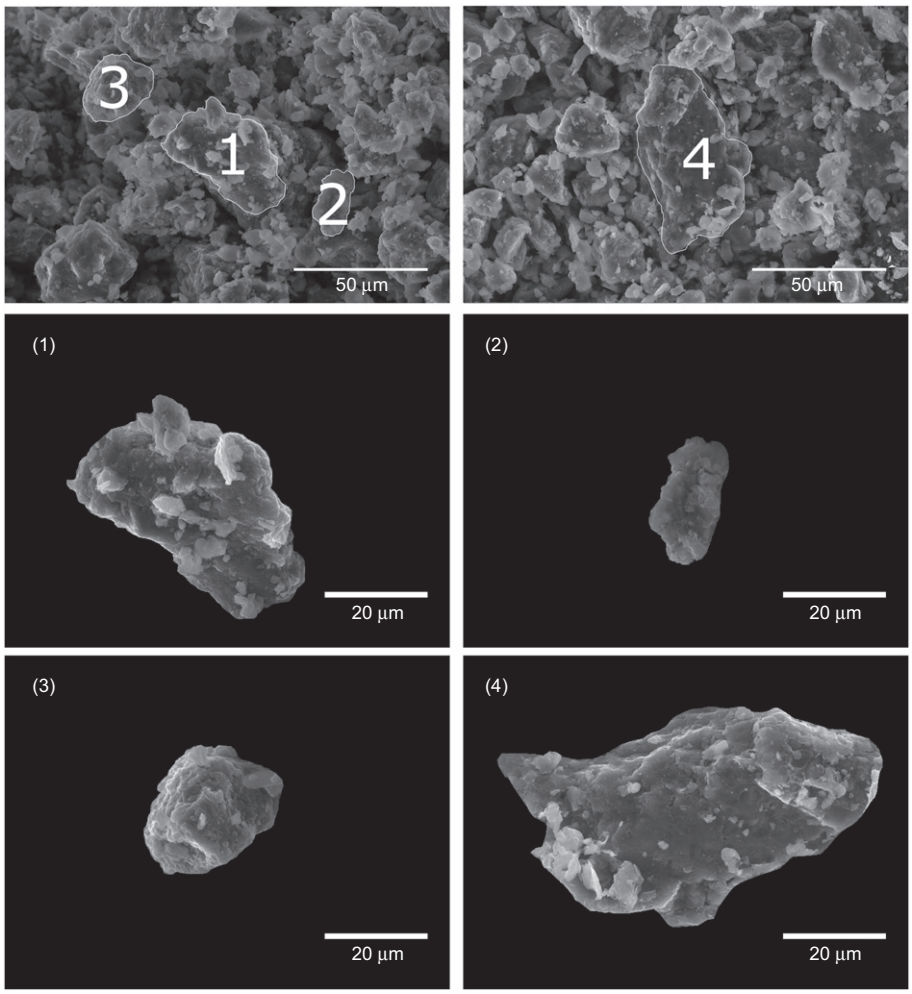

Fig. 13. Aggregates of the initial dry density 1·27 g/cm^3 samples selected for calculation of volume strain

upon wetting and decreases upon drying, consistently with MIP data, which have shown the suction dependency of the larger macropores. The authors could also observe an hysteretic phenomenon occurring after one wetting–drying cycle. The aggregate distance was larger after a wetting–drying cycle than initially. Recall that, consistently with these measurements, an oven drying–wetting cycle on low-density samples caused a smaller volume of larger macropores compared to the directly equilibrated samples (Fig. 3). The wetting–drying cycle thus caused the macroporosity to open, whereas the drying–wetting cycle caused its densification.

In order to quantitatively analyse the volume change of aggregates upon wetting and drying, the digital image analysis technique was used. The original ESEM photograph represents a plan view in two dimensions, as shown in Fig. 12(a). First, the original ESEM photographs were adjusted by threshold grey level to clearly identify the boundary of the aggregates. Then, the surface area of the aggregate was measured using a software tool at each stage (see Figs 12(b)–12(d)). Once the surface area had been obtained, the appropriate aggregate volume was calculated based on an assumption of its spherical shape. The first observation was set at the suction of 290·75 MPa as a starting point. Then, the volume strain could be calculated. The volume strain is used to define the relative volume change of the aggregate, defined as

$$\varepsilon_v = (V_i - V_0)/(V_0) \quad (3)$$

where ε_v is the volume strain; V_i is the volume of the aggregate at the stage i; and V_0 is the volume of the aggregate at the initial state.

Four different aggregates of each dry density were chosen to analyse their volume strain with suction. Figs 13 and 14 show the selected aggregates from ESEM photographs of low- and high-density samples. The volume strain upon wetting and drying paths is shown in Fig. 15. The volume strain increased with decreasing suction; however, this increase was relatively minor up to the low suction of 3·3 MPa. At this suction, a sudden increase in volume strain can be seen, but it is presumed that the values are affected by water entering the macropores, which caused the aggregate boundaries to be less clearly defined in the photomicrograph. During drying, water remained initially in the macropores due to hydraulic hysteresis and thus the apparent aggregate volume was also affected. Above a suction of 38·02 MPa, however, only a very small effect of hydraulic hysteresis is measured; the aggregate volumetric response thus appears to be reversible with suction.

Evaluation of aggregate saturation

Based on the volumetric strain of selected aggregates and water content determined from WRCs, calculation of the aggregate saturation was carried out. The aggregate saturation was investigated along the wetting path (for both ESEM and WRC measurements), because it was not affected by the presence of inter-aggregate water up to very low suctions. The calculation of aggregate saturation comprised the following steps.

(*a*) The water content corresponding to each value of suction applied in the ESEM chamber was calculated by interpolation from the wetting path of WRCs.

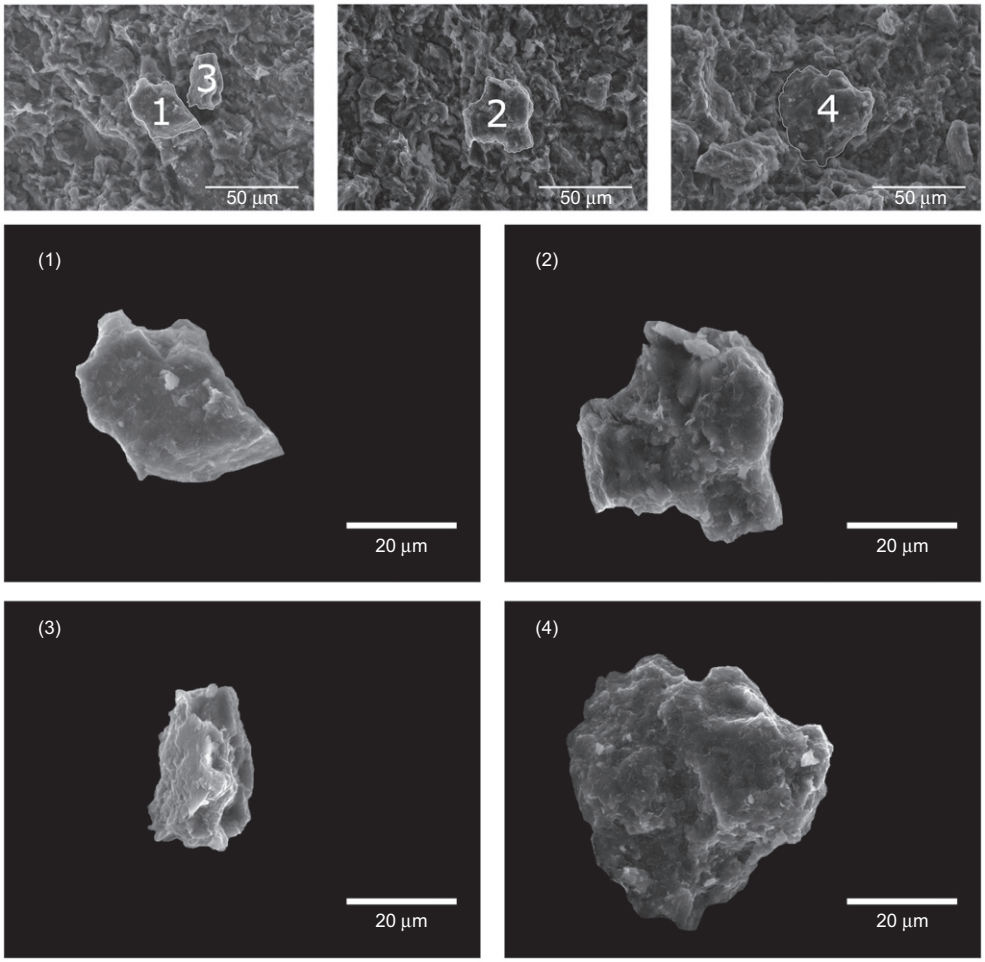

Fig. 14. Aggregates of the initial dry density 1·9 g/cm^3 samples selected for calculation of volume strain

For all of the aggregates studied, the suctions just before water entered the macropores was considered as a threshold state, in which aggregates were fully saturated, but the inter-aggregate pores were dry. This state corresponded to 3·85 MPa for low-density samples and 7·8 MPa for high-density samples.

(*b*) The volume of micropores was then calculated with the assumption of full saturation of aggregates from the water content at the threshold state. At this state, the calculated S_r was equal to one by definition (see Fig. 16).

(*c*) Subsequently, the volume change of the aggregates for each higher suction was calculated from ESEM microphotograph analysis (Fig. 15). The corresponding water content for each particular suction value was interpolated from WRC. Based on these values, the degree of saturation could be calculated for each aggregate and each suction level along the wetting path.

Despite the assumptions adopted in the volume strain estimation, including full saturation of the microstructure at the water-expulsion value of suction, dry inter-aggregate space and spherical shape of the aggregates, the calculation of S_r for all eight aggregates gives relatively consistent results (Fig. 16). This indicates that during wetting the samples were unsaturated down to the values of suction between 10 MPa and 60 MPa, the air expulsion value of suction being higher for samples with high dry density. These values are lower compared to the assumption of fully saturated aggregates up to the suctions of 80–100 MPa (Delage *et al*., 1998; Mašín & Khalili, 2015).

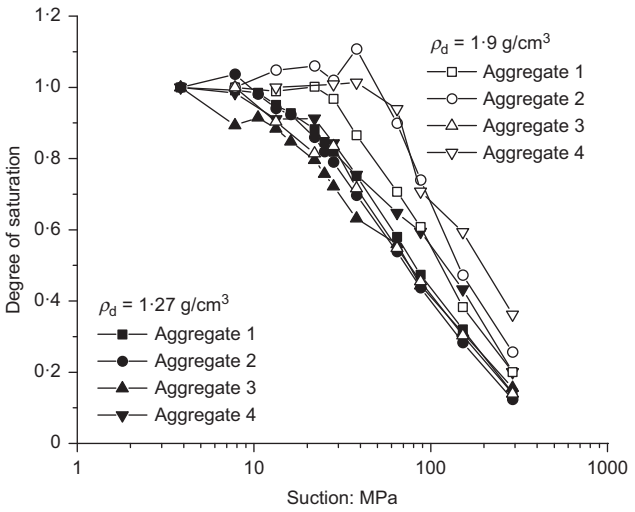

Fig. 16. Degree of saturation of aggregates during wetting evaluated from a combination of ESEM and WRC measurements

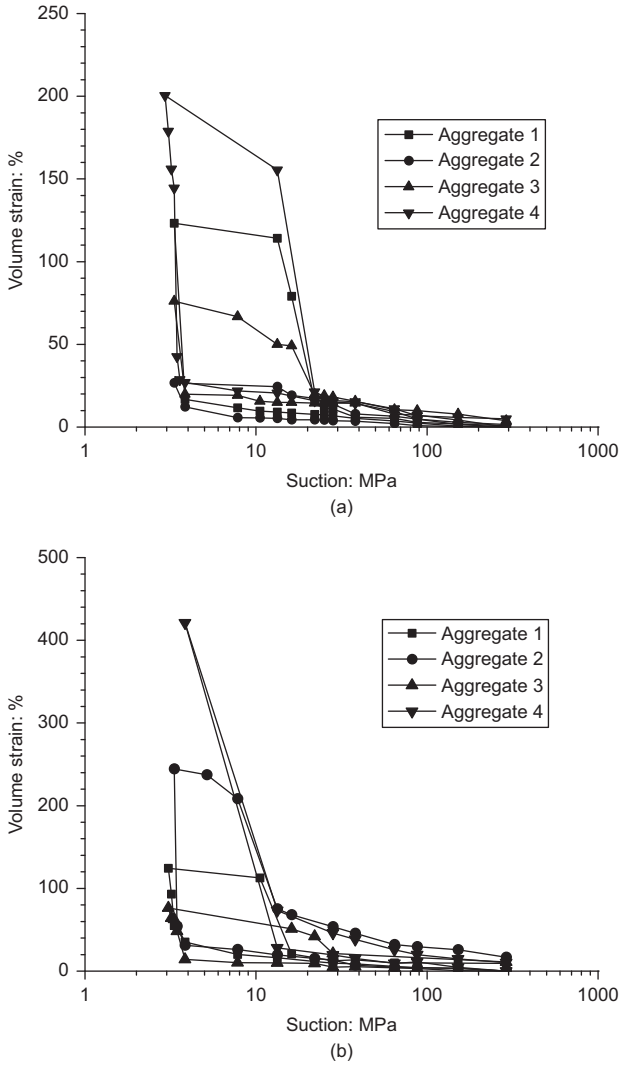

Fig. 15. Volume strain plotted against suction for compacted bentonite along wetting and drying paths: (a) initial $\rho_d = 1{\cdot}27$ g/cm^3; (b) initial $\rho_d = 1{\cdot}90$ g/cm^3

CONCLUDING REMARKS

In this paper, the authors have presented the results of water retention measurements along with void ratio measurements, MIP tests and ESEM micrographs of the Czech B75 calcium–magnesium bentonite at various initial dry densities. Results of the methods were quantitatively analysed and compared, leading to the following main conclusions.

(*a*) Apart from the inter-lamellar pores, which are not accessible to the adopted observation methods, two main pore families could be identified. Their transition pore size was suction dependent (0·07 to 0·3 μm for suctions varying between 286·7 and 3·29 MPa). The micropores were practically insensitive to compaction and only the largest micropores were sensitive to suction. The smaller macropores were sensitive to compaction only, whereas the larger macropores were sensitive to both compaction and suction.

(*b*) During wetting from the as-compacted state, the macroporosity remained completely dry up to very low values of suction (3·29 MPa).

(*c*) During wetting from the as-compacted state the micropores were found to be unsaturated up to the suction values between 10 to 60 MPa.

(*d*) Both macropores and micropores contributed to sample volume changes during suction change. Although the micropore volume change appeared to be reversible, permanent deformation remained on the macropore level. The wetting–drying cycle caused macroporosity loosening, whereas the oven-drying–wetting cycle caused densification of the largest macropores.

(*e*) Oven drying at 105°C and subsequent wetting was found to have little effect on the bentonite microstructure, apart from its effect on the largest macropores, which may be attributed to the mechanical hysteresis effects.

ACKNOWLEDGEMENTS

This project receives funding from the Euratom research and training programme 2014–2018 under grant agreement no. 745942. The first author acknowledges support by the grant no. 846216 of the Charles University Grant Agency. Institutional support by the Center for Geosphere Dynamics (UNCE/SCI/006) is greatly appreciated. Dr Sedlářová of the University of Chemistry and Technology (Prague) and Dr Plachý of the Czech Agriculture University are acknowledged for the MIP testing and sample preparation, respectively.

NOTATION

D	entrance pore diameter
e	void ratio
e_0	initial void ratio
I_p	plasticity index
P	intrusion pressure
R	molar gas constant
S_r	degree of saturation
S_t	total suction
s	suction
T	absolute temperature
V_i	volume of aggregate at stage i
V_0	volume of aggregate at initial state
w_c	water content
ε_v	volume strain
θ_{nw}	contact angle between mercury and soil surface
ρ_d	dry density
ρ_s	particle density
ρ_w	density of water
σ_{Hg}	surface tension of mercury
ω	molecular mass of water vapour

REFERENCES

Alonso, E. E., Vaunat, J. & Gens, A. (1999). Modelling the mechanical behaviour of expansive clays. *Engng Geol.* **54**, No. 1–2, 173–183.

Alonso, E. E., Pereira, J. M., Vaunat, J. & Olivella, S. (2010). A microstructurally based effective stress for unsaturated soils. *Géotechnique* **60**, No. 12, 913–925, https://doi.org/10.1680/geot.8.P.002.

ASTM (2004). C914-95: Standard test method for bulk density and volume of solid refractories by wax immersion. West Conshohocken, PA, USA: ASTM International.

Cui, Y. J. (2017). On the hydro-mechanical behaviour of MX80 bentonite-based materials. *J. Rock Mech. Geotech. Engng* **9**, No. 3, 565–574.

Cuisinier, O. & Laloui, L. (2004). Fabric evolution during hydromechanical loading of a compacted silt. *Can. Geotech. J.* **28**, No. 6, 483–499.

Delage, P., Audiguier, M., Cui, Y. J. & Howat, M. D. (1996). Microstructure of a compacted silt. *Can. Geotech. J.* **33**, No. 1, 150–158.

Delage, P., Howat, M. D. & Cui, Y. J. (1998). The relationship between suction and swelling properties in a heavily compacted unsaturated clay. *Engng Geol.* **50**, No. 1–2, 31–48.

Della Vecchia, G., Jommi, C. & Romero, E. (2013). A fully coupled elastic–plastic hydromechanical model for compacted soils accounting for clay activity. *Int. J. Numer. Analyt. Methods Geomech.* **37**, No. 5, 503–535.

Dieudonne, A. C., Della Vecchia, G. & Charlier, R. (2017). Water retention model for compacted bentonites. *Can. Geotech. J.* **54**, No. 7, 915–925.

Gatabin, C., Talandier, J., Collin, F., Charlier, R. & Dieudonné, A. C. (2016). Competing effects of volume change and water uptake on the water retention behaviour of a compacted MX-80 bentonite/sand mixture. *Appl. Clay Sci.* **121**, 57–62.

Gens, A. & Alonso, E. E. (1992). A framework for the behaviour of unsaturated clays. *Can. Geotech. J.* **29**, No. 6, 1013–1032.

Hattab, M., Hammad, T., Fleureau, J. M. & Hicher, P. Y. (2013). Behaviour of a sensitive marine sediment: microstructural investigation. *Géotechnique* **63**, No. 1, 71–84, https://doi.org/10.1680/geot.10.P.104.

Hausmannova, L. & Vasicek, R. (2014). Measuring hydraulic conductivity and swelling pressure under high hydraulic gradients. *Geological Society, London, Special Publications* **400**, 293–301, https://doi.org/10.1144/SP400.36.

Juang, C. H. & Holtz, R. D. (1986). A probabilistic permeability model and the pore size density function. *Int. J. Numer. Analyt. Methods Geomech.* **10**, No. 5, 543–553.

Komine, H. & Ogata, N. (1999). Experimental study on swelling characteristics of sand–bentonite mixture for nuclear waste disposal. *Soils Found.* **39**, No. 2, 83–97.

Li, J., Yin, Z. Y., Cui, Y. & Hicher, P. Y. (2017). Work input analysis for soils with double porosity and application to the hydro-mechanical modeling of unsaturated expansive clays. *Can. Geotech. J.* **54**, No. 2, 173–187.

Lin, B. & Cerato, A. B. (2014). Applications of SEM and ESEM in microstructural investigation of shale-weathered expansive soils along swelling-shrinkage cycles. *Engng Geol.* **177**, 66–74.

Lloret, A. & Villar, M. V. (2007). Advances on the knowledge of the thermo-hydro-mechanical behaviour of heavily compacted 'FEBEX' bentonite. *Phys. Chem. Earth* **32**, No. 8–14, 701–715.

Lloret, A., Villar, M. V., Sánchez, M., Gens, A., Pintado, X. & Alonso, E. E. (2003). Mechanical behaviour of heavily compacted bentonite under high suction changes. *Géotechnique* **53**, No. 1, 27–40, https://doi.org/10.1680/geot.2003.53.1.27.

Manca, D., Ferrari, A. & Laloui, L. (2016). Fabric evolution and the related swelling behaviour of a sand/bentonite mixture upon hydro-chemo-mechanical loadings. *Géotechnique* **66**, No. 1, 41–57, https://doi.org/10.1680/jgeot.15.P.073.

Mašín, D. (2013). Double structure hydromechanical coupling formalism and a model for unsaturated expansive clays. *Engng Geol.* **165**, 73–88.

Mašín, D. (2017). Coupled thermohydromechanical double-structure model for expansive soils. *ASCE J. Engng Mech.* **143**, No. 9, 04017067.

Mašín, D. & Khalili, N. (2015). Swelling phenomena and effective stress in compacted expansive clays. *Can. Geotech. J.* **53**, No. 1, 134–147.

Monroy, R., Zdravkovic, L. & Ridley, A. (2010). Evolution of microstructure in compacted London Clay during wetting and loading. *Géotechnique* **60**, No. 2, 105–119, https://doi.org/10.1680/geot.8.P.125.

Montes-H, G. (2005). Swelling–shrinkage measurements of bentonite using coupled environmental scanning electron microscopy and digital image analysis. *J. Colloid Interface Sci.* **284**, No. 1, 271–277.

Montes-H, G., Geraud, Y., Duplay, J. & Reuschle, T. (2005). ESEM observations of compacted bentonite submitted to hydration/dehydration conditions. *Colloids Surf. A: Physicochem. Engng Aspects* **262**, No. 1–3, 14–22.

Nowamooz, H. & Masrouri, F. (2010). Relationships between soil fabric and suction cycles in compacted swelling soils. *Engng Geol.* **114**, No. 3, 444–455.

OIML (The International Organization of Legal Metrology) (1996). *The scale of relative humidity (RH) of air certified against saturated salt solutions*. Paris, France: OIMLR 121.

Přikryl, R. & Weishauptová, Z. (2010). Hierarchical porosity of bentonite-based buffer and its modification due to increased temperature and hydration. *Appl. Clay Sci.* **47**, No. 1–2, 163–170.

Romero, E. (1999). *Characterisation and thermo-hydro-mechanical behaviour of unsaturated Boom-clay: an experimental study.* PhD thesis, Universitat Politecnica de Catalunya, Barcelona, Spain.

Romero, E. & Simms, P. H. (2008). Microstructure investigation in unsaturated soils: a review with special attention to contribution of mercury intrusion porosimetry and environmental scanning electron microscopy. *Geotech. Geol. Engng* **26**, No. 6, 705–727.

Romero, E. & Vaunat, J. (2000). Retention curves of deformable clays. In *Experimental evidence and theoretical approaches in*

unsaturated soils. Proceedings of an international workshop on unsaturated soils (eds A. Tarantino and C. Mancuso), pp. 91–106. Rotterdam, the Netherlands: A.A. Balkema.

Romero, E., Gens, A. & Lloret, A. (1999). Water permeability, water retention and microstructure of unsaturated compacted Boom clay. *Engng Geol.* **54**, No. 1, 117–127.

Romero, E., Della Vecchia, G. & Jommi, C. (2011). An insight into the water retention properties of compacted clayey soils. *Géotechnique* **61**, No. 4, 313–328, https://doi.org/10.1680/geot.2011.61.4.313.

Sánchez, M., Gens, A., Villar, M. V. & Olivella, S. (2016). Fully coupled thermo-hydro-mechanical double-porosity formulation for unsaturated soils. *Int. J. Geomech.* **16**, No. 6, D4016015.

Seiphoori, A., Ferrari, A. & Laloui, L. (2014). Water retention behaviour and microstructural evolution of MX-80 bentonite during wetting and drying cycles. *Géotechnique* **64**, No. 9, 721–734, https://doi.org/10.1680/geot.14.P.017.

Simms, P. H. & Yanful, E. K. (2001). Measurement and estimation of pore shrinkage and pore distribution in a clayey till during soil–water-characteristic curve tests. *Can. Geotech. J.* **38**, No. 4, 741–754.

Simms, P. H. & Yanful, E. K. (2005). A pore-network model for hydromechanical coupling in unsaturated compacted clayey soils. *Can. Geotech. J.* **42**, No. 2, 499–514.

Stastka, J. & Smutek, J. (2015). Experimental works with bentonite pellets at the CEG. *Proceedings of the LUCOEX conference and workshop – full-scale demonstration tests in technology development of repositories for disposal of radioactive waste*, Oskarshamn, Sweden, pp. 179–184.

Sun, H., Mašín, D. & Boháč, J. (2017). Experimental characterization of retention properties and microstructure of the Czech bentonite B75. In *Proceedings of the 19th international conference on soil mechanics and geotechnical engineering, Seoul 2017* (eds W. Lee, J.-S. Lee, H.-K. Kim and D.-S. Kim), pp. 1249–1252. Seoul, Korea: Korean Geotechnical Society.

Tang, A. M. & Cui, Y. J. (2005). Controlling suction by the vapour equilibrium technique at different temperatures and its application in determining the water retention properties of MX80 clay. *Can. Geotech. J.* **42**, No. 1, 287–296.

Villar, M. V. (2007). Water retention of two natural compacted bentonites. *Clays Clay Miner.* **55**, No. 3, 311–322.

Villar, M. V. & Lloret, A. (2001). Variation of the intrinsic permeability of expansive clays upon saturation. In *Clay science for engineering* (eds K. Adachi and M. Fukue), pp. 259–266. Rotterdam, the Netherlands: Balkema.

Villar, M. V., Gomez-Espina, R., Campos, R., Gutierrez-Nebot, L. & Barrios, I. (2014). Retention curves of bentonite under a microstructural perspective. In *Unsaturated soils* (eds N. Khalili, A. R. Russell and A. Khashghalb), vol. 2, pp. 989–994. Leiden, the Netherlands: CRC Press/Balkema.

Wang, Q., Cui, Y. J., Tang, A. M., Li, X. L. & Ye, W. M. (2014). Time- and density-dependent microstructure features of compacted bentonite. *Soils Found.* **54**, No. 4, 657–666.

Watt, G. R., Griffin, B. J. & Kinny, P. D. (2000). Charge contrast imaging of geological materials in the environmental scanning electron microscope. *Am. Miner.* **85**, No. 11–12, 1784–1794.

Fractal characteristics of pore structure of compacted bentonite studied by ESEM and MIP methods

Manuscript submitted to Acta Geotechnica on 2. 2. 2018 and accepted on 1. 7. 2019 by:

Haiquan Sun[1]
PhD student

Tel: +420221951556
Email: haiquan.sun@natur.cuni.cz

David Mašín[1] (corresponding author)
Associate Professor

Tel: +420221951552
Email: masin@natur.cuni.cz

Jan Najser[1]
Senior Lecturer

Tel: +420221951555
Email: najser@natur.cuni.cz

Vilém Neděla[2]
Researcher

Tel: +420 541 514 333
Email: vilem@isibrno.cz

Eva Navrátilová[2]
Researcher

Tel: +420 541 514 333
Email: navratilovae@isibrno.cz

[1] Faculty of Science
Charles University, Prague
Albertov 6, 128 43 Prague
Czech Republic

[2] Institute of scientific instruments
The Czech Academy of Sciences
Královopolská 147, 612 64 Brno
Czech Republic

Abstract

In this paper, we aim to clarify microstructure of bentonite from Cerny vrch deposit in the Czech Republic. We adopt results of ESEM and MIP experiments performed at various suctions along wetting and drying paths on bentonite samples compacted from powder to two different initial dry densities. The data were used for quantification of fractal dimension characteristics of pores of different sizes. Two different methods of calculating fractal dimension were used for MIP data and one method was used for evaluation of ESEM images. Fractal dimensions obtained from MIP data, combined with the measured pore size density functions, allowed us to identify two different pore families: micropores and macropores. Macropores can be further subdivided to fine macropores and coarse macropores based on fractal analysis. The pore systems were further distinguished by different responses to suction changes and to compaction effort. In general, we observed slight increase of fractal dimension with increasing suction and with increasing dry density.

Key words: bentonite, fractal dimension, suction, ESEM, MIP, microstructure

1. Introduction

Over the past few decades, bentonite has been an extensively studied material, thanks to its application as a buffer material in the planned repositories of spent nuclear fuel. It is now well accepted that bentonite structure is composed of different pore families. Typically, two predominant pore sizes are identified: macropores, formed between silt-sized aggregates of clay particles, and micropores, which represent the pore system within these aggregates. This distinction has been a basis for development of models describing mechanical and coupled hydro-mechanical behaviour of these materials [1-7].

Although the simple distinction of two pore systems is efficient for model formulation, various recent studies indicate that the pore structure of bentonite and its evolution during wetting and drying cycles is actually more complex. Wang et al [8] identified four major pore sizes in MX80 bentonite. Similarly, four pore sizes were suggested by [9] for bentonite from Czech deposit. Lloret and Villar [10] observed emergence of a new mode in pore size density function during wetting, located between two pore size peaks of as-compacted material. This is consistent with observation by [11], who

identified that bi-modal pore size distribution curve of bentonite transforms to monomodal after saturation. Similarly conclusions reached other researchers at different soil types [12-14]. In the cited studies, it was observed that mono-modal distribution transforms back to bi-modal in subsequent drying. However, Seiphoori et al [15] and Burton et al [16] observed that the double porosity structure did not recover when drying after wetting. Romero et al [14] assumed two pore families in compacted Boom clay, but elaborated more on selection of delimiting pore size between micropores and macropores. Detailed review of the microstructure of compacted unsaturated clays has been presented by [17].

In this work, we studied microstructure of Czech bentonite from Cerny vrch deposit, denoted as B75. This bentonite has been used as a buffer material in Mock-Up-Josef model of nuclear waste repository [18]. Microstructure determines pore shape, pore specific surface and pore size distribution. These properties are related to the cation exchange capacity, permeability and sorption capacity, which are important properties considered in the design of high level nuclear waste repositories. Most of the bentonite microstructure evaluation is based on quantification of global quantities (like micro- and macrovoid ratio), or on visual evaluations of ESEM images and pore size distributions measured by MIP method. In this work, we aim for a more quantitative evaluation using a fractal theory. It gives us better insight into the pore structure and it also allows us to better identify different pore families based on their sizes, which is a supporting argument for microstructurally-based bentonite material models.

The fractal theory was first introduced by [19]. The Euclidian or topological dimension is an integer; one represents line, two represents surface and three represents volume. However, the fractal dimension is a real number, for a line its value varies between 1 and 2, for surface varies between 2 and 3. The fractal dimension can be used to analyse the pore systems of porous medium based on self-similarity of pore geometry. Fractal dimension has been proven to be an efficient tool to describe and study the pore irregularity and surface roughness of different porous materials, such as the heterogeneities of pore spaces in sedimentary rocks [20-22], the fractal characteristic of micropores on the fracture surface of sandstone [23-25], the fractal description of particle fragmentation related to fracture energy [26] and shear strength [27]and the methane and gas adsorption of coals [28-30]. The fractal dimension of clay related to its structure has also been studied by many researchers [31-33,17,34-35].

Various techniques have been applied to analyse the pore structure of compacted bentonite. One of the methods is based on the digital image analysis using scanning electron microscopy (SEM) [36,33,37,38,30], environmental scanning electron microscopy (ESEM) [17,38,39] or transmission electron microscopy (TEM) [40] microphotographs. The other common methods include evaluation of mercury intrusion porosimetry test (MIP) [44] and the nitrogen gas adsorption-desorption tests [41-43]. Among all the methods, SEM, ESEM and MIP are most frequently used to investigate the pore structures of compacted bentonite [45,38,62]. Because bentonite is a clay sensitive to water, the pore structure would change with changing water content. The advantage of ESEM to SEM is that in ESEM the relative humidity can be controlled observing the fabric change with time or relative humidity, while with SEM we can only observe dry samples. The image analysis can only show two-dimensional pictures and local information, which doesn't represent complete 3D structure of the pores.

In this paper, we adopted results of ESEM and MIP methods to study bentonite microstructure using fractal theory. The ESEM method was selected as a representative photography method, giving detailed insight into the pore shape and structure, but providing only 2D images. MIP method was selected to supplement ESEM method, as it provides 3D information on pore sizes, which is however expressed in terms of cumulative volumes only, without information on pore shapes. Experiments on samples with different initial dry densities under different relative humidity conditions reported by [46] were adopted to evaluate the fractal characteristics.

2. Materials

The commercial compacted Czech bentonite B75 was used in this study. The montmorillonite content was around 60% and initial water content about 10%. The chemical composition of bentonite B75 is shown in Table 1 and the cation exchange capacity is shown in Table 2.

The bentonite powder was used to prepare the compacted samples. This powder was uniaxially compacted in the laboratory mould to reach the desired initial dry densities of 1.27 g/cm^3 and 1.90 g/cm^3. The initial water content of the powder was around 10%. The height of the sample was 10 mm and the diameter was 50 mm. The manufactured bentonite was cut into small pieces. Tests on two groups of samples were evaluated in this paper. Samples from the first group were dried in the oven for more than 48 hours

with temperature of 105 °C. Subsequently, the dried samples were put in the dessicator with suction control by different vapor pressure. Samples from the second group were initially compacted, directly dried by two different methods (freeze drying and oven drying) and adopted in ESEM measurements. All the evaluations were done on samples from the first group, except of evaluations from Sec. "The effect of oven drying and freeze drying on fractal dimension using ESEM images".

Each dessicator was in equilibrium with different chemical saturated salt solution corresponding to different relative humidity. In this paper, suctions of 286.7 MPa, 38 MPa and 3.29 MPa were imposed on the compacted bentonite for wetting path. After equilibration, the samples for MIP tests were freeze-dried before the measurement. The detailed information and procedures were described in [46].

3. Methods

3.1 Environmental Scanning Electron Microscopy

The Environmental Scanning Electron Microscopy (ESEM) tests have been performed using QUANTA 650 FEG scanning electron microscope at the Institute of Scientific Instruments of the Czech Academy of Sciences, Brno. Samples of compacted bentonite were equilibrated at suction of 286.7 MPa before their placement into ESEM cell. The samples were placed in a special conical holder and cooled by a Peltier stage. This holder allows minimising sample shift in conditions of very high relative humidity as well as better cooling which is necessary for sample stabilisation and repeatability of observation. Conditions of observation were kept constant throughout the experiment. The samples of the bentonites were observed in water vapour environment under increasing and then decreasing relative humidity (wetting and drying). The water vapour pressure of 93 Pa (relative humidity of 10%) was determined as optimal initial state for the experiment. Then the vapour pressure was gradually increased up to 850 Pa (relative humidity 97%). After the maximum value of the relative humidity was reached, the relative humidity was gradually decreased again down to 10%. The microphotographs were taken at each stage. The time interval between vapour pressure changes was 15 minutes. Similar interval was used by other researchers [45,38].

3.2 Mercury intrusion porosimetry tests

Mercury intrusion porosimetry (MIP) is based on the capillary law governing non-wetting liquid (with contact angle bigger than 90°) penetration into small pores. The pore entrance diameter (D) can be calculated from the intrusion pressure, p, the surface tension of mercury, σ_{Hg}, the contact angle between the mercury and soil surface, θ_{nw}, and the equivalent entrance diameter, D, $D = -(4\sigma_{Hg}\cos\theta_{nw})/P$. In this study, the θ_{nw} = 130° and σ_{Hg} = 0.484 N/m at 25 °C were considered in pore diameter calculation.

The tests were performed at the Department of Inorganic Technology at the University of Chemistry and Technology Prague (Apparatus Autopore IV, Micromeritics). All the samples for this measurement were freeze dried. The aparatures has two pressure regimes, one is the low one from 0.01 MPa to 0.2 MPa which can measure the pore radius between 100 μm and 3 μm, the other is the high regime from 0.2 MPa to 400 MPa which corresponds the pore radius between 3 μm to 1.5 nm. It is noted that the MIP method cannot detect nanopores below approx. 3 nm and these results were thus not adopted in the evaluation.

4. Fractal dimension calculation theory

4.1 Fractal dimension calculated from ESEM images

For fractal dimension analysis, the original gray scale microphotographs taken from ESEM apparatus must be transformed into binary images. The binary image contains only two colors, black and white. Typically, the black color represents pores and the white color represents the solid skeleton. The gray scale threshold value was used to separate the solid and pore. An appropriate global threshold value was chosen to apply to all microphotographs.

There are many methods to calculate fractal dimension from microphotographs taken from ESEM tests, such as box counting method [30], probability statistic method [47] or Fourier method [48]. The box counting method, which has been widely used in rocks and soils [30] characteristing the pore distribution and fractal dimension, was chosen to determine the fractal dimension of compacted bentonite. The procedures of calculating fractal dimension are shown in Figure 1 including the original gray scale ESEM photo (Figure 1 (a)), the binary image after applied threshold value (Figure 1(b)) and the binary image used in box counting to measure the fractal dimension (Figure 1 (c)). The

size of the box was denoted as ε. The number of boxes which cover solid surface was then marked as N(ε). This procedure was repeated with different box sizes with corresponding covering counts N obtained, so the box counting fractal dimension D_b could be calculated with equation (1) [49,30]:

$$D_b = -\lim_{\varepsilon \to 0} \frac{\ln(N(\varepsilon))}{\ln(\varepsilon)} \quad (1)$$

The fractal dimension equals to the slope of natural logarithms N(ε) versus ε.

In this paper, the free software ImageJ [50] and associated open source plugins [51] were used to process the microphotographs and to analyse the results.

4.2 Fractal dimension calculated from MIP data

The results of MIP were often used for the analysis of pore structure of materials like coal, clay and so on. For calculation of the pore surface fractal dimension Ds, the equation (2) based on Menger fractal dimension model has usually been used by other researchers [52,33,53,17], which is related to derivative of the cumulative intrusion volume as a function of intrusion pressure.

$$\log[(dV_p/dV_{max})/d_p] \propto (D_s - 4)\log p \quad (2)$$

where p is the intrusion pressure (MPa), V_p is the cumulative volume intruded for a given pressure p, V_{max} is the total volume intruded for the maximum intrusion pressure and D_s is the surface fractal dimension. The interval zones of self-similarity and the different types of pore structure can be obtained from the linear sections of $\log[(dV_p / dV_{\max}) / dp]$ versus log p, the slope of which yield the values of fractal dimension.

Another method is based on thermal dynamic relation of porous medium in the process of mercury intrusion porosimetry [54]. It is considering the equilibrium of surface energy increased by mercury intrusion and work done by surroundings, which is used to calculate the fractal dimension (denoted as D_z) using the following equations,

$$\ln(W_n) = \ln(Q_n) + C \quad (3)$$

$$\text{Let } Q_n = {r_n}^{2-D_z} {V_n}^{D_z/3} \quad (4)$$

$$W_n = \sum_{i=1}^{n} \bar{p}_i \Delta V \quad (5)$$

Substituting Equation (4) and (5) in to equation (3) leads to:

$$\ln(W_n/r_n^2) = D_z \ln\left(\frac{V_n^{\frac{1}{3}}}{r_n}\right) + C' \quad (6)$$

where i means i-th intrusion step, n means total intrusion number, $\overline{p_i}$ is the average intrusion pressure for ith intrusion, $\overline{p_i}\Delta V$ is the increased intrusion volume for i-th intrusion, r is the pore radius, C and C' are constants, D_z is fractal dimension calculated from thermal dynamic relations, W_n is the accumulated surface energy, Q_n is a function of pore radius and pore volume. Both these methods (Eq (2) and Eq (6)) were used for calculation of fractal dimension in this paper.

5. Results and discussion

5.1 Observation scale effects on fractal dimension using ESEM images

Figure 2 shows the ESEM microphotographs of compacted bentonite with initial dry density of 1.27 g/cm^3 under different magnifications. The pore size was measured by ImageJ software. Obviously, with magnification increase, the pore size decreases. The range of pore diameters roughly corresponding to each magnification is shown in Table 3. It is obvious from images that the compacted bentonite has multiple pore systems. The clay matrix looks homogeneous under low magnification in Figure 2 (a), but with increasing magnification, details of structure of the aggregates becomes clear. Two pore families were visually identified by [46]: macropores and micropores (see Figure 3). In this work, we investigate the data by evaluating the surface fractal dimension.

Although the microphotographs are in two dimensions, they still represent surface roughness under different magnifications. The surface fractal dimension (D_b) was used to analyse the roughness of the clay surface. Because of the 2D images, the surface fractal dimension will be between 1 and 2. The box counting method mentioned above and demonstrated in Figure 1 was used. Figures 4 and 5 show the results of box counting methods for dry density of 1.27 g/cm^3 and 1.9 g/cm^3 separately. The linear equation with the real box counting data has a high correlation coefficient of more than 0.997 for all the cases, which indicates that the pore structures of compacted bentonite has high fractal characteristics. The relation between fractal dimension and magnification for low and high dry density samples is shown in Figure 6. The results show a decrease in D_b with increasing magnification, which is followed by an increase at high

magnifications (the increase is however indicated by few data points only). D_b has a linear relationship with logarithm of magnification for both dry densities until the threshold value at magnification of 10 000 for lower dry density and 25 000 for higher dry density samples. The same linear trend was observed for soils by [55] and rocks by [22]. At low magnification, the microphotographs contain more aggregates than high magnification, which makes the surface more irregular.

Finally, we also evaluated possible effect of porosity on fractal dimension (Figure 7). This figure shows that fractal dimension does not correlate significantly with the porosity.

5.2 The effect of oven drying and freeze drying on fractal dimension using ESEM images

It is generally accepted that different drying techniques have different influence on the microstructure of compacted clays. Delage et al[56] summarized the water volume and total mercury intrusion volume of Champlain clay, which verified that freeze-drying can preserve its original micro structure. The oven drying produces large shrinkage especially for high water content samples. Keiser et al[57] studied influence of three different drying techniques (drying in ambient air, oven drying, and freeze drying) on the grain size of clay. The results showed that soil with high clay content (>39%) was sensitive to drying techniques.

Figure 8 shows microphotographs of the freeze dried and oven dried samples for medium dry density of 1.6 g/cm^3 compacted bentonite at various magnifications. The initial water content was around 10% and the samples were identical before drying. The details of freeze drying and oven drying methods were described in [46].

In order to investigate the drying method, influence of the microstructure of compacted bentonite on surface fractal dimension (D_b) was calculated on freeze dried and oven dried samples. Three initial dry densities of 1.27 g/cm^3, 1.6 g/cm^3 and 1.9 g/cm^3 with initial water content of 10% were studied. Surface fractal dimension (D_b) versus magnification for the two drying methods are shown in Figures 9 (a), (b) (c) for low, medium and high dry density samples respectively. The fractal dimension decreased with increasing magnification regardless of the drying method. The fractal dimension was almost the same at low magnification, while the difference is increasing with magnification increase. The fractal dimension calculated from oven dried samples show

a higher value at higher magnification for medium and high dry density samples, while little effect is observed on low dry density samples. Recall that, the higher the fractal dimension, the rougher the surface is. The fractal dimension reflects that oven drying may change the original structure which makes the clay surface more irregular with higher pore surface fractal dimension.

5.3 The effect of wetting and drying cycles on fractal dimension using ESEM images

In general, the water content influences the behavior of compacted bentonite. The volume of soil increases when water is adsorbed and consequently, the microstructure is affected. The clay surface was observed in different stages under various relative humidities. The compacted oven-dried bentonite was first equilibrated at suction of 286.7 MPa, then it was placed into ESEM cell and it was controlled by wetting path (relative humility 10% to 97%) and subsequently by drying path (relative humidity was decreased back to 10%).

The bentonite samples compacted to dry density of 1.27 g/cm^3 and 1.9 g/cm^3 were used for ESEM observation. 24 microphotographs were taken for each dry density for both wetting and drying paths. The suction can be calculated from relative humidity using equation (7),

$$S_t = (RT\rho_w / \omega)\ln(1/RH) \qquad (7)$$

where s_t is the total suction (kPa); R is the molar gas constant, which equals to 8.314462 J/(mol K); T is the absolute temperature (K); ρ_w is the density of water; ω is the molecular mass of water vapour, which equals to 18.016 g/mol; RH is relative humidity of the system which is defined as the ratio of partial pressure of vapour over saturation vapour pressure.

Considering the sharpl increase of swelling volume of bentonite aggregates under high relative humidity conditions [46], the magnification of 2500 was chosen for observation. It is detailed enough when compared with lower magnifications and still the aggregates can be tracked along all relative humidities. Fractal dimension was evaluated from each microphotograph with magnification of 2500. The surface fractal dimension (D_b) versus suction are shown in Figure 10 for dry densities of 1.27 g/cm^3 and 1.9 g/cm^3. It can be seen, that for low dry density samples the fractal dimension decreased with

wetting. Fractal dimension increased with drying up to suction of approx. 20 MPa and then it dereased again for suction above 100 MPa. For highly dry density samples, fractal dimension is independent of suction for wetting, while sharp increase followed by a slight decrease of D_b can be seen during drying. Similar phenomenon was observed by [58] for cement paste and [59] for unsatured soils.

5.4 Suctions effects on fractal dimension in MIP measurements

5.4.1 Pore surface fractal dimension D_s from MIP

The porosity measured by mercury intrusion porosimetry is shown in table 4. It decreases with increasing dry density and suction. Figure 11 shows the original data of mercury capillary pressure versus mercury intrusion saturation degrees. The mercury intrusion saturation degree equals to the intruded mercury volume divided by the total intruded mercury volume.

Figures 12 and 13 show the pore surface fractal dimension D_s versus pore radius from MIP data for low and high dry density samples respectively. The fractal dimension was calculated from Eq (2). An attempt was made to identify the interval zones of self-similarity and the different type of pore structure from the linear sections in Figures 12 and 13. There, the values of D_s can be calculated from the curve slope. Figures 12 and 13 show the surface fractal dimension of dry density samples of 1.27 g/cm^3 and 1.90 g/cm^3 under three suctions. According to [60], a surface fractal dimension, D_s, which equals to 2 represents a fissure like porosity, while D_s equals to 3 is representing a more space filling volumetric pore structure. This concept was used in boom clay by [33] [17] and in unsatured soils by [34].

In order to describe different pore size domains based on pore geometry, data for both dry densities and all suctions were plotted in one graph (Figure. 14(a)). Both micropores and macropores can be clearly identified based on the fractal analysis. Inside the family of macro-pores, fine macropores and coarse macropores can be distinguished (indicated by dashed lines in Figures 12 and 14). Micropores are represented by parallel regression lines of all samples demonstrating similar values of surface fractal dimension D_s. It shows that this domain representing the pores inside the aggregates is compaction-insensitive. However, close to the micro-macro boundary, D_s of high density samples is influenced by applied suction (Figure 15). The size of the micro-pores domain is

therefore not uniquely defined and depends on the value of suction. These results confirm quantitatively the qualitative evaluation presented by [46].

The actual value of surface fractal dimension for both pore families is shown in Figure 16. As is also clear from Fig. 14, the pores exhibit approximately similar value of D_s. The D_s of macropores is slightly higher in the case of low density samples, whereas for high dry density, the values are similar. When the trend of D_s values is compared to the fractal dimension D_b calculated from box counting method (Figure 6), the D_b decreased with magnification and then a little increased (this increase can, however, be caused by small number of pores present in the evaluated images at high magnificantions). This trend is supported by D_s values, which are higher for bigger pore radius and lower for smaller pore radius. The micropores exhibit similar D_s values in the range 2.72-3.0 (Table 5, Figure 16). It suggests similar shape of the pores, which can be described as a space-filling volumetric structure [17]. The fractal dimension of macropores in low dry density samples at high suction exceeds the value of 3. This can be caused by more complex shape of these pores, which can be also combined with microcracks. Similar values were observed by [17].

5.4.2 Thermal fractal dimension from MIP (Eq (6))

Figures 17 and 18 show the pore surface fractal dimension D_z calculated from equation (6). The D_z is constant in all pressure ranges compared with the fractal dimension D_s. The correlation coefficient of fitting curves of these MIP data is greater than 0.98, which indicates a good linear relationship. The fractal dimension D_z of low and high dry density samples under each suction level is shown in Figure 19. It can be seen that, as a general trend, fractal dimension slightly increased with the suction increase. This observation is consistent with pore surface fractal dimension (D_b) evaluated using ESEM images in wetting tests, but no clear comparison is possible with D_b evaluated using drying tests and with D_s variation with suction. High dry density samples have higher fractal dimension than low dry density samples.

5.5 Discussion on the differences between results obtained using ESEM and MIP methods

The MIP method is characterizing indirectly the features of the solid-pore interfaces. The MIP provides a limited information, however, as it describes the surface/volume accessible by mercury only. The fractal dimension calculation is based on ideal fractal

structure of Menger Sponge, which may vary with the scale D_s. The thermal fractal dimension (D_z) calculated from MIP is based on the thermal dynamic relation of porous medium in the process of mercury intrusion, which makes the fractal dimension constant through all the pressure range. Contrary, the fractal dimension calculated from ESEM uses images which covers most macropores (2500X), but the smallest and largest pores cannot be quantified using this magnification, it only represents 2D sections through the samples and evaluation of pore boundaries is subject to uncertainties. The fractal dimensions obtained from both results thus can't be compared directly, however, both give an insight in the pore structure characteristics quantifiable by these methods.

6. Conclusions

The fractal dimension of compacted bentonite using samples of different dry densities was studied by ESEM and MIP tests at different suctions. The influence of pore size, wetting and drying cycles, suction and compaction energy on fractal dimension were discussed and analysed. The different approaches based on box counting method (D_b), Menger fractal dimension model (D_s) and thermal dynamic relation (D_z) were applied. The following conclusions can be made:

1) The fractal analysis using box counting method on ESEM images proved high fractal characteristics of bentonite pore system. The fractal dimension decreases with increasing magnification due to more smooth and regular structures observed under high magnifications. However, the fractal dimension increases again when approaching extremely high magnifications. The effect of freeze drying and oven drying was investigated, showing higher fractal dimension of oven dried samples. This indicates certain change of the pore structure of the samples exposed to oven drying.

2) Two pore size domains were defined based on the fractal analysis of MIP data, namely micropores and macropores. The macropores can be subdivided to fine macropores and coarse macropores. The zones influenced by suction and different compaction energy where identified. An estimation of pore geometry of different size domains can be made based on the value of fractal dimension D_s. Pore size domains determined from fractal analysis correlates with size domains obtained by visual evaluation of MIP distribution curves. The fractal analysis of MIP data thus proved to

be a useful tool, which complements the information obtained from MIP distribution curves.

3) Comparison of the different methods of fractal analysis is problematic, due to different nature of methods used in evaluation. We can however conclude that often fractal dimension decreases slightly with decreasing suction (D_b evaluated using wetting tests, D_s on low density samples and D_z for both dry densities).

Acknowledgments

This project receives funding from the Euratom research and training programme 2014-2018 under grant agreement No 745942. The first author acknowledges support by the grants No. 846216 and 1476119 of the Charles University Grant Agency. Institutional support by Center for Geosphere Dynamics (UNCE/SCI/006) is greatly appreciated.

References

1. Gens A, Alonso EE (1992) A framework for the behaviour of unsaturated expansive clays. *Canadian Geotechnical Journal*, *29*(6), 1013-1032

2. Alonso E., Vaunat J, Gens A (1999) Modelling the mechanical behaviour of expansive clays. Engineering Geology 54, 173–183

3. Della VG, Jommi C, Romero E (2013) A fully coupled elastic–plastic hydromechanical model for compacted soils accounting for clay activity. Int. J. Numer. Anal. Methods Geomech. 37 (5), 503–535

4. Mašín D (2013) Double structure hydromechanical coupling formalism and a model for unsaturated expansive clays. Engineering Geology; 165:73–88

5. Sánchez M, Gens, A, Villar MV, Olivella S (2016) Fully coupled thermo-hydro-mechanical double-porosity formulation for unsaturated soils. International Journal of Geomechanics 16 (6), D4016015

6. Mašín D (2017) Coupled Thermohydromechanical Double-Structure Model for Expansive Soils. ASCE Journal of Engineering Mechanics, 143(9), 04017067

7. Li J, Yin ZY, Cui Y, Hicher PY (2017) Work input analysis for soils with double porosity and application to the hydromechanical modeling of unsaturated expansive clays. Canadian Geotechnical Journal 54 (2), pp. 173-187

8. Wang Q, Cui YJ, Tang AM, Li XL, Ye WM (2014) Time- and density-dependent microstructure features of compacted bentonite. Soils and Foundations, Vol. 54, No. 4, 657-666

9. Přikryl R, Weishauptová Z (2010) Hierarchical porosity of bentonite-based buffer and its modification due to increased temperature and hydration. Applied Clay Science 47, No. 1-2, 163-170

10. Lloret A, Villar MV (2007) Advances on the knowledge of the thermo-hydro-mechanical behaviour of heavily compacted "FEBEX" bentonite. Physics and Chemistry of the Earth 32, 701–715

11. Manca D, Ferrari A, Laloui, L (2016) Fabric evolution and the related swelling behaviour of a sand/bentonite mixture upon hydro-chemo-mechanical loadings. Géotechnique 66, No. 1, 41-57

12. Cuisinier O, Laloui L (2004) Fabric evolution during hydromechanical loading of a compacted silt. Canadian Geotechnical Journal 28, 483–499

13. Monroy R, Zdravkovic L, Ridley A (2010) Evolution of microstructure in compacted London Clay during wetting and loading. *Géotechnique,* 60 (2), 105–119

14. Romero E, Della VG, Jommi C (2011) An insight into the water retention properties of compacted clayey soils. *Géotechnique*, *61*(4), 313

15. Seiphoori A, Ferrari A, Laloui L. (2014) Water retention behaviour and microstructural evolution of MX-80 bentonite during wetting and drying cycles. Géotechnique 64, No. 9, 721-734

16. Burton GJ, Pineda JA, Sheng D, Airey D (2015) Microstructural changes of an undisturbed, reconstituted and compacted high plasticity clay subjected to wetting and drying. Engineering Geology 193, 363-373

17. Romero E, Simms PH (2008) Microstructure investigation in unsaturated soils: A review with special attention to contribution of mercury intrusion porosimetry and environmental scanning electron microscopy. Geotechnical and Geological Engineering 26, 705–727

18. Stastka J, Smutek J (2015) Experimental works with bentonite pellets at the CEG. LUCOEX Conference and workshop – Full-scale demonstration tests in technology development of repositories for disposal of radioactive waste. Oskarshamn, Sweden. pp. 179-184

19. Mandelbrot BB (1977) Fractals: form, chance and dimension. Freeman, San Francisco

20. Wong PZ, Howard J (1986) Surface Roughening and the Fractal Nature of Rocks. Physical Review Letters 57, 637–642

21. Flavio SA, Stefan L, Gregor PE (1998) Quantitative characterization of carbonate pore systems by digital image analysis. AAPG Bulletin 82 (10), 1815–1836

22. Liu K, Ostadhassan M, Zhou J, Gentzis T, Rezaee R (2017) Nanoscale pore structure characterization of the Bakken shale in the USA. *Fuel*, *209*, 567-578

23. Katz A, Thompson AH (1985) Fractal sandstone pores: implications for conductivity and pore formation. *Physical Review Letters*, *54*(12), 1325

24. Hansen JP, Skjeltorp AT (1988) Fractal pore space and rock permeability implications. *Physical review B*, *38*(4), 2635

25. Turcotte DL (2002) Fractals in petrology. *Lithos*, *65*(3-4), 261-271

26. Xu Y (2018a) The fractal evolution of particle fragmentation under different fracture energy. Powder Technology, 323, 337-345

27. Xu Y (2018b) Shear strength of granular materials based on fractal fragmentation of particles. Powder Technology, 333, 1-8
28. Friesen W I, Mikula RJ (1987) Fractal dimensions of coal particles. *Journal of Colloid and Interface Science*, *120*(1), 263-271
29. Mahamud M, López Ó, Pis JJ, Pajares JA (2003) Textural characterization of coals using fractal analysis. *Fuel Processing Technology*, *81*(2), 127-142
30. Liu X, Nie B (2016) Fractal characteristics of coal samples utilizing image analysis and gas adsorption. *Fuel*, *182*, 314-322
31. Vallejo LE (1996) Fractal analysis of the fabric changes in a consolidating clay. *Engineering Geology*, *43*(4), 281-290
32. Hyslip JP, Vallejo LE (1997) Fractal analysis of the roughness and size distribution of granular materials. *Engineering geology*, *48*(3-4), 231-244
33. Romero MEE (1999) *Characterisation and thermo-hydro-mechanical behaviour of unsaturated Boom clay: an experimental study*. Universitat Politècnica de Catalunya
34. Farulla CA, Jommi C (2005, May) Suction controlled wetting-drying cycles on a compacted scaly clay. In *Proceedings of international conference on problematic soils*(Vol. 25, p. 27)
35. Cui ZD, Zhao LZ, Yuan L (2016) Microstructures of consolidated Kaolin clay at different depths in centrifuge model tests. Carbonates and Evaporites, 31(1), 47-60
36. Komine H, Ogata N (1999) Experimental study on swelling characteristics of sand-bentonite mixture for nuclear waste disposal. *Soils and Foundations*, *39*(2), 83-97
37. Watt GR, Griffin BJ, Kinny PD (2000) Charge contrast imaging of geological materials in the environmental scanning electron microscope. *American Mineralogist*, *85*(11-12), 1784-1794
38. Lin B, Cerato AB (2014) Applications of SEM and ESEM in microstructural investigation of shale-weathered expansive soils along swelling-shrinkage cycles. *Engineering Geology*, *177*, 66-74
39. Deng H., Hu X, Li HA, Luo B, Wang W (2016) Improved pore-structure characterization in shale formations with FESEM technique. *Journal of Natural Gas Science and Engineering*, *35*, 309-319
40. Pyun SI, Rhee CK (2004) An investigation of fractal characteristics of mesoporous carbon electrodes with various pore structures. *Electrochimica Acta*, *49*(24), 4171-4180

41. Yang F, Ning Z, Liu H (2014) Fractal characteristics of shales from a shale gas reservoir in the Sichuan Basin, China. Fuel, 115, 378-384
42. Xiang G, Xu Y, Xie S, Fang Y (2017) a Simple Method for Testing the Fractal Dimension of Compacted Bentonite Immersed in Salt Solution. Surface Review and Letters, 24(03), 1750040
43. Xu Y (2018c) Fractal Model for the Correlation Relating Total Suction to Water Content of Bentonites. Fractals, 26(03), 1850028
44. Delage P, Audiguier M, Cui YJ, Howat MD (1996) Microstructure of a compacted silt. Canadian Geotechnical Journal. 33, 150-158
45. Montes-H G (2005) Swelling–shrinkage measurements of bentonite using coupled environmental scanning electron microscopy and digital image analysis. Journal of colloid and interface science, 284(1), 271-277
46. Sun H, Mašín D, Najser J, Neděla V, Navrátilová E (2018) Bentonite microstructure and saturation evolution in wetting–drying cycles evaluated using ESEM, MIP and WRC measurements. Géotechnique, 1-14
47. Florindo JB, Bruno OM (2014) Fractal descriptors based on the probability dimension: a texture analysis and classification approach. *Pattern Recognition Letters*, *42*, 107-114
48. Schepers HE, Van Beek JH, Bassingthwaighte JB (1992) Four methods to estimate the fractal dimension from self-affine signals (medical application). *IEEE Engineering in Medicine and Biology Magazine*, *11*(2), 57-64
49. Grau J, Méndez V, Tarquis AM, Diaz MC, Saa A (2006) Comparison of gliding box and box-counting methods in soil image analysis. *Geoderma*, *134*(3-4), 349-359
50. Rasband WS, 1997-2016 ImageJ, U. S. National Institutes of Health, Bethesda, Maryland, USA, https://imagej.nih.gov/ij/
51. Karperien A. (2013) FracLac for ImageJ. Charles Sturt University
52. Korvin G (1992) *Fractal models in the earth sciences*. Elsevier Science Limited
53. Jommi C, Sciotti A (2003) A study of the microstructure to assess the reliability of laboratory compacted soils as reference material for earth constructions.
In *proceedings of the 2nd international conference on structural and construction engineering* (Vol. 3, pp. 2409-2415). Balkema
54. Zhang B, Li S (1995) Determination of the surface fractal dimension for porous media by mercury porosimetry. *Industrial & Engineering Chemistry Research*, *34*(4), 1383-1386

55. Dathe A, Eins S, Niemeyer J, Gerold G (2001) The surface fractal dimension of the soil–pore interface as measured by image analysis. *Geoderma*, *103*(1-2), 203-229
56. Delage P, Lefebvre G (1984) Study of the structure of a sensitive Champlain clay and of its evolution during consolidation. *Canadian Geotechnical Journal*, *21*(1), 21-35
57. Keiser L, Soreghan GS, Joo YJ (2014) Effects of drying techniques on grain-size analyses of fine-grained sediment. *Journal of Sedimentary Research*, *84*(10), 893-896
58. Beddoe RE, Lang K (1994) Effect of moisture on fractal dimension and specific surface of hardened cement paste by small-angle X-ray scattering. *Cement and concrete research* 24, no. 4, 605-612
59. Khoshghalb A, Pasha AY, Khalili N (2015) A fractal model for volume change dependency of the water retention curve. *Géotechnique*, *65*(2), 141-146
60. De Las Cuevas C (1997) Pore structure characterization in rock salt. *Engineering geology*, *47*(1-2), 17-30
61. Hausmannova L, Vasicek R (2014) Measuring hydraulic conductivity and swelling pressure under high hydraulic gradients. *Geological Society, London, Special Publications*, *400*, SP400-36
62. Niu, WJ., Ye, WM. & Song, X., (2019) Unsaturated permeability of Gaomiaozi bentonite under partially free-swelling conditions, Acta Geotechnica (in print, https://doi.org/10.1007/s11440-019-00788-9)

Table 1. The chemical composition of bentonite B75 [61].

Component	Weight(%)
SiO_2	51.91
Al_2O_3	15.52
Fe_2O_3	8.89
TiO_2	2.28
CaO	4.6
MgO	2.22
Na_2O	1.21
K_2O	1.27
P_2O_5	0.4
MnO	0.11
FeO	2.95
SO_3	0.09
$CaCO_3$	11.71
CO_2	5.15
Lost-drying	10.65

Table 2. The cation exchange capacity of bentonite B75.

Cation	mmol/100g
Ca^{2+}	47.27
Na^{+}	15.39
K^{+}	2.01
Mg^{2+}	15.80
H^{+}	<0.5

Table 3. Typical pore diameter under different magnification.

Magnification	800	1500	2500	5000	10000	25000	50000
Pore diameter (um)	10-25	6-10	4-8	2-4	1.5-3	0.5-1	0.02-0.1

Table 4. Initial porosity measured by MIP test.

	286.7	38	3.24
1.27	42.99%	46.07%	51.59%
1.90	13.75%	17.70%	23.90%

Table 5. Fractal dimension Ds with pore systems for both dry densities.

	1.27 g/cm^3		1.90 g/cm^3	
Suction/MPa	Macropores	Micropores	Macropores	Micropores
286.7	3.25	2.73	2.99	2.72
38	3.35	2.86	2.95	3.00
3.29	2.97	2.78	2.71	2.99

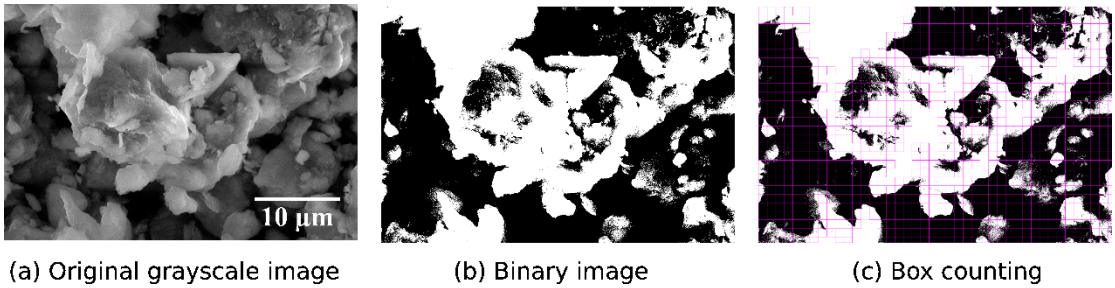

Figure 1. Examples of ESEM microphotographs of compacted bentonite used for box counting fractal dimension methods, the original gray scale image (a), binary image (b), box counting (c).

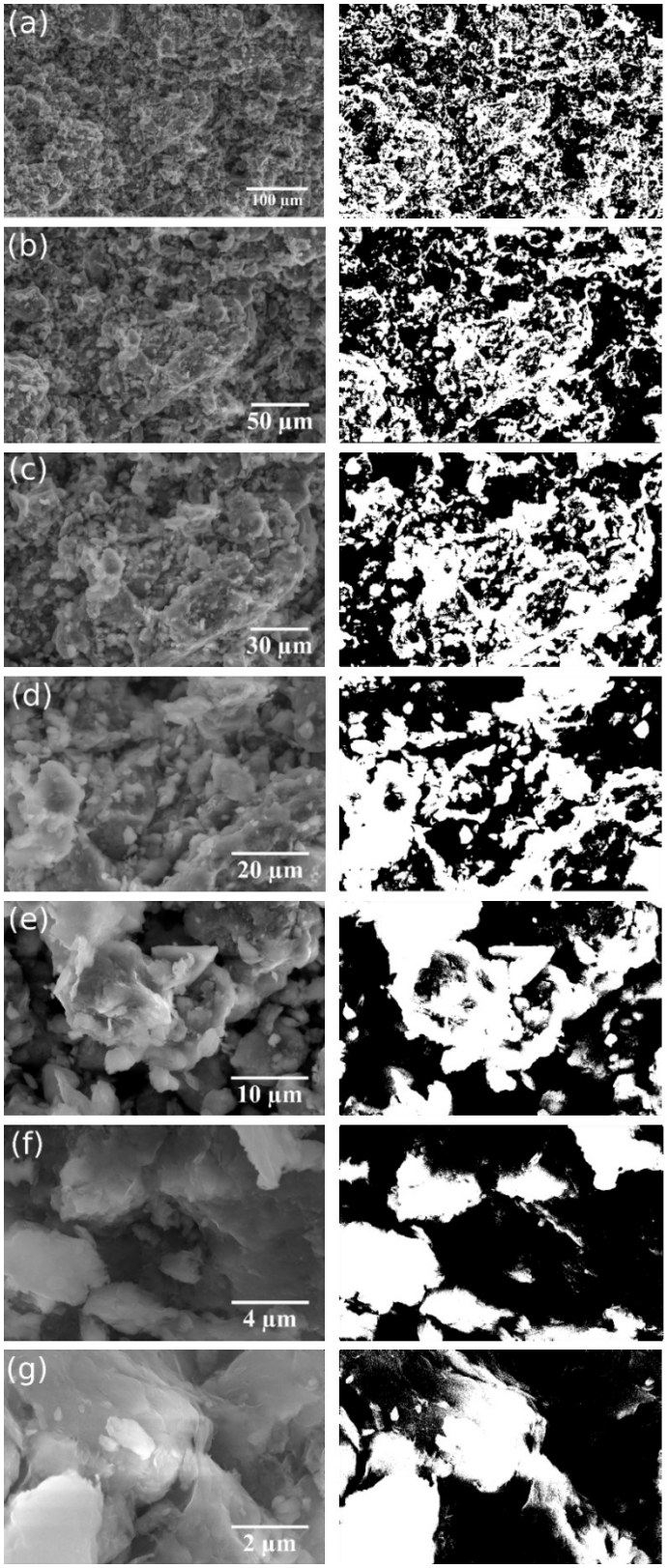

Figure 2. ESEM observation of freeze dried compacted bentonite (ρ_d = 1.27 g/cm^3) under different magnification: (a) 800X, (b) 1500X, (c) 2500X, (d) 5000X, (e)10000X, (f) 25000X, (g) 50000X. left: original grayscale images; right: binary images.

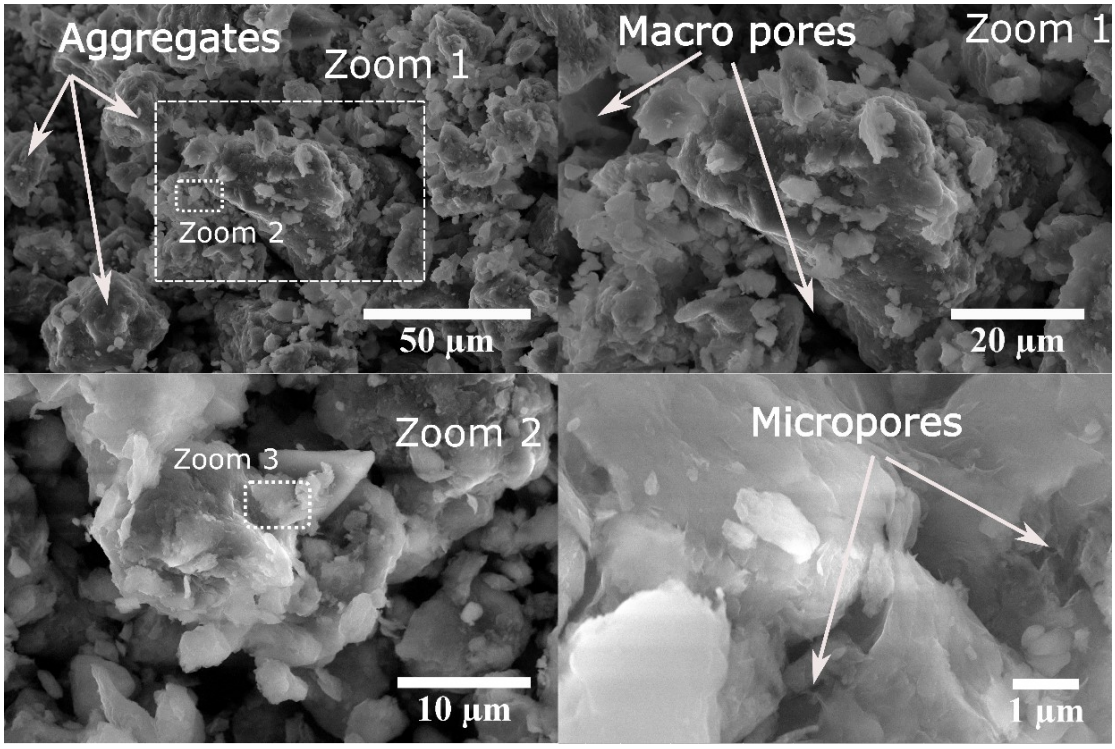

Figure 3. ESEM micrographs of compacted bentonite with a dry density of 1.27 g/cm^3 with macropores and micropores pore families[46].

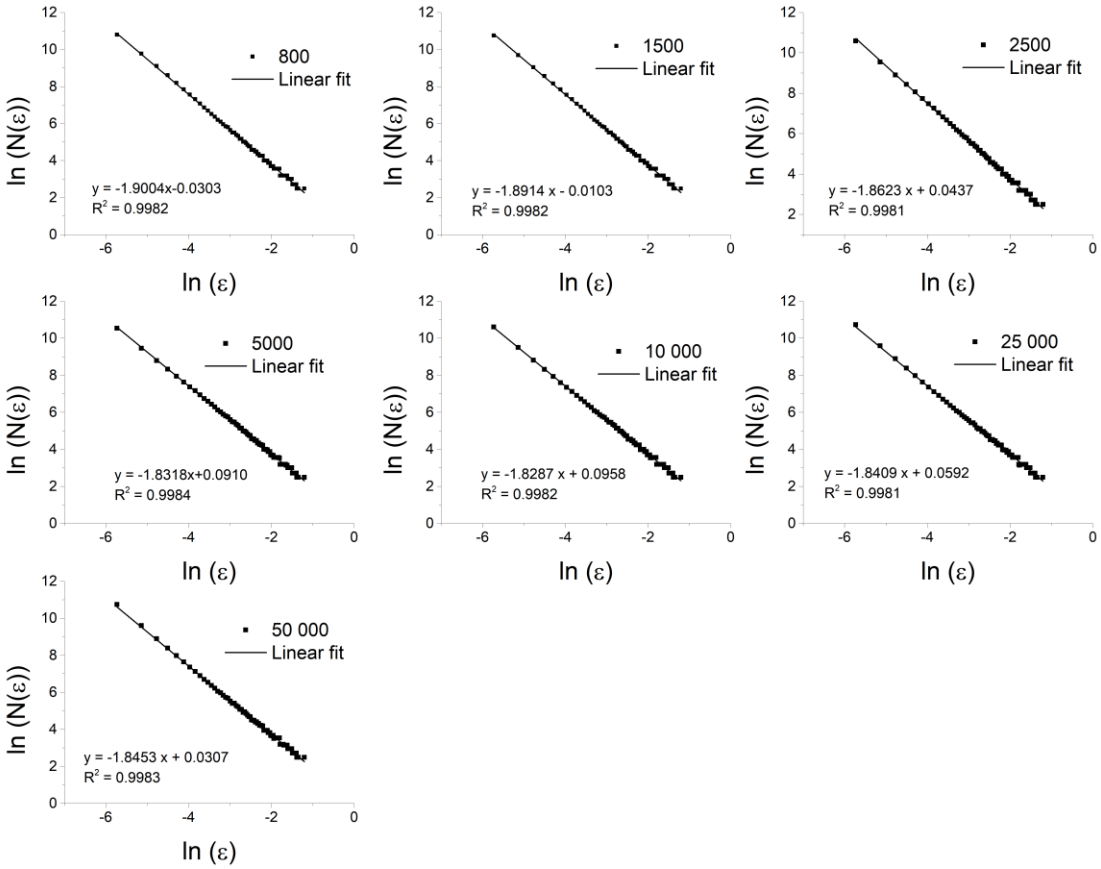

Figure 4. Surface fractal dimension (D_b) of dry density of 1.27 g/cm^3 with different magnification from ESEM microphotographs.

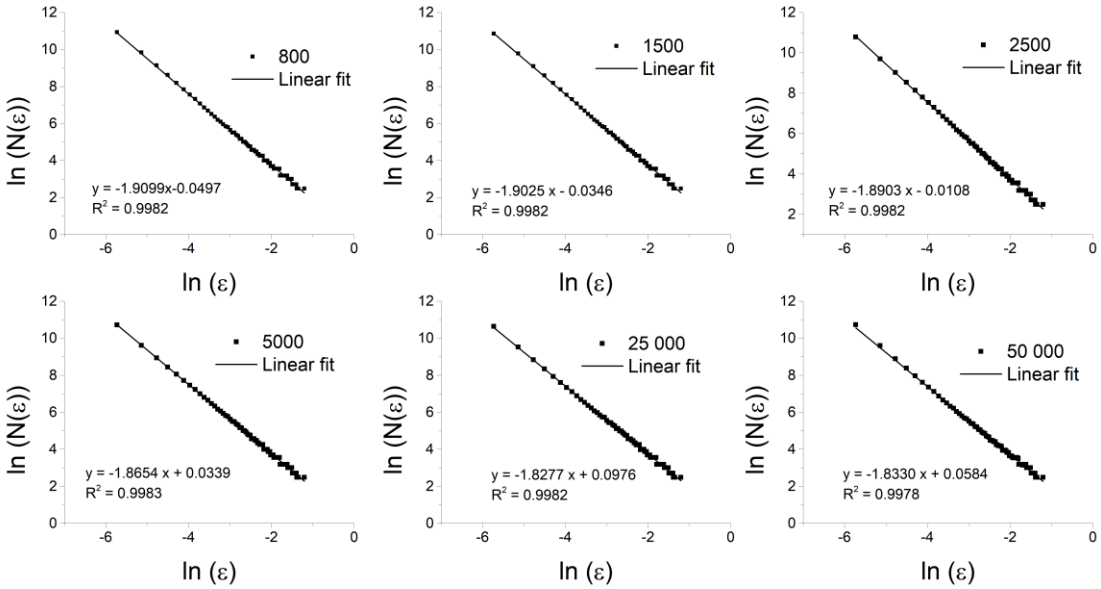

Figure 5. Surface fractal dimension (D_b) of dry density of 1.90 g/cm^3 with different magnification from ESEM microphotographs.

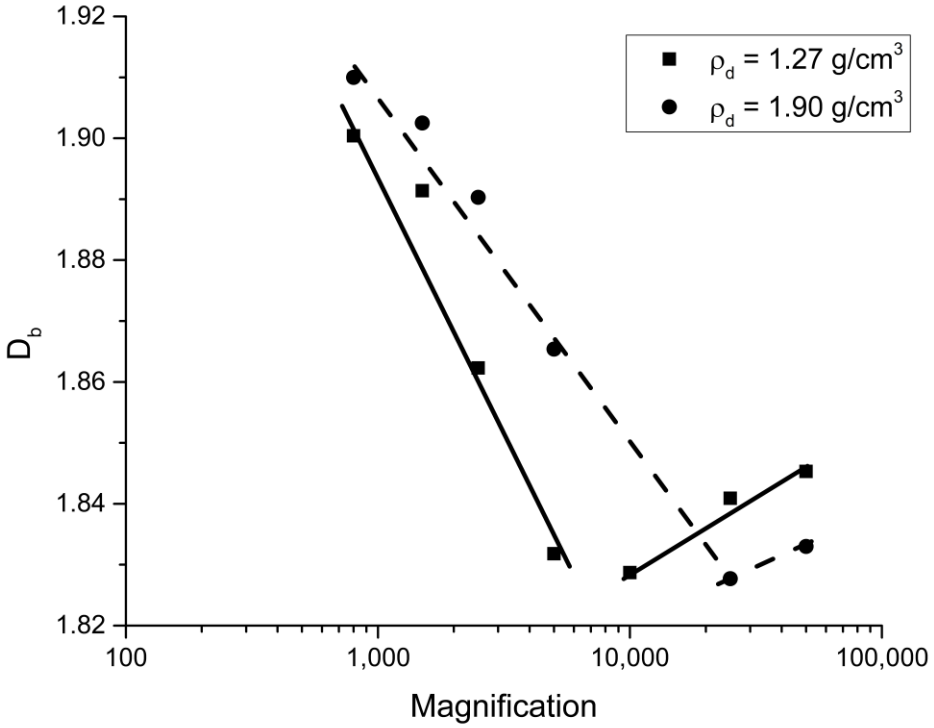

Figure 6. Surface fractal dimension (D_b) versus magnification, low dry density of 1.27 g/cm^3 (a) and high dry density of 1.9 g/cm^3 (b).

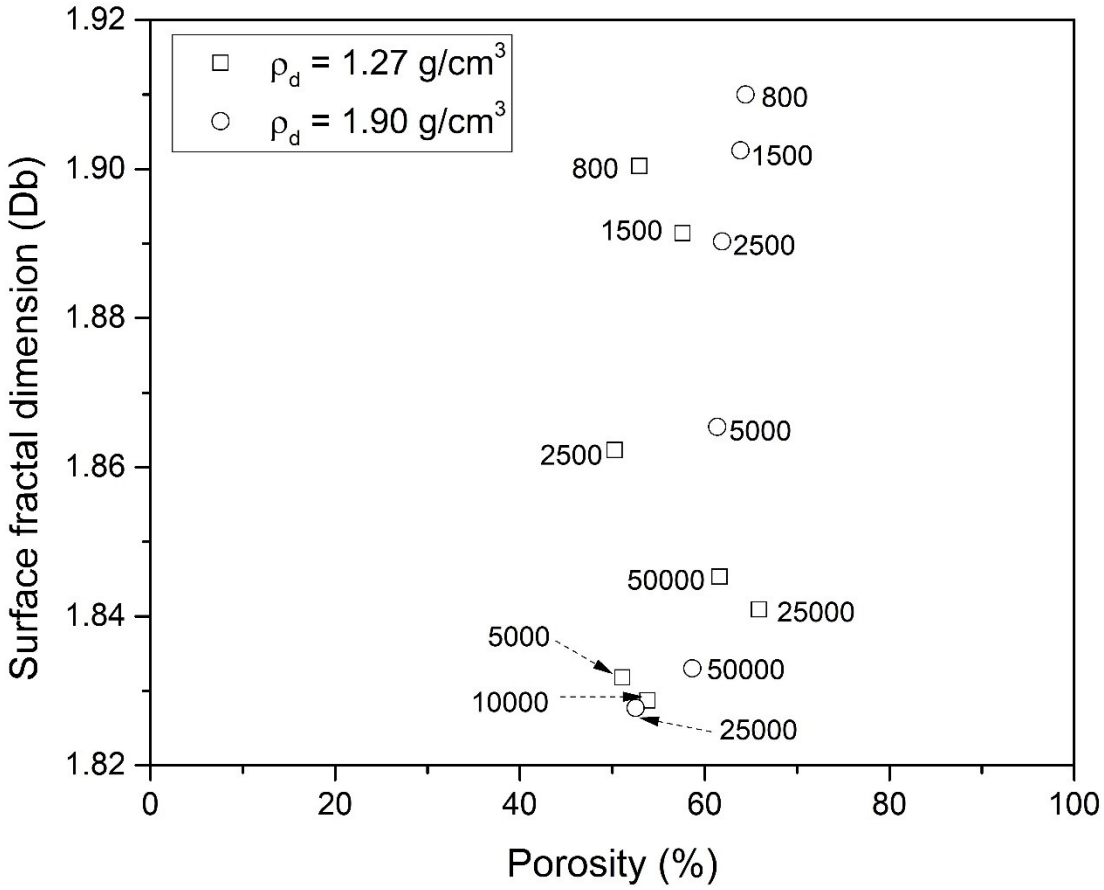

Figure 7. Porosity from binary image versus surface fractal dimension (Db).

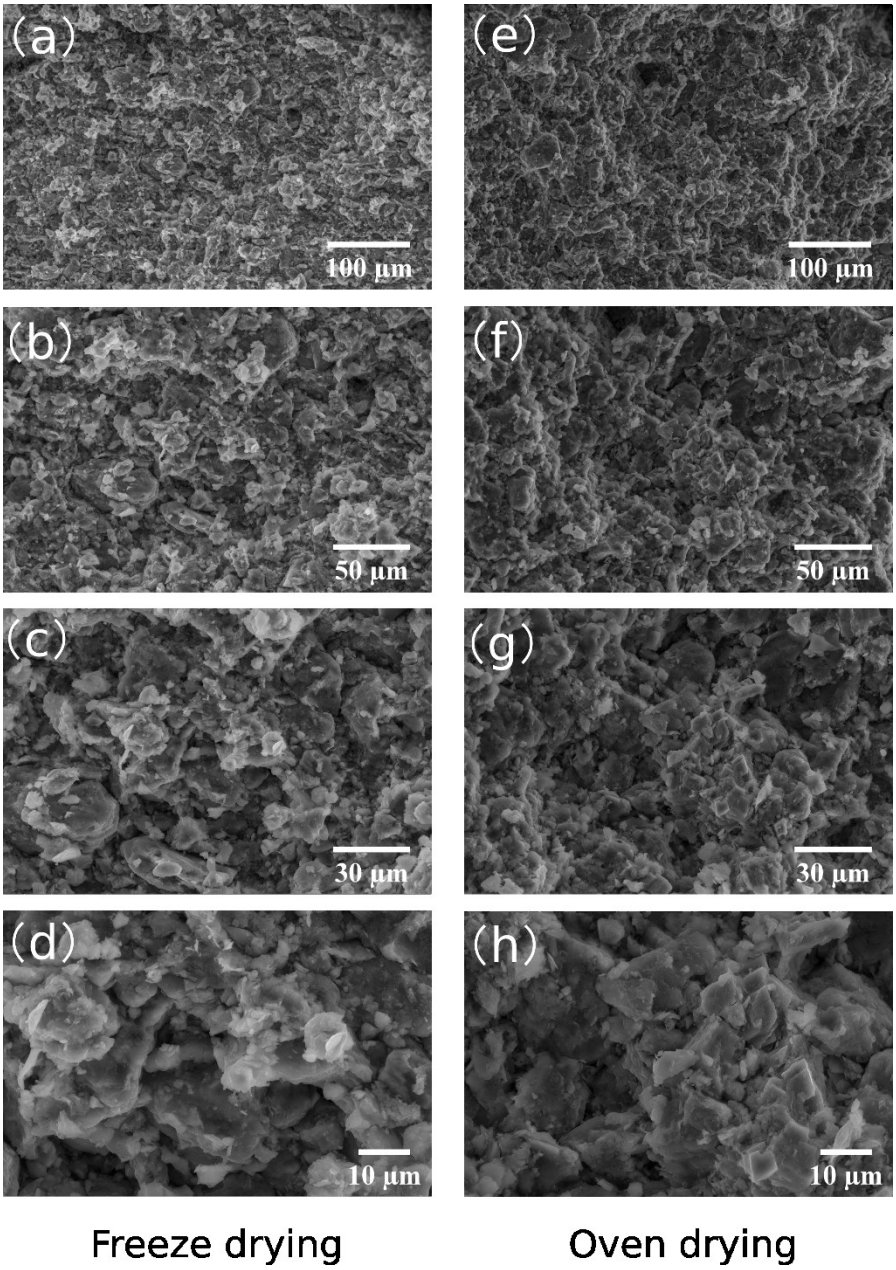

Figure 8. Dry density of 1.60 g/cm^3 bentonite dried by freeze drying (left) and oven drying (right) with magnification of 800X (a&e), 1500X (b&f), 2500X (c&g) and 5000X (d&h).

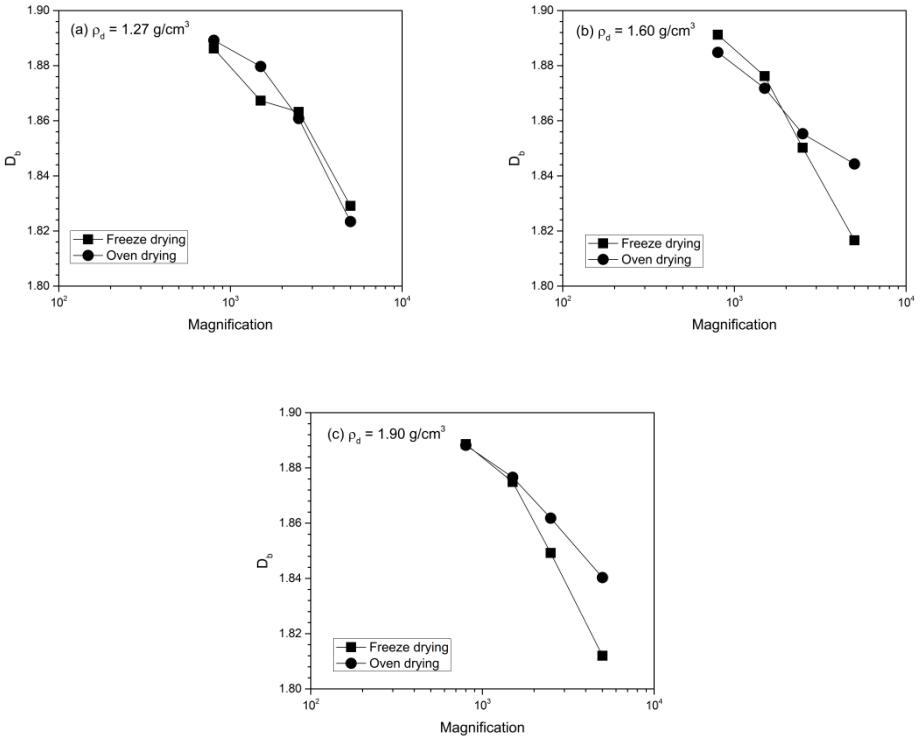

Figure 9. Surface fractal dimension (D_b) of freeze dried and oven dried samples along with magnification for both dry densities

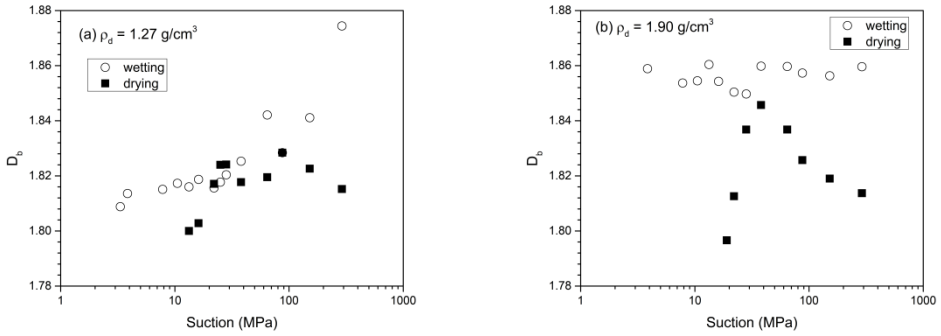

Figure 10. Surface fractal dimension (D_b) versus suction with drying and wetting cycles, low dry density of 1.27 g/cm^3 (a) and high dry density of 1.90 g/cm^3 (b).

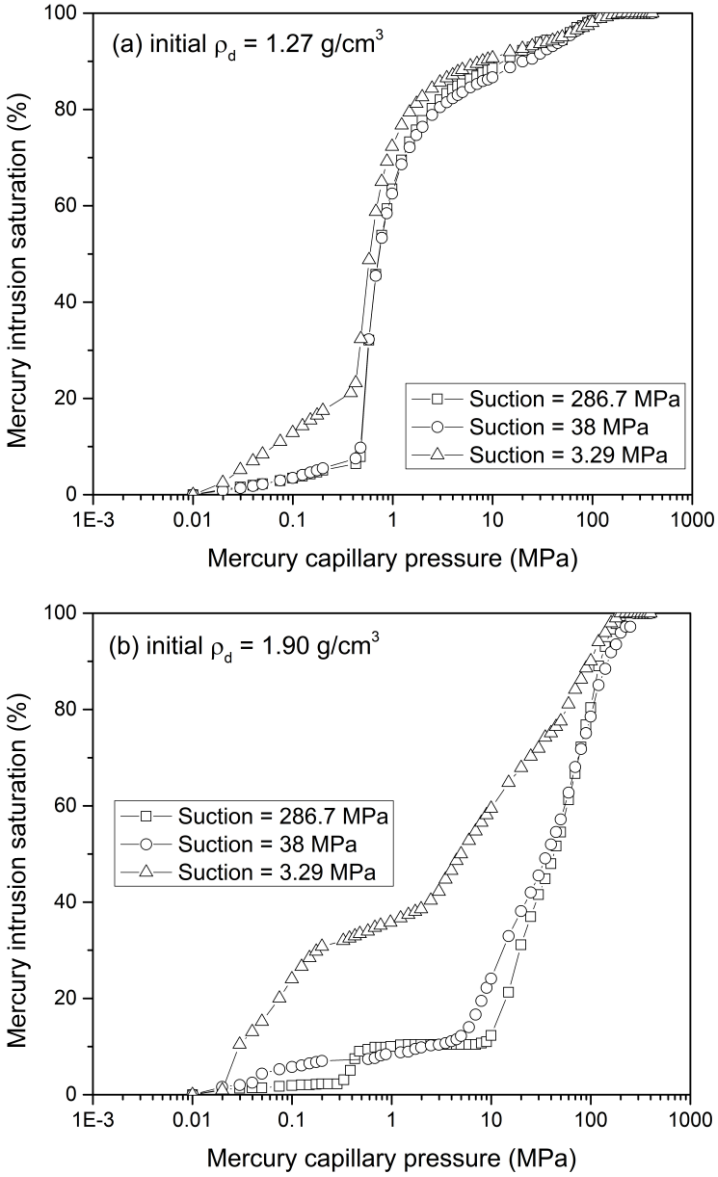

Figure 11. Mercury intrusion saturation versus mercury capillary pressure

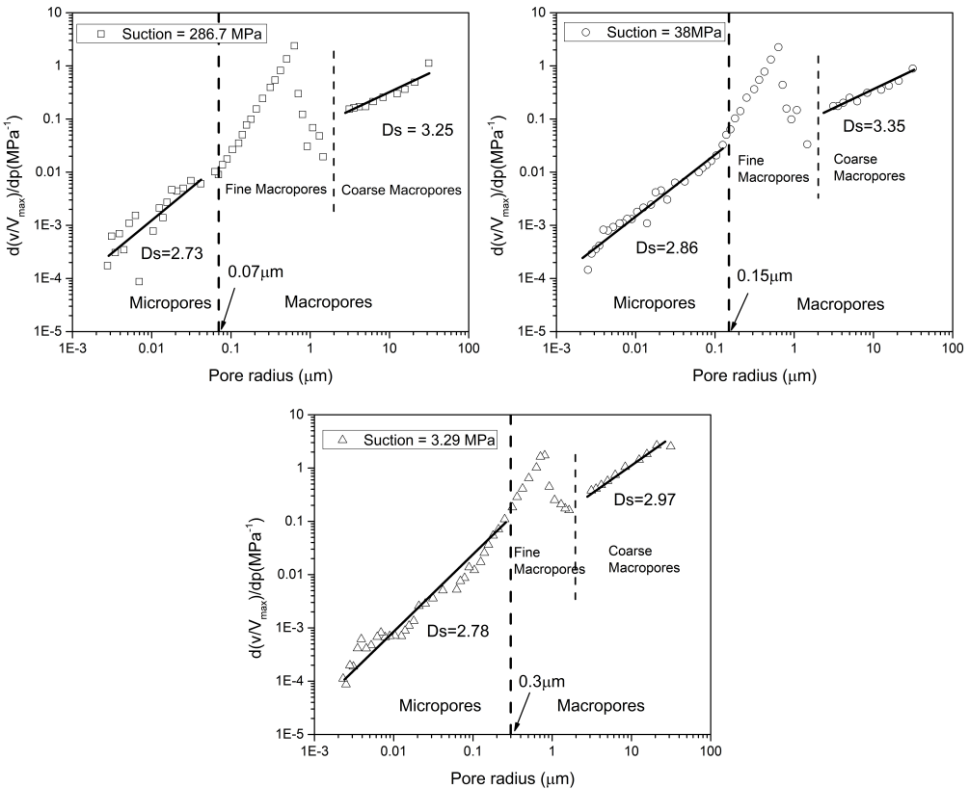

Figure 12. Fractal dimension D_s versus applied pressure for dry density of 1.27 g/cm^3 under (a) suction = 286.7MPa, (b) suction = 38MPa, (c) suction= 3.29MPa.

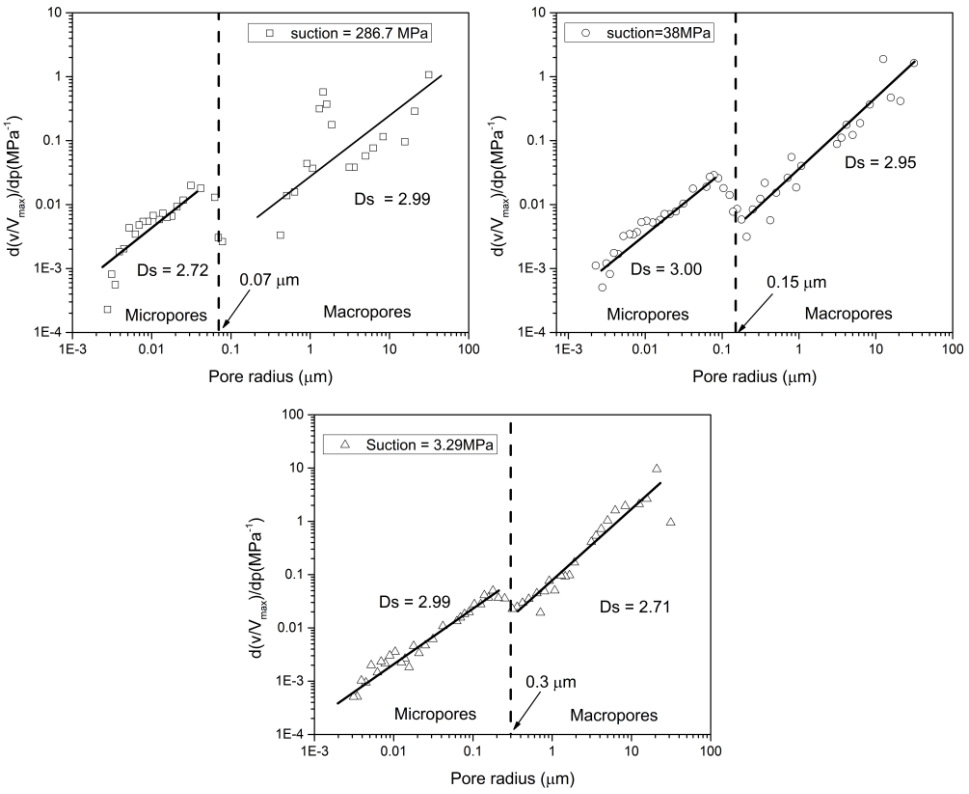

Figure 13. Fractal dimension D_s versus applied pressure for dry density of 1.90 g/cm^3 under (a) suction = 286.7 MPa, (b) suction = 38 MPa, (c) suction= 3.29 MPa.

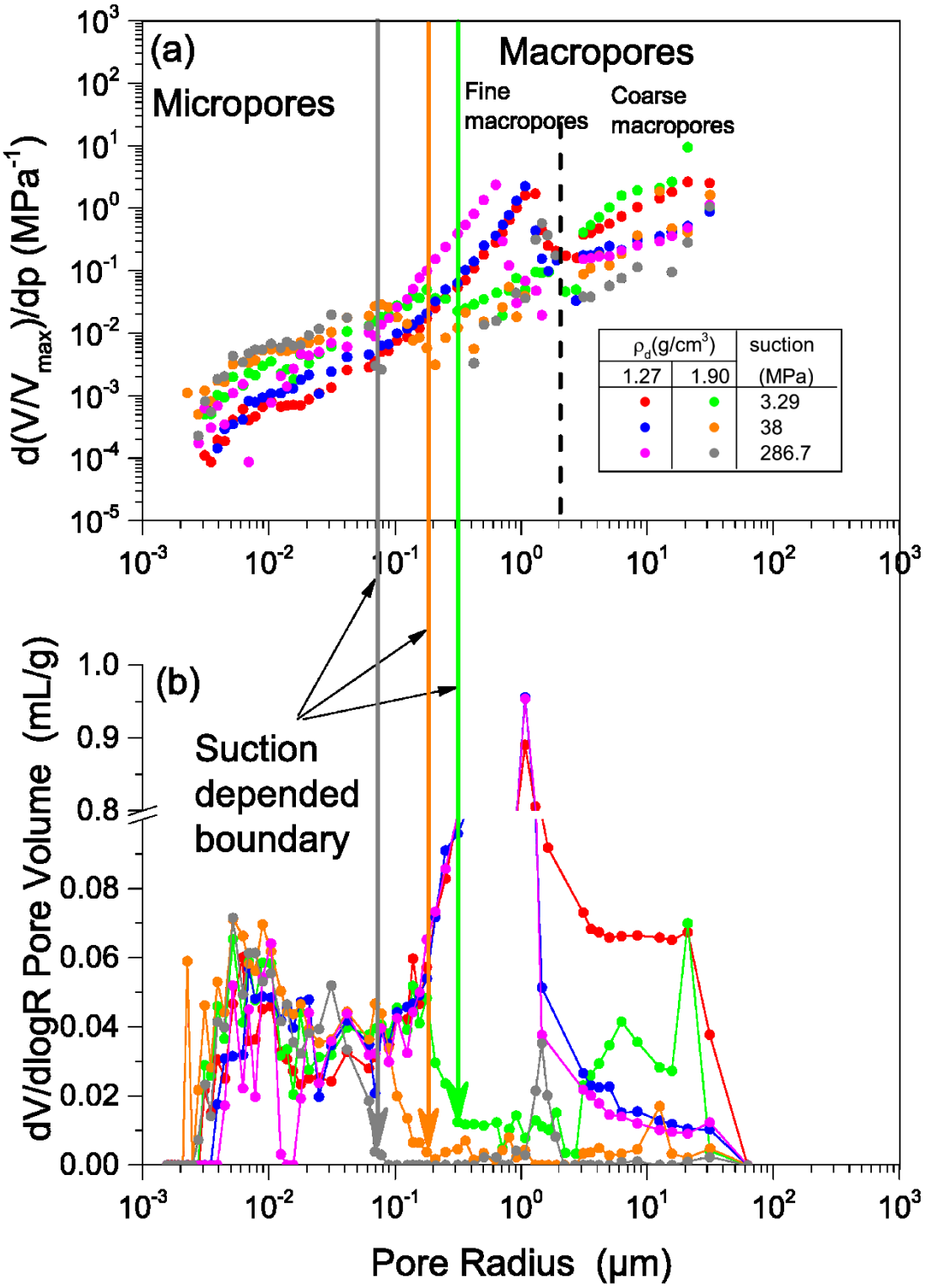

Figure 14. Fractal dimension (a) and pore size distribution (b) with pore radius under each suction level for both dry densities.

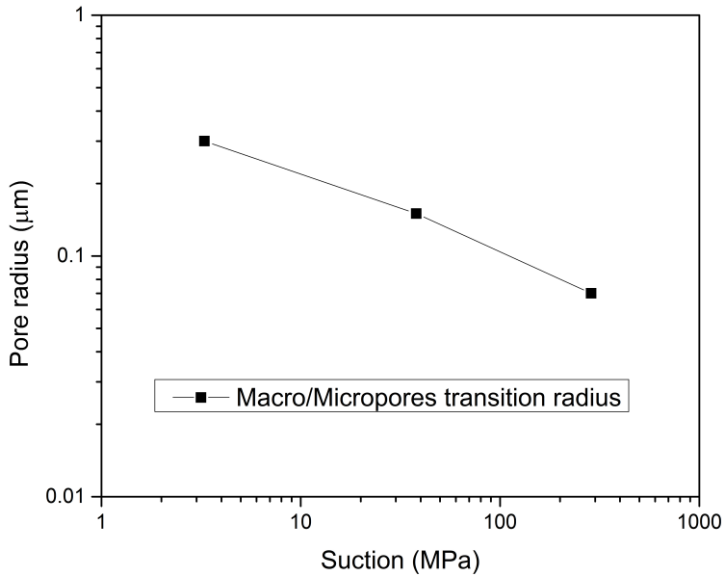

Figure 15. Transition pore radius changing with suction for high dry density.

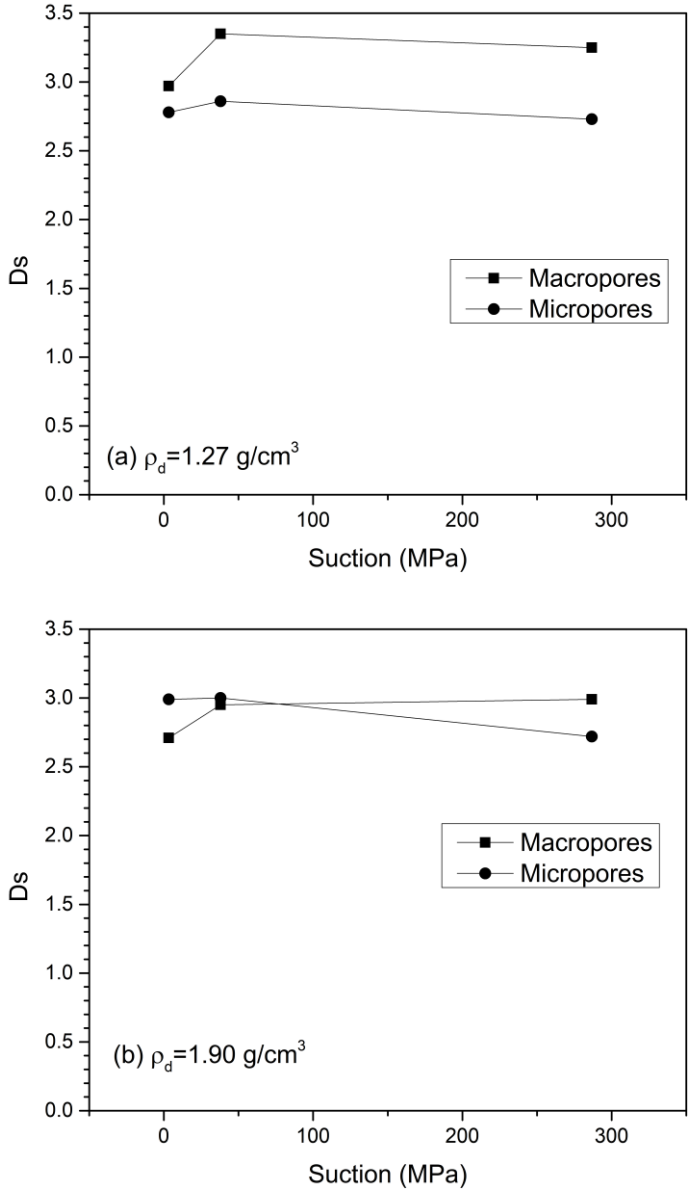

Figure 16. Fractal dimension versus suction for various pore systems (a) dry density of 1.27 g/cm^3 and (b) dry density of 1.9 g/cm^3.

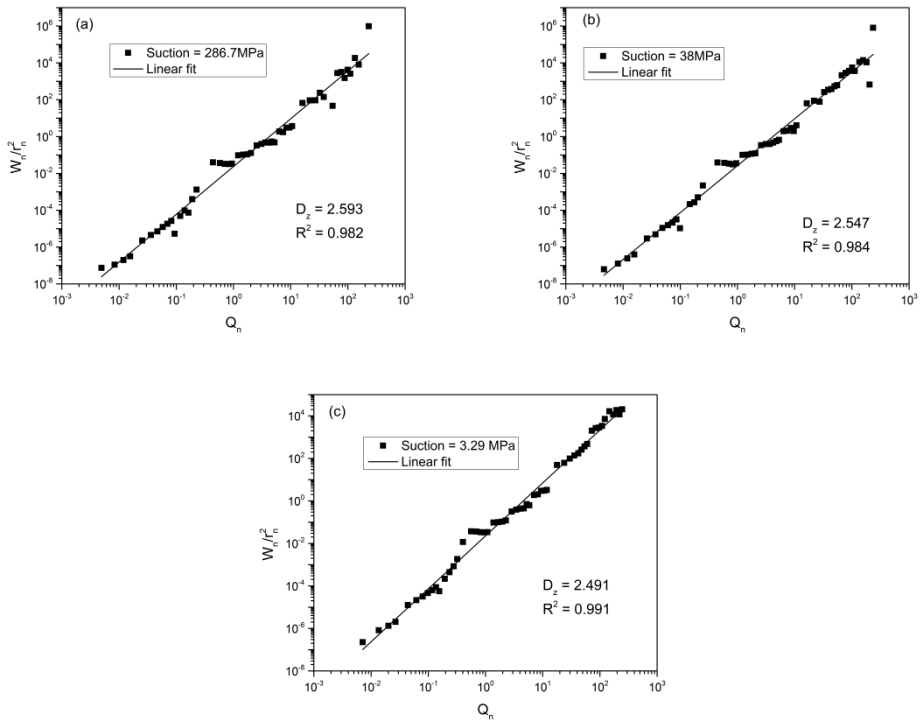

Figure 17. Fractal dimension D_z of low dry density of 1.27 g/cm^3 under (a) suction = 286.7 MPa, (b) suction = 38 MPa, (c) suction= 3.29 MPa.

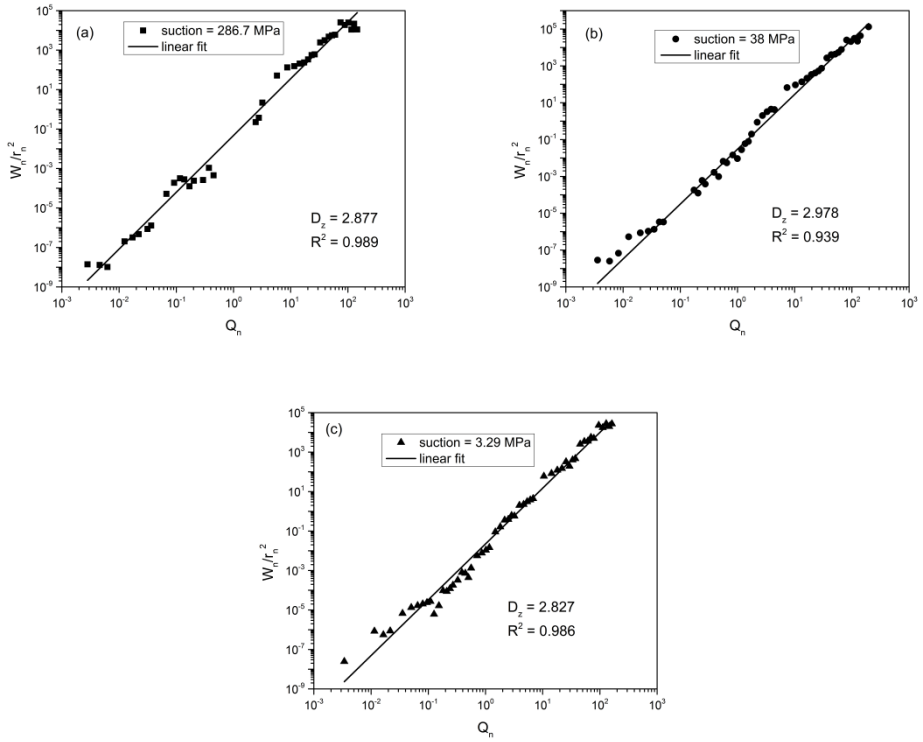

Figure 18. Fractal dimension D_z of low dry density of 1.90 g/cm^3 under (a) suction = 286.7 MPa, (b) suction = 38 MPa, (c) suction= 3.29 MPa.

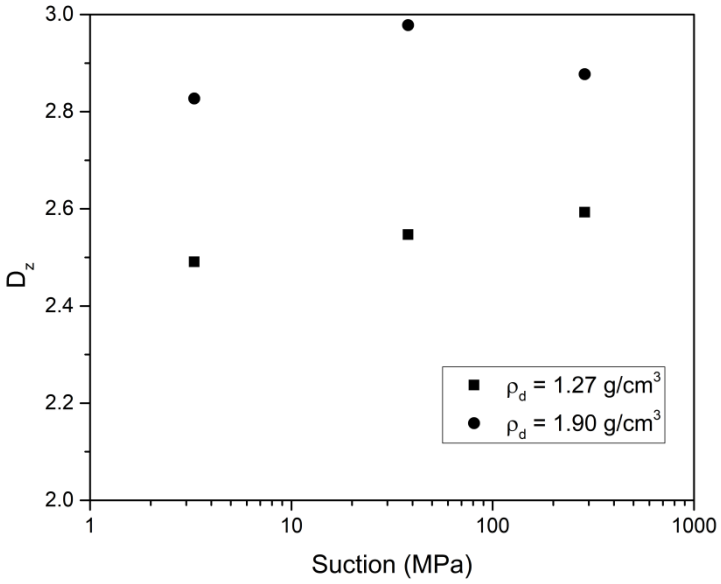

Figure 19. Fractal dimension D_z versus suction for both dry densities.

Geomechanics and Engineering, *Vol. 16, No. 1 (2018) 71-83*
DOI: https://doi.org/10.12989/gae.2018.16.1.071

A new method to predict swelling pressure of compacted bentonites based on diffuse double layer theory

Haiquan Sun*

Faculty of Science, Charles University, Albertov 6, 128 43, Prague 2, Czech Republic

(Received July 6, 2017, Revised January 2, 2018, Accepted March 29, 2018)

Abstract. Compacted bentonites were chosen as the backfill material and buffer in high level nuclear waste disposal due to its high swelling pressure, high ion adsorption capacity and low permeability. It is essential to estimate the swelling pressure in design and considering the safety of the nuclear repositories. The swelling pressure model of expansive clay colloids was developed based on Gouy-Chapman diffuse double layer theory. However, the diffuse double layer model is effective in predicting low compaction dry density (low swelling pressure) for certain bentonites, and invalidation in simulating high compaction dry density (high swelling pressure). In this paper, the new relationship between nondimensional midplane potential function, u, and nondimensional distance function, Kd, were established based on the Gouy-Chapman theory by considering the variation of void ratio. The new developed model was constructed based on the published literature data of compacted Na-bentonite (MX80) and Ca-bentonite (FoCa) for sodium and calcium bentonite respectively. The proposed models were applied to re-compute swelling pressure of other compacted Na-bentonites (Kunigel-V1, Voclay, Neokunibond and GMZ) and Ca-bentonites (FEBEX, Bavaria bentonite, Bentonite S-2, Montigel bentonite) based on the reported experimental data. Results show that the predicted swelling pressure has a good agreement with the experimental swelling pressure in all cases.

Keywords: bentonite, swelling pressure, expansive soils, nuclear waste disposal

1. Introduction

Deep geological repository is popularly being considered as storage for high level nuclear waste in many countries such as Sweden, France, Japan, China, Czech Republic, Germany, Belgium, Spain and so on (Dixon and Grey 1985, Pusch 1992, Delage 2007, Sun *et al.* 2018). The high level nuclear wastes are mainly from the 'burning' of uranium fuel in a nuclear reactor. The used uncycled nuclear fuels are firstly storage in ponds for 40 or 50 years. After that the used fuel assemblies are ready for encapsulation or loading into casks ready for indefinite storage or permanent disposal underground (WNA 2016). Spent nuclear fuel will be stored in isolated copper canisters inside underground bedrock with a depth of several hundred meters. The canisters will be placed in the tunnel galleries surrounded by multiple release barriers. Generally, the compacted bentonite blocks or other forms of bentonite like bricks and pellets are often planned as buffer and backfill material thanks to its low hydraulic conductivity, high-ion adsorption capacity and high swelling pressure (Bucher and Muller Vonmoos 1989, ENRESA 2000, Schanz and Tripathy 2009, Gueddouda 2011, Sun 2015). The function of compacted bentonite barrier is that the material should hold the canister tightly when subjected to water, simultaneously limit the access of water to waste container and prevent the migration of radionuclide into the nature, and should transfer the heat produced by nuclear radiation of nuclear fuels to the host rocks.

Once emplaced, the tunnel galleries are closed and the around environment are rebalanced. The unsaturated compacted bentonite will be hydrated by adsorbing the water or electrolytes from surrounding bedrocks. The space between canisters and bedrocks are always assumed to be constant full of compacted bentonite. The initially unsaturated compacted bentonite will exhibit swelling pressure when meet with water. To make sure the safety of the repository, the swelling pressure of the compacted bentonite must be no more than the in situ strength of the surrounding rocks. Thus, the estimation and determination of swelling pressure is essential and crucial for safety design and long terms functionality of backfill materials and buffer in nuclear repositories. Swelling pressure determined by laboratory tests have been studied by many researchers (Pusch 1982, Dixon and Gray 1985, ENRSEA 2000 and Komine 2004) who performed the tests at confined conditions without volume change of the compacted bentonite specimen.

Compacted bentonites are clays with high content of montmorillonite. Bentonite swelling is because of the clay-water-electrolyte interaction (Bolt 1956). It is known that the physicochemical forces are responsible for the swelling behavior of colloid bentonite substance from diffuse double layer theory (Bolt 1956, van Olphen, 1977, Mitchell 1993). According to Mašín (2015) summarized, the basic forms of diffuse double layer theory are only available for montmorillonite clay particles suspended in monovalent liquid solutions at low concentrations (Warkentin and

*Corresponding author, Ph.D. Student
E-mail: haiquan.sun@natur.cuni.cz

ISSN: 2005-307X (Print), 2092-6219 (Online)

Schofield 1958, Sridharan and Jayadeva 1982, Zhang *et al.* 1993, Yong 1999a, b, Komine and Ogata 1996, Mitchell and Soga 2005, Phillips and Tripathy 2011, Liu 2013). Some researchers attempted to study the swelling pressure of compacted bentonite based on diffuse double layer theory related to the physicochemical forces (Komine and Ogata 1996, Sridharan and Choudhury 2002, Tripathy *et al.* 2004, Bharat *et al.* 2013, 2017, Liu 2015, Sun 2017). The reason for difference between theoretical values from DDL theory and experimental data have been studied by many researchers (Barcey *et al.* 1972, Pusch 1982, Young and Mohamed 1992, Sridharan and Choudhury 2002, Tripathy *et al.* 2004 and Schanz and Tripahty 2009).

2. Literature review

Three mechanisms for clay mineral formation (inheritance, neoformation, and transformation) operating in three geological environments (weathering, sedimentary, and diagenetic-hydrothermal) yield nine possibilities for the origin of clay minerals in nature (Eberl 1984). The main group of clay minerals are kaolinite, illite and montmorillonite. Montmorillonite is the main content of bentonites. Generally, many types of exchangeable cations exist in bentonites material. The amount and type of cations of the bentonite depends on the mechanisms and geological environments of formation as mentioned before.

The unit layer of the montmorillonite consists of an aluminium octahedral sheet sandwiched between two silica tetrahedral sheets, as shown schematically in Fig. 1(a) (1-3). The thickness of unit layer is about 9.6 Ångström (Å) shown in Fig. 1(a) (3). Generally, cations and water molecules exist in the interlayer. The unit layers are bonded by weak van der Waal forces which occurred between molecules. The silica tetrahedral - aluminium octahedral - silica tetrahedral forms the structure of unit layer. The strong chemical bond is formed by atoms (Si-O, Al-O), which is much higher than van der Waal forces. The extensive isomorphous substitution occurred for silicon and aluminum which were replaced by other cations such as magnesium, iron, zinc, nickel, lithium etc. (Grim 1968). The charge deficiencies due to isomorphous substitution are balanced by exchangeable cations located within clay particles as shown in Fig. 1(b). The ideal arrangement of unit layers is parallel structure as shown in Fig. 1(c). In general, several unit layers comprise clay particles. The thickness of clay particles varies from 10 to 50 Å. The space between clay particles are called inter-particle pores where the diffuse double layer formed. At very low water content condition, the exchangeable cations are strongly attracted to the negative surface of unit layer. Two parallel unit layers are separated by cations which shows a very low level of hydration. This would be correspond to water in region A in Fig. 1(d). With ingress of water, the cations are partial hydrated by combining with the water molecules. The distance between unit layers will expand when the potential energy of repulsion is higher than the potential energy of attraction which comes from van der Waals forces and electrostatic forces between negative charged surface and positive charged interlayer cations. Probably, at this situation the water exist in region B as shown in Fig. 1(d). The balance of attraction and repulsion is denoted as crystalline swelling (Norrish 1954, Kittrick 1969). Crystalline swelling is a process whereby 0 to 4 discrete layers of water molecules are intercalated between unit layers shown in Fig. 1(b) (3). Layer hydrates with 0, 1, 2, 3, and 4 layers of water molecules are distinguished by basal spacings of approximately 10.0, 12.5, 15.0, 17.5 and 20.0 Å, respectively (Laird 2006). Upon further ingress of water, it will reach region C as shown in Fig. 1(d), the cations were fully hydrated and produced a higher concentration compared with the bulk fluid ion concentration far away from the clay surface. At the same time, the cations near surface try to diffuse to equilibrium the whole concentration due to the difference in ion concentration in bulk fluid solution and high ion concentration near clay surfaces. The swelling of the clay particles due to the osmotic phenomena are termed as osmotic swelling or diffuse double layer swelling (Van Olphen 1977). The negative charged clay surface, the distributed charged cation and the adsorbed water are together termed as the diffuse double layer (Bolt 1956, Van Olphen 1963). Usually, the thickness of diffuse double layer is around 200 Å which depends on the exchange cations, electronical surface charge, pore fluid, density, temperature etc.

The montmorillonite clay usually contains some monovalent or divalent cations during its formation under different geological environment. The different types of bentonite are each named after the respective dominant element, such as sodium bentonite, calcium bentonite etc. The types of exchange cations deeply influence the behavior of montmorillonite. Lambe and Whitman (1969) give the radius of un-hydrated and hydrated sodium ions as 0.98 Å and 7.8 Å, respectively. The thickness of DDL can expand to 120 Å for sodium bentonite under certain conditions (Grim 1968, Van Olphen 1977). If the monovalent sodium cations are replaced by divalent calcium or magnesium cations, there would need to be only half as many cations present to balance the negative charges on the clay particles, and the whole size of the clay particle would shrink (Nelson *et al.* 2015). Benson and Meer (2009) showed that clays having an abundance of monovalent cations had a much higher swell index than those with an abundance of divalent cations. Tamura *et al.* (2000) shown that the water uptake capacities of calcium or magnesium montmorillonites are nearly similar. The osmotic repulsive pressure is much less for divalent cations (Norrish 1954). However, the repulsive energy due to hydration of divalent exchangeable cations is significantly greater than that of monovalent ions (MacEwan 1954). These may contribute to the different swelling behavior of Na-bentonite and Ca-bentonite.

The basic form of DDL theory was proposed by Gouy-Chapman (Gouy 1910, Chapman 1913). This theory can predict the swelling behavior of bentonites by consideration of variations in clay-water-electrolyte systems. According to DDL theory, the interaction forces between double layers depends on the mindplane potential and ion concentration at mindplane between the two parallel clay platelets and its value equals to the osmotic pressure in that plane (Bolt 1956).

It is shown that the DDL theory can predict good value of swelling pressure with dry density lower than 1.55Mg/m^3

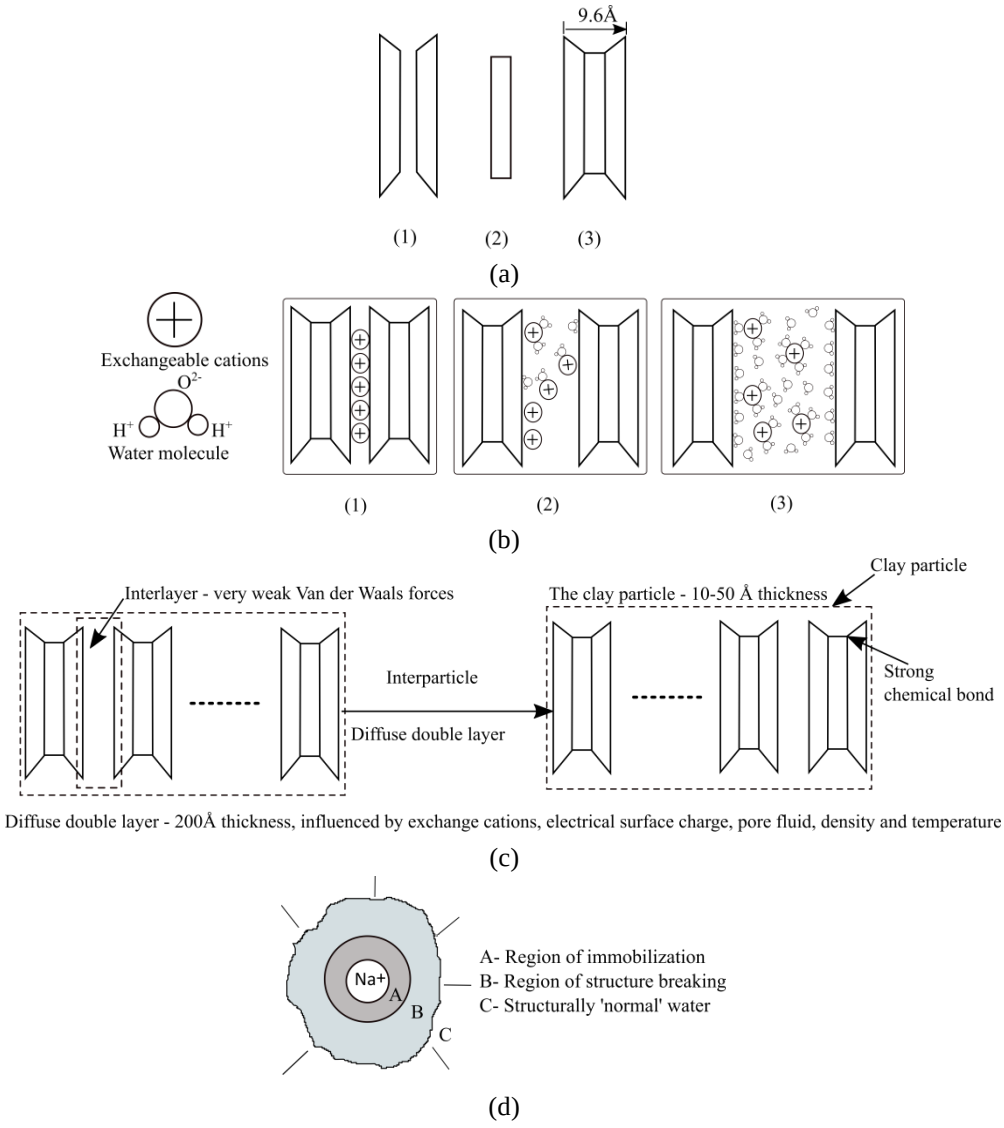

Fig. 1 Schematic diagram of structure of montmorillonite, (a) structure of unite clay layer, (1) Silica tetrahedral sheet, (2) Aluminium octahedral sheet, (3) unit clay layer; (b) Clay-water interactions, (1) dry condition, (2) water molecules wedge into the interlayer, (3) fully hydrated cations which results in repulsive forces and expanding caly layers (due to hydration energy); (c) interaction of clay particles, interpaticle, interlayer, diffuse double layer (thickness data from Lambe (1958) and Grim (1968)) and (d) Iron hydration (modified from Frank and Wen (1957))

for bentonite S-2 (Schanz and Tripathy 2009). Komine and Ogata (1996) pointed out that the DDL can predict adequately the swelling characteristics of compacted bentonite when the swelling pressure is less than about 3MPa and the type is sodium bentonite (Kunigel). However, there exists big difference between the theoretical value and experimental data at high dry density. The difference between theoretical values from DDL theory and experimental data have been studied by many researchers (Barcey *et al.* 1972, Pusch 1982, Young 1984, Young and Mohamed 1992, Sridaran and Choudhury 2002, Tripathy *et al.* 2004, Schanz and Tripahty 2009, Puppala *et al.* 2017). Some researchers (Verwey and Overbeek 1948, Van Olphen 1963 and Yong 1999) pointed out that the hydration energy due to surface and ion hydration are the major contributing factors to swelling pressure at close separation of clay platelets (high dry density). The difference between theoretical and experimental data was attributed to many factors (Bolt 1956, Sridharan and Jayadeva 1982, Mitchell 1993, Tripathy *et al.* 2004): (1) poorly developed or partially developed diffuse double layers, (2) surface and ion hydration near clay particles, (3) nonuniform size of clay particles, (4) deviation of clay fabric structure, (5) presence of non-swelling minerals in the clay.

From the literature review, it can be seen that the DDL was effective in predicting swelling pressure with low dry density for some certain bentonites (Komine and Ogata 1996) and has been successfully to explain the compressibility behavior of colloid clays (Mitchell 1993). Tripathy *et al.* (2004) proposed three new equations for prediction of swelling pressure by considering multiple valent montmorillonite, while it doesn't work well on some divalent rich bentonites (Schanz and Tripathy 2009).

In this paper the Gouy-Chapman diffuse double layer

theory are used to calculate the theoretical swelling pressure. The difference of swelling pressure between theoretical and experimental data are shown for all compacted Na-bentonites and Ca-bentonites from literature. Two new proposed equations are derived from Na-bentonites (MX80) and Ca-bentonites (FoCa), later the new equations are proposed to predict the swelling pressure of other compacted bentonites.

3. Theoretical relationship between swelling pressure and dry density

The swelling pressure is the difference between the osmotic pressure in the central plane between two clay platelets and the osmotic pressure in the equilibrium solution (Bolt 1956). The osmotic pressure at the central plane between clay platelets can be calculated from Gouy-Chapman diffuse double layer theory which original presented by Bolt (1956) and Van Olphen (1963) and improved by Sridharan and Jayadeva (1982). The following equations are used to establish the theoretical relationship between swelling pressure and dry density

$$e = G\gamma_w Sd \times 10^6 \tag{1}$$

$$\gamma_d = \frac{G\gamma_w}{1+e} \tag{2}$$

$$\int_z^u \frac{1}{\sqrt{(2\cosh y - 2\cosh u)}} dy = \int_0^d d\xi = -Kd \tag{3}$$

$$-\left(\frac{dy}{d\xi}\right)_{x=0} = \sqrt{(2\cosh z - 2\cosh u)} = \left(\frac{B}{S}\right)\sqrt{\frac{1}{2\varepsilon_0 D n_0 kT}} \quad \text{at x=0, y=z} \tag{4}$$

$$p = 2n_0 kT(\cosh u - 1) \tag{5}$$

$$K = \left(\frac{2n_0 e'^2 v^2}{\varepsilon_0 DkT}\right)^{\frac{1}{2}} \tag{6}$$

where e is the void ratio of compacted bentonite, G is the specific gravity, γ_w is the density of water, γ_d is the dry density, S is the specific surface area (m^2/g), d is the half of the distance of clay platelets (m), u is the nondimensional midplane potential, y is the nondimensional potential at a distance x from the clay surface, z is the nondimensional potential function at the surface (x = 0), ξ is the distance function(ξ = Kx), B is the base cation exchange capacity (meq/100g), ε_0 is the permittivity of vacuum (8.8542×10^{-23} $C^2J^{-1}m^{-1}$), D is the dielectric constant of bulk fluid (80.4 for water), n_0 is the ionic concentration of the bulk fluid in ions/m^3, k is the Boltzmann's constant (1.38×10^{-23} J/K), K is the diffuse double layer parameter (1/m), T is the absolute temperature in Kelvin, p is the swelling pressure (Pa), e' is the elementary electric charge (1.602×10^{-23} C), v is the weighted averaged of valency of exchangeable cations (Tripathy *et al.* 2004).

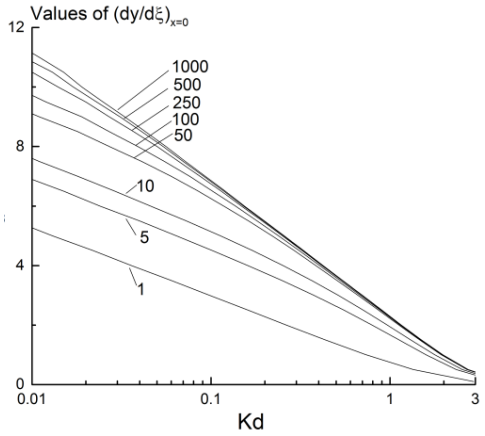

Fig. 2 Theoretical u-Kd relationship (Sridharan and Jayadeva 1982)

Sridharan and Jayadeva (1982) summarized the u and kd relationships for different values of (dy/dξ)x=0 shown in Fig. 2. A linear relationship between u and log(Kd) was suggested to compute u value for known Kd. Sridharan and Choudhury (2002) proposed u-log (Kd) for saturated slurries of Na-montmorillonites with valence of 1. Three different u-log Kd relationships were proposed as following

$$u = 2.35 - 4.375\log Kd \tag{a}$$

$$u = 2.10 - 4.583\log Kd \tag{b}$$

$$u = 2.81 - 3.375\log Kd \tag{c}$$

Eq. (a) was constructed based on all the clays (illite, kaolinite, motmorillonite) in pressure of 10-1000KPa. Eq. (b) was the theoretical u-log(Kd) only related to montmorillonite in pressure of 50-400KPa. Eq. (c) was recalculated based on experimental Na montmorillonite data.

Tripathy *et al.* (2004) used the procedures similar to Sridharan and Choudhury (2002) to propose u-log(Kd) relations. Tripathy *et al.* (2004) proposed three methods to establish the u-log(Kd) relations. The method 1 considered all u and kd values in pressure of 50-40000 KPa and with n_0 from 10^{-5} - 10^{-3}M. The method 2 was used by consideration of all the u and Kd values from 50 to 40000KPa, with n_0 equals to 10^{-4}M. The method 3 considered u-log(Kd) in the pressure range of 50-400kpa, similar to Eq. (b). The method 3 was used in his article to establish new relationship between the nondimensional midplane potential function, u and the distance function, Kd, for MX80, FEBEX, Montigel bentonite, based on comparing the experimental results and swelling pressure derived from diffuse double layer theory.

Because the swelling pressure tests were performed under the infiltration of distilled water with a concentration of approximately 10^{-4}M, thus the method 2 were adopted as theoretical DDL values in this paper. The swelling pressure can be predicted by relating the value of u obtained from Eq. (5) and Kd for any given properties of bentonite and the known bulk fluid properties (Sridharan and Jayadeva 1982, Tripathy *et al.* 2004). For a range of assumed swelling pressure, the value of u can be obtained

Table 1 Physical properties, montmorillonite content and cation exchange capacity for all compacted bentonites

Type	Name	MMT (%)	CEC (meq/100g)				BEC (meq/100g)	G	S (m^2/g)	v	w_L(%)	w_p (%)	References
			Na	Ca	Mg	K							
Na - bentonites	MX80	75	62.4	7.4	3	0.2	73	2.76	562	1.14	411±10	47	Muller-Vonmous and Kahr (1982), (1983)
	Kunigel-V1						104.4	2.7	525	1.46	416	21	Japan nuclear Cycle Development Insitute (1999)
	Voclay	69	56.6	29.3	13.2	1.6	100.7	2.84	558.9*	1.42	628.2	44.8	Komine (2004
	Neokunibond	76	62	33	6.3	1.9	103.5	2.68	615.6*	1.38	607.5	50.69	Komine 2004
	GMZ	75.4	43.4	29.1	12.3	2.5	78.3	2.71	570	1.67	276	38	Wen (2006)
Ca - bentonites	FoCa	80	3.6	73.1	6.5	0.8	84	2.67	300	1.94	112	50	Volckaert *et al.* (2000) Marcial *et al.* (2002)
	FEBEX	92±3	25	42	32	3	102	2.7	752±47	1.73	102±4	53±3	ENRESA 2000, Lajudie et al.1996
	Montigel	66	1.8	37.6	22.4	0.2	62	2.85	493	1.97	50	50	Muller-Vonmous and Kahr (1982), (1983), Lajudie *et al.* (1996)
	Bentonite S-2	92±4	22±3	41±7	31±7	2.5±1	97	2.78	614±74	1.66	105±10		ENRESA 2000
	Bavaria		9	33	32		74	2.8	650	1.88	178	56.1	Schanz *et al.* (2009)

*Note: MMT- montmorillonite, BEC – base exchange capacity, CEC- cation exchange capacity, G – specific gravity, S – specific surface, *-value estimated form the specific surface of MMT (810 m^2/g) (Komine and Ogata 1996)

Table 2 Initial water content, compaction pressure, dimensions, laboratory temperature and reference of compacted bentonite used in the paper

Bentonite	Initial WC (%)	Compaction pressure(KN)	Dimensions		T (℃)	Reference
			Dia/mm	H/mm		
MX80		100-300	56.4	20-25	20	Bucher and Müller-Vonmoos (1989)
Kunigel-V1	6.5~10.0	8.5~145	60	5		Japan Nuclear Cycle Development Institute (1999) and Komine (2004)
Voclay	11.1~15.1	8.5~145	60	5	22±1	Komine (2004)
Neokunibond	11.3~12.3	8.5~145	60	5	22±1	Komine (2004)
GMZ	11.14		50	20		Schanz and Al-Badran (2014)
FoCa	12		38~57	12-20	24±1	Imbert and Villar (2006)
FEBEX	12.5~15.5		53	7-8	20~25	ENRESA (2000)
Montigel		100~300	56.4	20~25	20	Bucher and Müller-Vonmoos (1989)
Ben. S-2	9~11		53	7~8	20~25	ENRESA (2000)
Bavaria	9.9		50	15	20	Schanz and Tripathy (2009)

from Eq. (5) and the value of z can be calculated from Eq. (4). The value of Kd also can be calculated from Eq. (3) by knowing u and z. The value of K can be determined by Eq. (6), so the value of d can be obtained from Eq. (3). Knowing d, Eq. (1) can be used to calculate e. The dry density can be calculated from Eq. (2). The integration of Eq. (3) is evaluated numerically using the "quad" MATLAB method. Thus, the theoretic relationship between swelling pressure and dry density can be obtained.

4. Materials

Various bentonites including Na-bentonites and Ca-bentonites were studied as buffer materials for nuclear waste disposal all over the world. Such as MX80, Na-bentonites original from Wyoming, USA, and FoCa bentonite, Ca- bentonites original from France and so on, which were planned as buffer and backfill materials for high level nuclear waste disposal. In this paper, it contents five Na-bentonites and five Ca-bentonites. The detailed physical properties, montmorillonite content, cation exchange capacity, liquid limit and plastic limit were shown in Table 1. Generally, the value of swelling pressure depends on the amount of montmorillonite content. It can be seen the MX80 bentonite with the montmorillonite content is around 75%, which is the average content among all the compacted Na-bentonites in the publish papers. The FoCa bentonites with the montmorillonite content is around 80% which is also the average content among all the compacted Ca-bentonites in the publish papers. In addition, the MX80 and FoCa bentonite contains the highest sodium and calcium cation content respectively. Based on this priority, the two bentonites were selected as representative of Na- bentonites and Ca-bentonites respectively. The valencies of the bentonites were obtained from the weighted average of the valencies of the cations exist in the bentonites, which suggested by Tripathy *et al.* (2004).

The swelling pressure of compacted bentonites was usually determined in the laboratory. For preparation of each dry density of specimen, the bentonite powders were statically compacted in a special compaction mould corresponding to different compaction forces. The general condition was oedometric condition which fixing the top part of the oedometric cell. And the water was infiltrated from the bottom of the specimen, the swelling pressure is measured using the load cell placed between the restrain and the top of the compacted bentonites. The volume of the compacted bentonites keeps constant during the saturation process. The tests were conducted in normal soil mechanic laboratories which has a temperature around 20 ℃. After swelling pressure test, the water content was determined by

oven drying, the degree of saturation with a value of 90-120% indicted that the specimens were almost saturated. The detailed information about the specimens such as initial state, preparation procedures, specimen dimensions, testing equipment and laboratory testing temperature were listed in Table 2.

5. Difference between theoretical and experimental swelling pressure

To calculate the theoretical swelling pressure, the u-log(Kd) relationship must be established as presented before. According to Sridharan and Jayadeva (1982) and Tripathy *et al.* (2004), the ionic concentration of the bulk fluid nearly has a molal concentration of approximately 10^{-4} M, so the concentration n_0 is assumed to 10^{-4} M in this paper. The swelling pressure varies from 0 kPa to 40 MPa for all the studied compacted bentonites. The following procedures were suggested to establishe the u-Kd relationship for all compacted bentonites: (i) assumed the pressure range which is from 50 to 40 000 KPa increased by step, u values can be obtained by Eq. (5); (ii) the value of z can be calculated from equation (4) by given the value of B, S; (iii) The value of Kd also can be calculated from equation (3) by given the value of u and z. In order to save the space, here only MX80 Na-bentonite and FoCa Ca-bentonite were listed, the calculated u and Kd values are shown in Table 2.

From Table 3, the value of $(dy/d\xi)_{x=0}$ is 211.17 and 455.208 for MX80 and FoCa bentonite respectively. According to Sridharan and Jayadeva (1982), it was noted that u plotted against log(Kd) is linear for larger values of $(dy/d\xi)_{x=0}$ and for u>1.0. The linear fitting curve of u-log(Kd) of MX80 and FoCa bentonites were shown in Fig.3. Once the relationship was obtained, the theoretical u can be calculated from Kd, in which d was calculated from Eq. (1) by assuming a series of dry density, K was calculated from Eq. (6) by the known parameters listed in Table 1. Once the value of theoretical u was got, the theoretical swelling pressure can be calculated from Eq. (5). Thus, the swelling pressure of theoretic DDL prediction of each compacted bentonite were presented in the following Eqs. (7)-(16).

Figs. 4 and 5 show the theoretical and experimental swelling pressure of sodium and calcium compacted bentonites versus dry density respectively. It can be observed that the theoretical swelling pressure of Na-bentonite corresponds to the experimental data well at low dry density for MX80 bentonite and Kunigel-V1 bentonite (<1.5 Mg/m^3).

$$p = 2n_0kT[\cosh(-3.462\log(Kd) + 3.292) - 1] \text{ MX80} \quad (7)$$

$$p = 2n_0kT[\cosh(-3.749\log(Kd) + 3.052) - 1] \text{ Kunigel–V1} \quad (8)$$

$$p = 2n_0kT[\cosh(-3.684\log(Kd) + 3.108) - 1] \text{ (Voclay)} \quad (9)$$

$$p = 2n_0kT[\cosh(-3.638\log(Kd) + 3.148) - 1] \text{ (Neokunibond)} \quad (10)$$

$$p = 2n_0kT[\cosh(-3.500\log(Kd) + 3.262) - 1] \text{ (GMZ)} \quad (11)$$

Table 3 Values of u, z, $(dy/d\xi)_{x=0}$ and Kd for MX80 bentonite and FoCa bentonite

Pressure /KPa	u	MX80 bentonite			FoCa bentonite		
		z	$(dy/d\xi)_{x=0}$	Kd	z	$(dy/d\xi)_{x=0}$	Kd
		$n_0=10^{-4}$ M					
50	5.32	10.710	211.17	0.211	12.242	455.208	0.216
100	6.01	10.714	211.17	0.146	12.243	455.208	0.152
200	6.70	10.723	211.17	0.101	12.245	455.208	0.106
400	7.39	10.741	211.17	0.069	12.249	455.208	0.074
800	8.08	10.775	211.17	0.046	12.257	455.208	0.051
1000	8.30	10.792	211.17	0.040	12.261	455.208	0.045
2000	9.00	10.872	211.17	0.026	12.280	455.208	0.031
4000	9.69	11.015	211.17	0.016	12.317	455.208	0.020
8000	10.38	11.250	211.17	0.010	12.386	455.208	0.013
10000	10.61	11.350	211.17	0.008	12.420	455.208	0.011
20000	11.30	11.739	211.17	0.005	12.571	455.208	0.007
40000	11.99	12.236	211.17	0.002	12.818	455.208	0.004

$$p = 2n_0kT[\cosh(-3.957\log(Kd) + 2.869) - 1] \text{ (FoCa)} \quad (12)$$

$$p = 2n_0kT[\cosh(-3.494\log(Kd) + 3.266) - 1] \text{ (FEBEX)} \quad (13)$$

$$p = 2n_0kT[\cosh(-3.494\log(Kd) + 3.267) - 1] \quad \text{Bentonite Montigel} \quad (14)$$

$$p = 2n_0kT[\cosh(-3.555\log(Kd) + 3.217) - 1] \quad \text{(Bentonite S-2)} \quad (15)$$

$$p = 2n_0kT[\cosh(-3.371\log(Kd) + 3.363) - 1] \quad \text{Bavaria bentonite} \quad (16)$$

This phenomenon was observed by Komine and Ogata (1996) of sodium Kunigel bentonite. According to them, the DDL theory was only effective in prediction swelling pressure with low dry density for certain bentonites. As for other Na-bentonites, the theoretical value was higher than experimental data at low dry density, while they consist with experimental data well only among some certain ranges. In Fig. 5 for compacted Ca-bentonites, the same phenomenon was found that the theoretical value corresponds well with the experimental data among low dry density range. Meanwhile it occurred bigger difference than Na-bentonites during high dry density range. In order to see the accuracy of the DDL prediction clearly, redraw the dry density against with the difference of swelling pressure which equals to the experimental data minus the DDL calculated values. Fig. 6(a) and 6(b) shows the difference of swelling pressure with increasing dry density for Na-bentonite and Ca-bentonite respectively. Assumed the difference is within ±0.5MPa, the model can be accepted. The dash line included the area between -0.5MPa and 0.5 MPa, it is clearly that the DDL model is only suitable for certain Na-bentonites shown in Fig. 6(a), while the DDL model is unavailable for Ca-bentonite with dry density higher than 1.6 Mg/m^3 shown in Fig. 6(b). It can be

concluded that the DDL theory is unavailable for compacted bentonites and it should need some revises.

It is known that swelling of bentonite (montmorillonite) has two mechanisms. One is the crystalline swelling and the other is the diffuse double layer swelling (Van Olphen 1963). Swelling of montmorillonite takes place in two distinct ways. At closed clay platelet distance (<2.2 nm) (high dry density), the expansion was primary dependent on the exchangeable cation and the hydration energy of the cations. Upon further ingress of water, when the clay platelet distance is greater than 3.5 nm, the hydrated cations will move into the solution to form the electrical diffuse

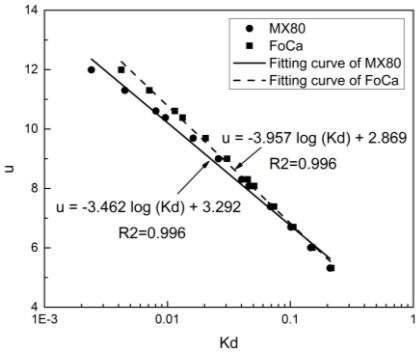

Fig. 3 Theoretic u-Kd relationships of MX80 and FoCa bentonite

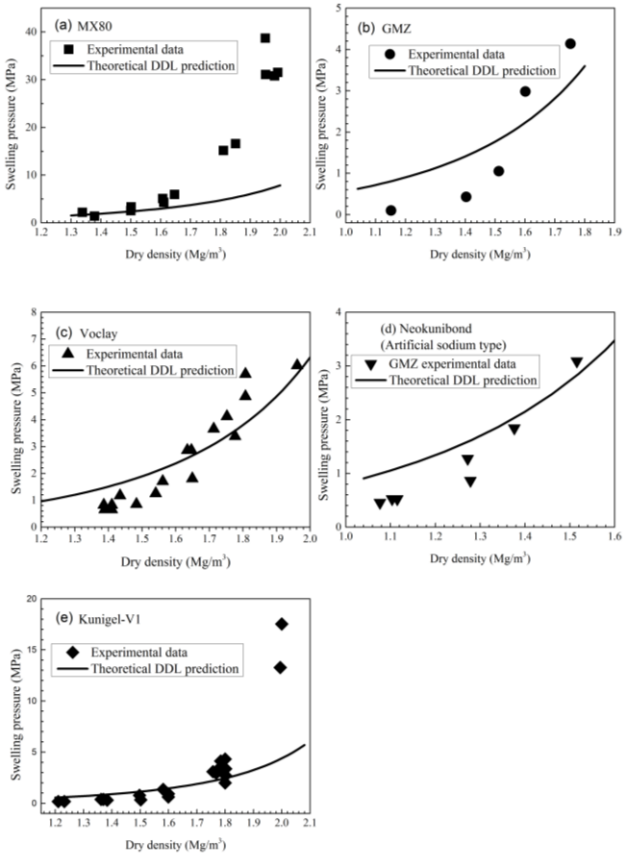

Fig. 4 Theoretical and experimental swelling pressure versus dry density for Na-bentonites, (a) MX80 bentonite, (b) GMZ, (c) Voclay, (d) Neokunibond and (e) Kunigel-V1

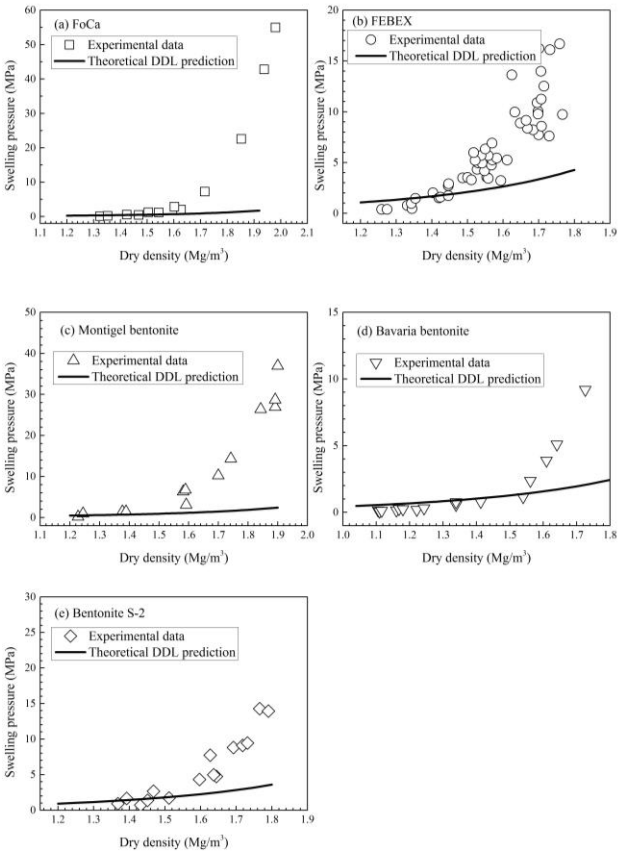

Fig. 5 Theoretical and experimental swelling pressure versus dry density for Ca-bentonites, (a) FoCa bentonite, (b) FEBEX, (c) Montigel bentonite, (d) Bavaria bentonite and (e) Bentonite S-2

double layer. The montmorillonite was thought to develop the rest of the micelle fluid and the swelling was essentially osmotic (Norrish 1954). At lower dry density, a possible dissociation of ions from the clay particle surface contributed to the diffuse double layer repulsion (Schanz *et al.* 2009). At higher dry density, the adsorptive forces due to surface and ion hydration dominated the swelling pressure. The hydration energy due to surface and ion hydration are the major contributing factors to swelling pressure at close separation of clay platelets (Verwey and Overbeek 1948, Van Olphen 1963 and Yong 1999). The swelling pressure can be regard as equivalent to the double layer repulsive pressure only when double layer repulsion is the dominated force. It is clearly to see that there are some limited conditions when using the DDL theory. The effects of ion and surface hydration energy may have effects on the swelling pressure of compacted bentonite at very close separation distance. However, the DDL theory doesn't consider this influence.

It was noted that several factors may significantly influence the swelling pressure of compacted bentonite other than the one only predicted by diffuse double layer theory. There are different kinds of cations existing in compacted bentonite, which has different hydration radius and hydration energy, and they can contribute to swelling pressure. For higher dry density, the distance between clay platelets is much closer, even their respective force fields overlap and have a great influence on the behavior of the

clay-electrolyte system. Therefore, it needs developed of the basic DDL theory used for predicting the swelling pressure of compacted bentonite.

6. Suggested new relationship of u-log(Kd)

The effects of ions and surface hydration energy can deeply influence the swelling pressure of compacted bentonite at very close separation distance as previous discussed. The swelling pressure is initially predicted by Eq. (5). The parameter n_0, k and T in Eq. (5) are assumed to be constant in this article, the theoretical swelling pressure only depends on the non-dimensional mid-plane potential u. The value of u is the reason for the difference between theoretical DDL prediction and experimental data. It is necessary to compare the theoretical and experimental u and study their difference. From experimental results, the u values can be calculated by knowing the swelling pressure by Eq. (5). K values can be obtained by Eq. (6). The values of d can be calculated by Eq. (1), thus Kd values can be obtained. The void ratio corresponding to each dry density also can be calculated by Eq. (1).

Considering the difference of preserve cations in different bentonite, the mineral components and the difference between theoretical and measured swelling pressure (Table 1, Fig. 6). Here, the MX80 and FoCa bentonite contained the highest sodium and calcium content respectively, also they have the average montmorillonite content among Na-bentonite and Ca-bentonite. Therefore, MX80 and FoCa bentonite can be regarded as the representative of Na-bentonites and Ca-bentonites

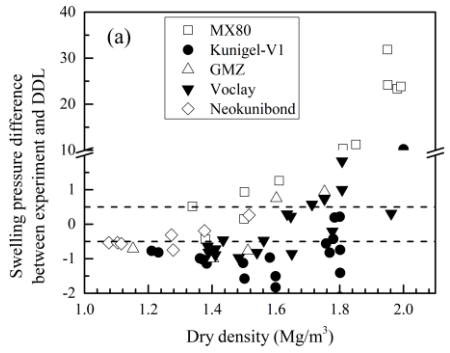

(a)

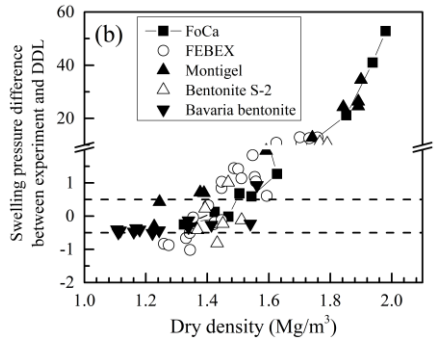

(b)

Fig. 6 The swelling pressure difference between experimental data and DDL theoretical values versus dry density for (a) Na-bentonites and (b) Ca-bentonites

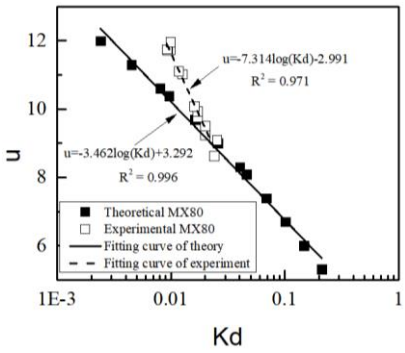

(a)

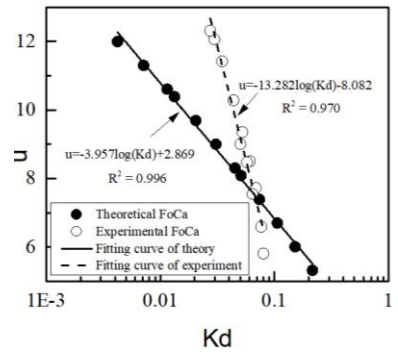

(b)

Fig. 7 The theoretical and experimental u-log(Kd) relationship of (a) MX80 bentonite and (b) FoCa bentonite

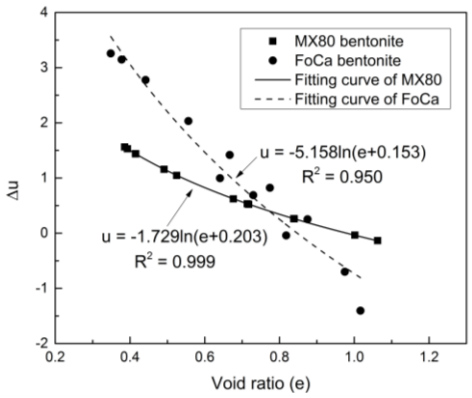

Fig. 8 Relationship between Δu and void ratio of (a) MX80 bentonite and (b) FoCa bentonite

respectively. Fig. 7 shows the theoretical and actual experimental relationship of u and log(Kd) for MX80 bentonite and FoCa bentonite. The slope of experimental data is much lower than theoretical value for both bentonites, which results the difference between theoretical and experimental results. Considering Fig. 6, it is obvious that the difference between the DDL predicted and experimental swelling pressure seems to have an exponential increase trend against the dry density for all bentonites.

Once the experimental u and log(Kd) relationship was obtained, the difference in u values, Δu, can be calculated using experimental u values minus theoretical DDL u values. Because of the limit of DDL, especially its inaccurately predicted at high dry density range, which the

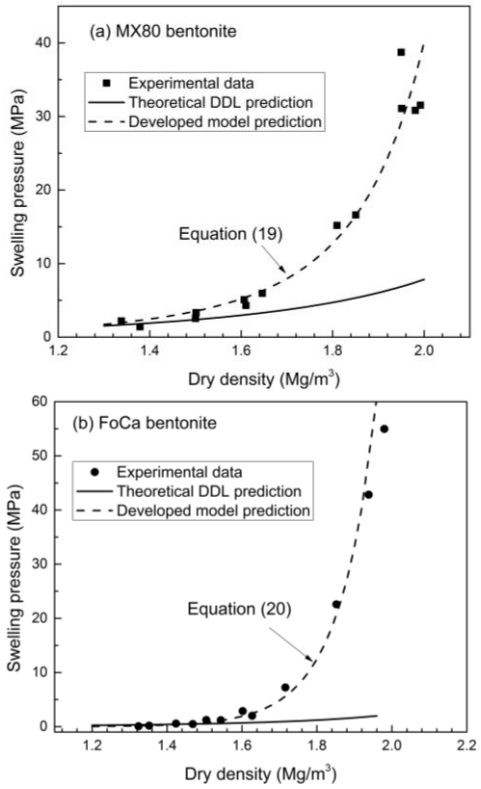

Fig. 9 Theoretical DDL prediction, experimental and developed model for swelling pressure of (a) MX80 bentonite and (b) FoCa bentonite

hydration energy of ions or repulsive forces mainly controls (Schanz and Tripathy 2009). It results in the difference of swelling pressure between theoretical and experimental data. The difference Δu may compensate the hydration energy, repulsive pressure etc. which are not considered in DDL theory. Because the swelling pressure has relations to u (Eq. (5)), and u has relations with clay platelets d (equation 3), d has relations with e (Eq. (1)), so the difference of u should follow some function of void ratio. From the expression of Eq. (5), an attempt was made to revise the relationship between u and log(Kd).

An idea came out that the difference of experimental and theoretical non-dimensional mid-plane potential, Δu, should follow the same trend with dry density. The growth form of hyperbolic function cosh(u) and exponential function follows the same style. Based on this, it is assumed that the Δu has an exponential increased with dry density. Considering the difference of swelling pressure is negative below dry density of 1.5 Mg/m^3 and positive in the following dry density, the Δu would have a natural logarithm decreased with increased of void ratio. Here we choose the void ratio instead of dry density considering the non-dimension of void ratio. Based on the experimental information of MX80 and FoCa bentonite, the relationship between Δu and e were established for Na-bentonites and Ca-bentonites. The Δu versus void ratio (e) of MX80 and FoCa bentonite was presented in Fig. 8.

The natural logarithm relationship between Δu and void ratio (e) can be obtained. Their relationships were shown in Eqs. (17) and (18). The values of Δu decrease with the increasing of void ratio. The new modified nondimension midplane potential can be got by added Δu to theoretical u. And the swelling pressure can be recomputed by Eqs. (19) and (20) for MX80 and FoCa bentonite respectively. Fig. 9 shows swelling pressure versus dry density of MX80 and FoCa bentonite by the experimental, DDL theory and proposed Eqs. (19) and (20). It can be seen the proposed equations predicted much better than the original DDL theory at high dry density range. The proposed equation has a good agreement with the experimental data. Eqs. (21) and (22) were the proposed equations for calculating swelling pressure of Na-bentonite and Ca-bentonite.

$$\Delta u_{MX80} = -1.729\ln(e+0.203) \quad \text{(Na - bentonite)} \tag{17}$$

$$\Delta u_{FoCa} = -5.158\ln(e+0.153) \quad \text{(Ca - bentonite)} \tag{18}$$

$$p = 2n_0kT[\cosh((-3.462\log(Kd) + 3.292) - 1.729\ln(e+0.203)) - 1] \tag{19}$$

$$p = 2n_0kT[\cosh((-3.957\log(Kd) + 2.869) - 5.158\ln(e+0.153)) - 1] \tag{20}$$

$$p=2n_0kT[\cosh(u_{theory} + \Delta u_{MX80}) - 1] \tag{21}$$

$$p=2n_0kT[\cosh(u_{theory} + \Delta u_{FoCa}) - 1] \tag{22}$$

7. Verification of proposed equations for swelling pressure

The modified swelling pressure equation (21) and (22) were derived based on experimental MX80 and FoCa bentonite data and DDL theory, which were proposed for Na- and Ca-bentonite respectively. And later the equations

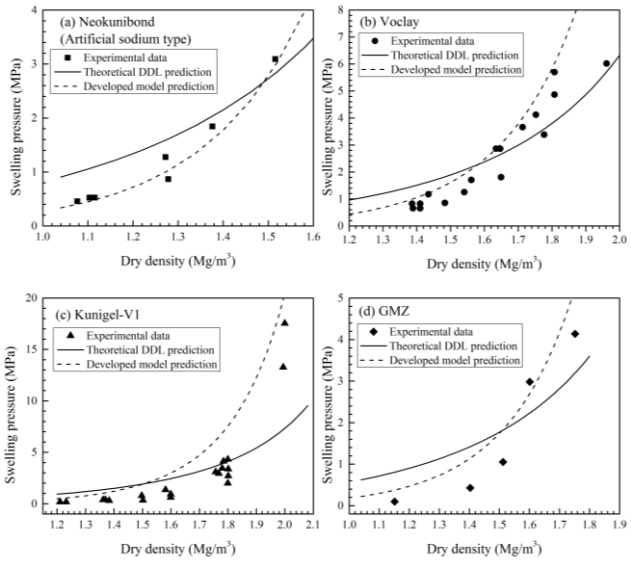

Fig. 10 Theoretical DDL prediction, experimental and developed model for swelling pressure of Na-bentonites (a) Nekunibond bentonite, (b) Voclay bentonite, (c) Kunigel-V1 bentonite and (d) GMZ bentonite

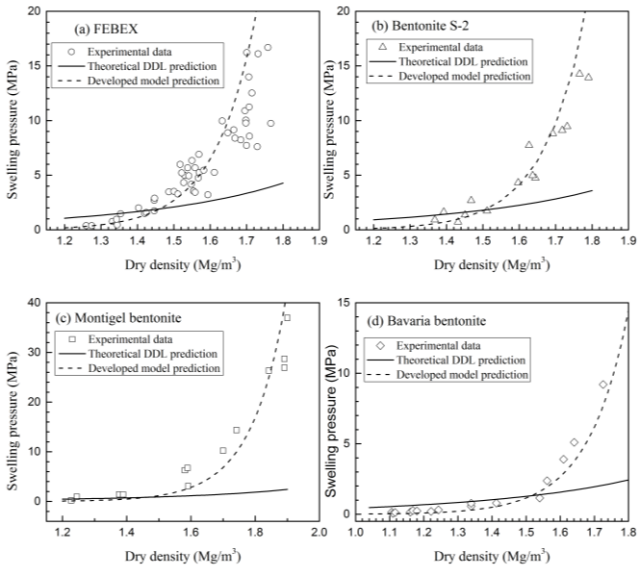

Fig. 11 Theoretical DDL prediction, experimental and developed model for swelling pressure of Ca-bentonites (a) FEBEX bentonite, (b) Bentonite S-2, (c) Montigel bentonite and (d) Bavaria bentonite

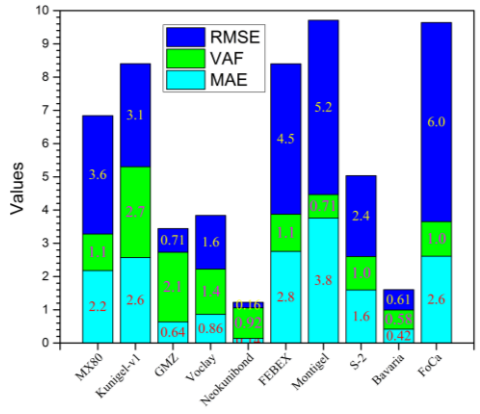

Fig. 12 Theoretical DDL prediction, experimental and developed model for swelling pressure of Ca-bentonites (a) FEBEX bentonite, (b) Bentonite S-2, (c) Montigel bentonite and (d) Bavaria bentonite

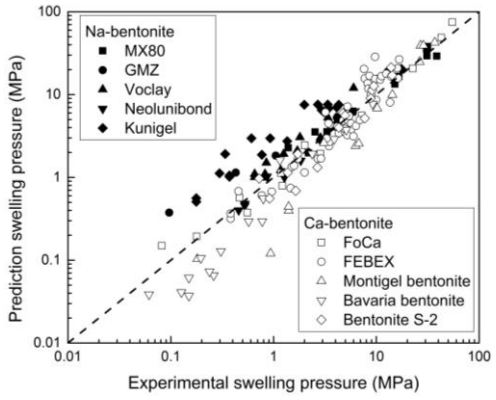

Fig. 13 Experimental swelling pressure versus prediction swelling pressure for all the compacted bentonite

will be applied in other nuclear waste barrier materials as listed before. Detailed as following: experimental swelling pressure data of FEBEX bentonite (ENRESA 2000) from Spain, Kunigel V1 (Japan Nuclear Cycle Development Institute 1999), Voclay and Neokunibond bentonite (Komine 2004) from Janpan, bentonite S-2 (ENRESA 2000) from Spain, Bavaria Bentonite (Schanz and Tripathy 2009) and Montigel bentonite (Bucher and Müller-Vonmoos 1989) from Germany, GMZ bentonite (Schanz and Al-Badran 2014) from Gaomiaozi County (Inner Mongolia, China) were selected for the verification of the new modified swelling-pressure equations. The theoretical u-log(Kd) relationship were presented from Eqs. (7)-(16). The experimental u-log(Kd) can be obtained by assumed the known swelling pressure as mentioned before.

The swelling pressure of Na-bentonites and Ca-bentonites, reported by experimental tests, calculated by theoretical DDL prediction and recalculated by proposed equations, versus dry density relationship are plotted in Figs. 10 and 11, respectively. It can be seen that the proposed equations can predict the swelling pressure more accuracy than the DDL prediction.

In order to discuss the accuracy of the developed model, the variance accounted for two values (VAF), mean absolute error (MAE) and the root mean square error (RMSE) which were presented by Eqs. (23), (24) and (25) respectively, were also computed to evaluate the performance of the proposed model. VAF, MAE and RMSE are frequently used to evaluate the difference between values predicted by a model and the measured values actually obtained in laboratory.

$$VAF = \left[1-\frac{var(X_{exp,i}-X_{model,i})}{var(X_{exp,i})}\right]\times 100\% \quad (23)$$

$$MAE = \frac{1}{n}\sum_{i=0}^{n}\left|x_{exp,i}-x_{model,i}\right| \quad (24)$$

$$RSEM = \sqrt{\frac{\sum_{i=0}^{n}(X_{exp,i}-X_{model,i})^2}{n}} \quad (25)$$

where $x_{exp,i}$ and $x_{model,i}$ is the experimental value and the model predicted value at i stage, respectively. n is the observation times.

If VAF equals to 100%, MAE and RMSE equals to zero, in which the experimental value equals to model predicted value, it means that the model is quite perfect. The higher the VAF value and the lower the MAE and RSEM values, the better the model works. The swelling pressure predicted by the proposed equations are compared with their experimental data. All the values of each compacted bentonite are shown in Fig. 12.

In Fig. 13, the abscissa represents the experimental swelling pressure and the ordinate represent the model prediction swelling pressure of all the bentonites. The model prediction values are very accurate when all the points located in diagonal line (dash line). In other words, the nearer the points closed to the line, the more accuracy the model is. The Kunigel-V1 values are above the line at 0.3-09 MPa range, which means that the model predicted a little higher than the experimental data. This phenomenon can be confirmed by the highest VAF value of Kunigel-V1

in Fig. 12. At lower swelling pressure range 0.06-0.3 MPa, the Bavaria bentonite data is below the line, which means that the model predicted much lower than the experimental data. Due to the logarithmic-logarithmic coordinates, a tiny difference would reflect a big difference in the Figures. At this time, the MAE values will help us to evaluation the accuracy of the proposed model. Results show that the prosed model work well for Bavaria bentonite. The agreement between experimental and model predicted value can be observed in Fig. 13. The results show that the proposed model prediction Eqs. (21) and (22) worked well for Na-bentonites and Ca-bentonites.

8. Comparison with other developed DDL model

In order to compare the proposed model with previous published models especially for divalent rich bentonite, the Bavaria bentonite was a good candidate. The modified swelling pressure equations proposed by Tripathy *et al.* (2004) considering the weight average valency of cations in clay are as following

$$p = 2nkT[\cosh(-7.277\ \log_{10} Kd - 2.91) - 1] \quad \text{(for v = 1.14 -1.50)} \tag{26}$$

$$p = 2nkT[\cosh(-10.427\ \log_{10} Kd - 7.72) - 1] \quad \text{(for v = 1.66 −1.73)} \tag{27}$$

$$p = 2nkT[\cosh(-9.190\ \log_{10} Kd - 3.26) - 1] \quad \text{(for v = 1.97)} \tag{28}$$

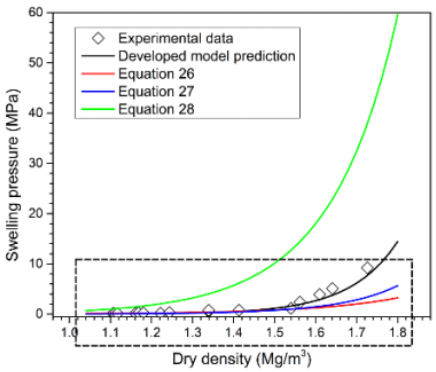

(a)

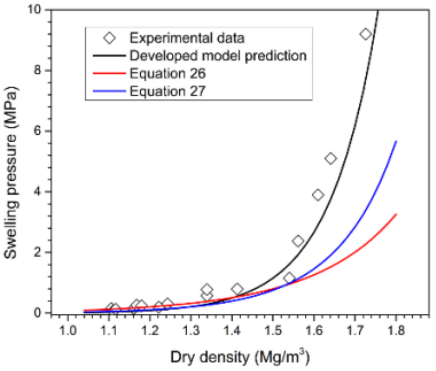

(b)

Fig. 14 Experimental data and model prediction values of Bavaria bentonite (a) and Zoom in dash area (b)

Because the average valency is 1.88, so the equation 28 was adopted to calculate the swelling pressure. The calculated results were shown in Fig. 14 with green line, it was far higher than the experimental results. Also, the Eqs. (26) and (27) were also used to calculate the swelling pressure as shown in Fig. 14. Results show that both equations predicted well below dry density of 1.55 Mg/m^3. Because Eqs. (26) and (27) were mainly for certain valence range, both is not suitable for Bavaria bentonite. It can be seen that the proposed model in the paper predicted well for Bavaria bentonite.

9. Conclusions

The swelling pressure of several bentonites was calculated from Gouy-Chapman diffuse double layer theory and compared with the experimental data. Results show that the original theoretical DDL prediction can't predict swelling pressure well. It predicted much lower at high dry density for all the bentonites. Many factors contribute to this as discussed in the paper. Based on the MX80 representing Na-bentonite and FoCa representing Ca-bentonite data, the modified new relationship between nonodimension midplane potential, u, and distance function, Kd, were derived. The new relationships were suggested to calculate swelling pressure of other bentonites. The proposed equations were verified by other compacted bentonites such as Kunigel, FoCa, Bentonite S-2 and Montigel bentonite, Voclay, Neokunibond, GMZ bentonite, FEBEX and Bavaria bentonite. The swelling pressures calculated by proposed equations indicated a good agreement with the experimental swelling pressures. The proposed equations are valid in predicting of swelling pressure of compacted bentonite.

Acknowledgements

The financial support by the research grant No. 846216 of Charles University Grant Agency is greatly appreciated. The author also greatly appreciated the STARS (Supporting TAlented Ph.D. Research Students) scholarship offered by Charles University.

References

Barcey, L., Harrington, A. and Ottewill, R.H. (1972), "The measurement of forces between particles in disperse systems", *Kolloid Zeitschrift Zeitschrift fuer Polymere*, **250**(7), 655-666.

Benson, C.H. and Meer, S.R. (2009), "Relative abundance of monovalent and divalent cations and the impact of desiccation on geosynthetic clay liners", *J. Geotech. Geoenviron. Eng.*, **135**(3), 349-358.

Bharat, T.V. and Das, D.S. (2017), "Physicochemical approach for analyzing equilibrium volume of clay sediments in salt solutions", *Appl. Clay Sci.*, **136**, 164-175.

Bharat, T.V., Sivapullaiah, P.V. and Allam, M.M. (2013), "Novel procedure for the estimation of swelling pressures of compacted bentonites based on diffuse double layer theory", *Environ. Earth Sci.*, **70**(1), 303-314.

Bolt, G.H. (1956), "Physico-chemical analysis of the compressibility of pure clays", *Géotechnique*, **6**(2), 86-93.
Bucher, F and Müller-Vonmoos, M. (1989), "Bentonite as a containment barrier for the disposal of highly radioactive waste", *Appl. Clay Sci*., **4**(2), 157-177.
Chapman, D.L. (1913), "A contribution to the theory of electro-capillarity", *Philosoph. Mag*., **25**, 475-481.
Delage, P. (2007), *Microstructure Features in the Behaviour of Engineered Barriers for Nuclear Waste Disposal*, in *Experimental Unsaturated Soil Mechanics*, Springer, 11-32.
Dixon, D.A and Gray, M.N. (1985), *The Engineering Properties of Buffer Material*, Technical Report TR-350, Fuel Waste Technology Branch, Whiteshell Laboratories, Pinawa, Canada.
Eberl, D.D. (1984), "Clay mineral formation in rocks and soils", *Philos. Trans. R. Soc. London Ser. A*, **311**(1517), 241-257.
ENRESA. (2000), *FEBEX project-Full Scale Engineered Barriers Experiments for a Deep Geological Respiratory for High Level Radioactive Waste in Crystalline Host Rock*, Final Report, Publicación Téechnica 1/2000, Empresa Nacional de Residuos Radiactivos SA (ENRESA), Madrid, Spain.
Gouy, G. (1910), "Electric charge on the surface of an electrolyte", *J. Phys*., **4**(9), 457-467.
Grim, R.E. (1968), *Clay Mineralogy*, McGraw-Hill, New York, U.S.A.
Gueddouda, M.K., Lamara, M., Abou-Bekr, N. and Taibi, S. (2010), "Hydraulic behaviour of dune sand-bentonite mixtures under confining stress", *Geomech. Eng*., **2**(3), 213-227.
Imbert, C. and Villar, M.V. (2006), "Hydro-mechanical response of a bentonite pellets/powder mixture upon infiltration", *Appl. Clay Sci*., **32**(3-4), 197-209.
Japan Nuclear Cycle Development Institute. (1999), *H12: Project to Establish the Scientific and Technical Basis for HLW Disposal in Japan: Supporting Report 2 (Respiratory Design and Engineering Technology)*, Japan Nuclear Cycle Development Institute, Tokyo, Japan.
Kittrick, J.A. (1969), "Interlayer forces in montmorillonite and vermiculite", *Soil Sci. Soc. Am. Proc*., **33**(2), 217-222.
Komine, H. (2004), "Simplified evaluation for swelling characteristics of bentonites", *Eng. Geol*., **71**(3-4), 265-279.
Komine, H. and Ogata, N. (1996), "Prediction for swelling characteristics of compacted bentonite", *Can. Geotech. J*., **33**(1), 11-22.
Laird D.A (2006), "Influence of layer charge on swelling of smectites", *Appl. Clay Sci*., **34**(1-4), 74-87.
Lajudie, A., Raynal, J., Petit, J.C. and Toulhoat, P. (1996), "Clay-based materials for engineered barriers: A review", *Mater. Res. Soc. Symp. Proc*., **353**, 221-229.
Lambe, T.W. and Whitman, R.V. (1969), *Soil Mechanics*, John Wiley and Sons, New York, U.S.A.
Liu, L. (2013), "Prediction of swelling pressures of different types of bentonite in dilute solutions", *Colloid. Surf. A Physicochem. Eng. Aspect*., **434**, 303-318
Liu, L. (2015), "Counterion-only electrical double layers: An application of density functional theory", *J. Chem. Phys*., **143**(6), 064902.
MacEwan, D.M.C. (1954), "Short-range electrical forces between charged colloid particles", *Nature*, **174**(4418), 39-40.
Marcial, D., Delage, P. and Cui, Y.J. (2002), "On the high stress compression of bentonites", *Can. Geotech. J*., **39**(4), 812-820.
Mašín, D. and Khalili, N. (2016), "Swelling phenomena and effective stress in compacted expansive clays", *Can. Geotech. J*., **53**(1), 134-147.
Mitchell, J.K. (1993), *Fundamentals of Soil Behaviour*, 2nd Edition, John Wiley and Sons, New York, U.S.A.
Mitchell, J.K. and Soga, K. (2005), *Fundamentals of Soil Behaviour*, 3rd Edition, John Wiley & Sons, New York, U.S.A.
Müller-Vonmoos, M. and Kahr, G. (1982), *Bereitstellung von Bentonit für Laboruntersuchungen*, Nationale Genossenschaft für die Lagerung Radioaktiver Abfälle, Nagra Technischer Bericht 82-04, Nagra, Wettingen, Switzerland.
Müller-Vonmoos, M. and Kahr, G. (1983), *Mineralogische Untersuchungen von Wyoming Bentonit MX-80 und Montigel*, Nagra Technischer Bericht, 83-12.
Nelson, J.D., Chao, K.C., Overton, D.D. and Nelson, E.J. (2015), *Foundation Engineering for Expansive Soils*, Wiley, New York, U.S.A.
Norrish, K. (1954), "The swelling of montmorillonite", *Discuss. Faraday Soc*., **18**, 120-134.
Phillips, A. and Tripathy, S. (2011), "Swelling pressures of some initially saturated and compacted saturated bentonites", *J. Adv. Technol. Civ. Eng*., **1**(1), 64-69.
Puppala, A.J., Pedarla, A., Pino, A. and Hoyos, L.R. (2017), "Diffused double-layer swell prediction model to better characterize natural expansive clays", *J. Eng. Mech*., **143**(9), 04017069.
Pusch, R. (1982), "Mineral-water interactions and their influence on the physical behaviour of highly compacted Na bentonite", *Can. Geotech. J*., **19**(3), 381-387.
Pusch, R. (1992), "Use of bentonite for isolation of radioactive waste products", *Clay Miner*, **27**(3), 353-361.
Schanz, T. and Al-Badran, Y. (2014), "Swelling pressure characteristics of compacted Chinese Gaomiaozi bentonite GMZ01", *Soils Found*., **54**(4), 748-759.
Schanz, T. and Tripathy, S. (2009), "Swelling pressure of a divalent-rich bentonite: Diffuse double-layer theory revisited", *Water Resour. Res*., **45**(2), W00C12.
Sridharan, A. and Choudhury, D. (2002), "Swelling pressure of sodium montmorillonites", *Géotechnique*, **52**(6), 459-462.
Sridharan, A. and Jayadeva, M.S. (1982), "Double layer theory and compressibility of clays", *Géotechnique*, **32**(2), 133-144.
Sun, D.A., Zhang, L., Li, J. and Zhang, B. (2015), "Evaluation and prediction of the swelling pressures of GMZ bentonites saturated with saline solution", *Appl. Clay Sci*., **105**, 207-216.
Sun, H. (2017), "Prediction of swelling pressure of compacted bentonite with respect to void ratio based on diffuse double layer theory", *Proceedings of the GeoMEast 2017: Advances in Characterization and Analysis of Expansive Soils and Rocks*, Sharm El-Sheikh, Egypt, July.
Sun, H., Mašín, D., Najser, J., Neděla, V. and Navratilova, E. (2018), "Bentonite microstructure and saturation evolution in wetting-drying cycles evaluated using ESEM, MIP and WRC measurements", *Géotechnique*, 1-53.
Tamura, K., Yamada, H. and Nakazawa, H. (2000), "Stepwise hydration of high-quality synthetic smectite with various cations", *Clays Clay Miner*., **48**(3), 400-404.
Tripathy, S., Sridharan, A. and Schanz, T. (2004), "Swelling pressures of compacted bentonites from diffuse double layer theory", *Can. Geotech. J*., **41**(3), 437-450.
Van Geet. M., Bastiaens W., Volckaert, G., Weetjens, E., Sillen, X., Maes, N., Imbert, Ch., Billaud, P., Touzé, G., Filippi, M., Plas, F., Villar, M.V., García-Gutiérrez, M., Mingarro, M., Gens, A. and Vallejan, B. (2009), *A Large-scale in situ Demonstration Test for Repository Sealing in an Argillaceous Host Rock-Phase II*, Technical Report No. EUR 24161 EN, European Commission, Contract No. FIKW-CT-2000-00010.
Van Olphen, H. (1963), *An Introduction to Clay Colloid Chemistry: For Clay Technologists, Geologists and Soil Scientists*, Interscience, New York, U.S.A.
Van Olphen, H. (1977), *An Introduction to Clay Colloid Chemistry: For Clay Technologists, Geologists and Soil Scientists*, 2nd edition, Wiley-Interscience, New York, U.S.A.
Verwey, E.J.W. and Overbeek, J.T.G. (1948), Theory of the Stability of Lyophobic Colloids, Elsevier.

Warkentin, B.P. and Schofield, R.K. (1958), "Swelling pressures of dilute Na-montmorillonite pastes", *Proceedings of the 7th National Conference on Clays and Clay Minerals*, Washington, D.C., U.S.A., October.

Wen, Z.J. (2006), "Physical property of China's buffer material for high-level radioactive waste repositories", *Chin. J. Rock Mech. Eng.*, **25**(4), 794-800.

WNA (2016), *Radioactive Waste Management*, World Nuclear Association, London, U.K., <http://www.world-nuclear.org/>.

Yong, R.N. (1999a), "Overview of modeling of clay microstructure and interactions for prediction of waste isolation barrier performance", *Eng. Geol.*, **54**(1-2), 83-91.

Yong, R.N. (1999b), "Soil suction and soil-water potentials in swelling clays in engineered barriers", *Eng. Geol.*, **54**(1-2), 3-13.

Yong, R.N. and Mohamed, A.M.O. (1992), "A study of particle interaction energies in wetting of unsaturated expansive clays", *Can. Geotech. J.*, **29**(6), 1060-1070.

Yong, R.N., Sadana, M.L. and Gohl, W.B. (1984), "A particle interaction model for assessment of swelling of an expansive soil", *Proceedings of the 5th International Conference on Expansive Soils*, Adelaide, Australia, May.

Zhang, F., Zhang, Z.Z., Low, P.F. and Roth, C.B. (1993), "The effect of temperature on the swelling of montmorillonite", *Clay Miner.*, **28**, 25-31.

CC